# Contact Measurements in the Cadaveric Human Hip Using Optical Fiber Sensors

by

Devan Bouchard
B.A.Sc., University of British Columbia, 2006

A Thesis Submitted in Partial Fulfillment
of the Requirements for the Degree of

MASTER OF APPLIED SCIENCE

in the Department of Mechanical Engineering

# Supervisory Committee

Contact Measurements in the Cadaveric Human Hip Using Optical Fiber Sensors

by

Devan Bouchard
B.A.Sc., University of British Columbia, 2006

**Supervisory Committee**

Dr. Peter Wild, Supervisor
(Department of Mechanical Engineering)

Dr. Stephanie Willerth, Departmental Member
(Department of Mechanical Engineering)

# Abstract

**Supervisory Committee**

Dr. Peter Wild, Supervisor
(Department of Mechanical Engineering)

Dr. Stephanie Willerth, Departmental Member
(Department of Mechanical Engineering)

The overarching goal of this study was to develop a method to measure solid matrix stress, *ex vivo,* in the articular cartilage of three cadaveric human hip joints. The primary objectives were to establish the day to day repeatability of the method over three sequential days of testing before resecting the labrum on the fourth day to observe changes in joint behavior.

Three to six fiber optic contact stress sensors were inserted within the middle zone of the acetabular cartilage to measure solid matrix stress in three hemipelvis hip specimens. A fiber optic hydrostatic fluid pressure sensor was used to simultaneously measure the synovial fluid pressure in the fossa while a representative physiological load was applied using a materials testing machine. Once inserted, the location of all sensors was quantified using a radio-stereometric analysis technique showing good repeatability of sensor location.

The target radial positions of contact stress sensors were 0º, 25º, and 50º anterior of the AIIS and the observed positions were -1º ± 5º, 27º ± 3º and 56º ± 14º. Measurements of 0.26 ± 0.13 MPa and 0.440 ± 0.14 MPa for peak hydrostatic synovial fluid pressure show poor repeatability and no consistent change was observed after labral resection.

Two contact stress sensors measured positive solid matrix stress values of 0.21 MPa and 0.69 MPa which agree with the findings of a similar experiment, however, poor day to day repeatability was observed. The difference between maximum and minimum stress values tended to be lower, and the nominal maximum solid matrix stress value higher, on the final day of testing after labral resection. No clear, consistent difference in the mean value of the solid matrix stress at the end of the test was found between tests with the intact labrum and after labral resection. Significant cross-sensitivity artifact is suspected in the solid matrix stress measurements significantly limiting the results. Several recommendations to improve upon these limitations in future work have been identified.

Despite challenges during the experimental work and poor repeatability of measurements from the fiber optic sensors, incremental advances were made toward achieving the goal of developing a measurement system for cartilage solid matrix stress in the hip.

# Table of Contents

Supervisory Committee ..... ii
Abstract ..... iii
Table of Contents ..... v
List of Tables ..... vii
List of Figures ..... viii
List of Abbreviations ..... xi
Acknowledgements ..... xii
Dedication ..... xiii
Chapter 1: Introduction ..... 1
1.1 Anatomical Background ..... 1
1.2 Clinical Motivation ..... 4
1.3 Objectives ..... 7
1.4 Organization of Thesis ..... 8
Chapter 2: Contact Mechanics of the Human Hip ..... 9
2.1 Anatomical Region of Interest ..... 9
2.2 Load Transfer Across Biphasic Articular Cartilage Tissue ..... 12
2.3 Sensors for *Ex Vivo* Contact Measurements in the Hip ..... 16
2.4 Key Findings of *Ex Vivo* Contact Studies ..... 21
2.5 Role of the Labrum as a Hydrostatic Seal ..... 27
2.6 Physiological Alignment During Specimen Potting ..... 28
Chapter 3: Experimental Setup and Methodology ..... 33
3.1 Contact Stress Sensor Calibration ..... 33
3.2 Hydrostatic Pressure Sensor Calibration ..... 36
3.3 Temperature Calibration of Both Sensor Types ..... 37
3.4 Specimen Preparation and Potting ..... 40
3.5 Sensor Insertion ..... 42
3.6 Radiographic Technique for Quantifying Sensor Location ..... 51
3.7 Material Testing Machine Experimental Setup ..... 54
3.8 Representative Physiological Loading ..... 55
3.9 Data Acquisition During Experiments ..... 56
3.10 Testing Protocol ..... 57
3.11 Labral Resection ..... 58
Chapter 4: Experimental Results and Discussion ..... 59
4.1 Sensor Calibration Results ..... 60
4.2 Accuracy and Repeatability of Sensor Placement ..... 63
4.3 Durability of Sensor Fixation ..... 66
4.4 Effect of Cartilage Quality on Durability of Sensors ..... 67
4.5 Hydrostatic Pressure Measurements in the Fossa ..... 70
4.6 Overall Joint Consolidation ..... 74
4.7 Solid Matrix Stress Contact Measurements in Cartilage ..... 78
4.8 Temperature ..... 84
4.9 Study Strengths ..... 86

4.10 Study Limitations ..... 86
Chapter 5: Recommendations and Conclusion ..... 89
5.1 Recommendations for Future Work ..... 89
5.2 Conclusions ..... 90
Bibliography ..... 93
Appendix A : Detailed Specimen Potting Protocol ..... 100
Appendix B : Detailed Test Protocol ..... 102
Appendix C : Protease Solution ..... 103

# List of Tables

Table 2-1: Summary of Peak and Average *Ex Vivo* Contact Stress Measurements for Stance Phase of Gait ..... 21

Table 2-2: Explanation of Common Contact Patterns on the Acetabular Cartilage Surface ..... 22

Table 2-3: Comparison of Experimentally Measured Load to Actual Applied Load..... 25

Table 2-4: Comparison of Orientation for Specimen Potting Used for Single Leg Stance Phase of Gait in *Ex Vivo* Studies..... 30

Table 3-1: Donor Information..... 40

Table 4-1: Sensor Calibration Summary..... 61

Table 4-2: Calibration of Sensor V-M Before and After..... 63

Table 4-3: Summary of Radial Sensor Positions ..... 64

Table 4-4: Operational Status of All Sensors Throughout Testing..... 66

Table 4-5: Summary of Hydrostatic Pressure Measurements in the Fossa ..... 73

Table 4-6: Normalized Final Displacement of Linear Acutator ..... 77

Table 4-7: Difference Between Maximum and Minimum Solid matrix stress Observations for t=1 to 3600 Seconds ..... 81

Table 4-8: Summary of Phase Shift Throughout Testing ..... 83

Table 4-9: Fluid Bath Temperature Drift Measured Between Start and Finish of Test ... 85

# List of Figures

Figure 1-1: Osseous anatomy of the pelvis. ..... 2

Figure 1-2: Femoral anatomy shown on cadaver ..... 3

Figure 1-3: Anatomy of the acetabulum ..... 3

Figure 1-4: Ligaments covering the joint capsule ..... 4

Figure 1-5: Depiction of femoroacetabular impingement showing: a) normal anatomy b) pincer impingement c) cam impingement. Adapted from Macfarlane et al. (2010). ..... 5

Figure 2-1: Composition of articular cartilage. Reproduced with permission from (Brinker & Miller 1999) ..... 13

Figure 2-2: Cartilage plug experiment schematic. Reproduced with permission from Adams et al. (1999). ..... 15

Figure 2-3: Results from cartilage plug experiments showing (a) stress profile across the plug and (b) linear relationship of measured stress to varying applied force at plug centre. Reproduced with permission from Adams et al. (1999). ..... 16

Figure 2-4: Traditional techniques for contact stress measurement a) femoral head mounted transducers (Brown & Shaw 1983) b) acetabular mounted transducers schematic (Adams & Swanson 1985) c) view of acetabulum with transducers (Mizrahi et al. 1981) d) Fujifilm covering femoral head (Levine et al. 2002) e) instrumented femoral prosthesis (Rushfeldt et al. 1981). All figures reproduced with permission. ..... 18

Figure 2-5: Etched hydrostatic pressure sensor (a) overall sensor, (b) section view of tip and (c) strain relief provided by steel housing when exposed to hydrostatic pressure. Reproduced with permission from Dennison and Wild (2008a). ..... 19

Figure 2-6: Schematic of contact force sensor. Reproduced with permission from Dennison et al. (2010). ..... 20

Figure 2-7: Synovial fluid pressure measured in the fossa of an intact hip specimen before and after labral resection. Reproduced with permission from Ferguson et al. (2003). ..... 28

Figure 2-8: (a) Forces acting on a full pelvis specimen; (b) angle, θ, of resultant force resolved using vectors; (c) hemipelvis potted with correction θ to maintain resultant force direction through joint. Reproduced with permission from Bay et al. (1997) ..... 32

Figure 3-1: Side view of contact stress sensor calibration setup ..... 34

Figure 3-2: Contact stress sensor calibration setup ..... 34

Figure 3-3: Hydrostatic pressure calibration setup ..... 37

Figure 3-4 : Environmental chamber with sensors located inside for temperature calibration ..... 38

Figure 3-5: (a) Contact stress sensors bundled to RTD temperature probe; (b) beaker of water inside environmental chamber with RTD probe and sensors at mid-depth ..... 39

Figure 3-6: Hydrostatic pressure sensors (left) and RTD probe (right) attached to thermal mass..... 40

Figure 3-7: (a) Adjustable alignment fixture for specimen potting (b) attached to laboratory stand and specimen while the blue PMMA hardens ..... 41

Figure 3-8: Three contact stress sensors inserted through the labrum in Specimen 2..... 43

Figure 3-9: Six contact stress sensors inserted into Specimen 3. ..... 43

Figure 3-10: Radial Position of sensors on 3-D model of pelvis..... 44

Figure 3-11: Surgical suite at CHHM showing a hip specimen secured in place on the hip distraction apparatus within the field imaging of the C-arm. ..... 45

Figure 3-12: (a) 25G x 1" needle and 0.010" wire trochar individually and (b) assembled. ..... 45

Figure 3-13: Window in anterior joint capsule used to insert three needles through labrum into acetabular cartilage of Specimen 2..... 46

Figure 3-14: Radiographs of needle for sensor insertion in acetabular cartilage with (a) needle tip inside rim of acetabulum and (b) inserted to full depth 15 mm. ..... 47

Figure 3-15: Insertion needle contacting bone/cartilage interface showing (a) digging action and (b) bouncing action (needle not to scale). ..... 48

Figure 3-16: Strain relief loop and three blue contact stress sensor insertion needles secured with sutures. Pressure sensor entering the fossa and green insertion needle are visible..... 49

Figure 3-17: Hydrostatic pressure sensor (faint line travelling horizontally at bottom) within the outline of fossa of Specimen 1 (H1340)..... 50

Figure 3-18: Sample biplanar radiographic images taken at planes 25º apart for Specimen 1. Lead beads are used to identify the AIIS and the insertion needles. ..... 52

Figure 3-19: Example of radial position angle, θ, relative to the line connecting the AIIS and joint centre. The angle is positive in the anterior direction..... 53

Figure 3-20: Material testing machine experimental setup showing (a) fluid bath containing specimen and (b) ball bearing parallels to eliminate traction forces..... 54

Figure 3-21: Adjustable fixture to mount femoral shaft to material testing machine; (a) angle of flexion is fixed at 13º, however, adduction is adjustable from 0º to 45º using the curved slot; (b) an aluminum block is used as a safety stopper..... 55

Figure 3-22: Compressive sinusoidal creep load profile ..... 56

Figure 3-23: Specimen in fluid bath surrounded by ice for overnight storage between tests ..... 57

Figure 3-24: Specimen 1 (a) before and (b) after resection of the anterior labrum leaving tabs where the contact stress sensors pass through the labrum..... 58

Figure 4-1: The typical linear relationship between wavelength response and applied calibration stress value for one trial of contact stress sensor V-P..... 60

Figure 4-2: Radial position of all sensors for (a) Specimen 1, (b) Specimen 2 and (c) Specimen 3. Positive angular displacement is anterior of the AIIS. The image of Specimen 3 (right hip) has been flipped horizontally to match the images of 1 and 2 (left hips)..... 63

Figure 4-3: Tilted view of acetabulum from Specimen 1 showing typical consistent insertion distance below the rim of the acetabulum..... 65

Figure 4-4: Cartilage surfaces from (a) Specimen 1 (cartilage deterioration at the insertion site of sensor V-L circled), (b) Specimen 2 and (c) Specimen 3 after disarticulation on the final day of testing. ..... 68

Figure 4-5 : Sensors passing through lesion in labrum of Specimen 3..... 70

Figure 4-6: Hydrostatic synovial fluid pressure and applied load vs time for (a) Specimen 2 and (b) Specimen 3. ..... 71

Figure 4-7: Hydrostatic synovial fluid pressure measured in the fossa vs. time for (a) Specimen 2 and (b) Specimen 3. For clarity, a one second moving average was used, starting at the first peak of the sinusoidal loading cycle at 4.0 sec and 5.2 sec for Specimens 1 and 2 respectively. ..... 72

Figure 4-8: Displacement of linear actuator and applied compressive load (pink) vs time for Specimen 2, shown as (a) absolute and (b) standardized relative to the peak value of the first sinusoidal cycle at 4.0 sec. Positive values indicate consolidation of the joint... 75

Figure 4-9: Standardized linear actuator displacement vs time for (a) Specimens 1, (b) Specimen 2 and (c) Specimen 3. For clarity, a one second moving average was used, starting at 3.3, 4.0 and 5.2 seconds for Specimens 1, 2, and 3 respectively. Positive values indicate consolidation of the joint. ..... 76

Figure 4-10 : Solid matrix stress vs. time, Specimen 1 sensors (a) V-I, (b) V-K and (c) V-L ..... 79

Figure 4-11: Solid matrix stress vs. time for Specimen 2 sensor V-K ..... 79

Figure 4-12: Solid matrix stress vs. time for Specimen 3 sensors (a) V-I and (b) V-P .... 79

Figure 4-13: Examples of contact stress sensor response phase shifts of 0, $\pi/2$, and $\pi$ from applied compressive load (pink) in Specimen 1 for (a) sensor V-K and (b) sensor V-I... 83

# List of Abbreviations

Anterior Inferior Iliac Spine.....AIIS

Anterior Superior Iliac Spine.....ASIS

Body Weight.....BW

Centre for Hip Health and Mobility..... CHHM

Fiber Bragg Grating.....FBG

Pubic Tubercle.....PT

Phosphate Buffered Saline..... PBS

Resistive Temperature Device..... RTD

# Acknowledgements

I would like acknowledge the direct contributions of Murray Wong and Kristel Leung, both summer students at the Centre for Hip Health and Mobility (CHHM). Murray adapted the RSA imaging technique in Section 3.6 to this project, collected the images and processed the data. Kristel assisted with specimen dissection and instrumentation. Your contributions were integral and the long hours did not go unnoticed. Good luck!

My supervisor, Dr. Peter Wild, opened many doors along this journey by offering positivity at challenging moments and stimulating critical thought. Peter, I would like to thank you for the patience, flexibility, and dedication to removing obstacles throughout this project. Dr. Chris Dennison, thank you for the time spent familiarizing me with your previous work and providing feedback throughout this journey.

This project was in collaboration with Dr. David Wilson and Dr. Mike Gilbart of the UBC Department of Orthopedics who provided resources, biomechanical expertise, and clinical guidance. Post-doctoral fellow Dr. Shahram Amiri contributed by making the RSA imaging protocol available. Specimens and facilities were provided by CHHM and iCord where researchers and staff were genuinely cooperative. Financial support from the National Science and Engineering Research Council of Canada is also acknowledged.

I would like to thank my parents, Irene and John, and sister, Elyse, for providing the supportive foundation that has allowed me to succeed. Without your encouragement and second-set-of-eyes, I could not have completed this thesis.

Kari-Jean, thank you for the calming conversations, caring messages and patience needed to watch someone close also dedicate himself in a second direction.

# Dedication

I would like to dedicate this thesis to all those in the world with an inextinguishable inquisitiveness, who embark on a lifelong path of learning despite not being granted the same academic opportunities that I humbly express gratitude for having been privileged with. I admire your strength to pursue learning in the face of adversity.

# Chapter 1: Introduction

This research project is focused on validating a system to measure stress in articular cartilage with the potential for future use in answering clinical research questions about osteoarthritis in the human hip. Subtle developmental deformities are thought to cause destructive increases in cartilage stress and may play a role in damaging anatomical structures such as the labrum which influence joint contact mechanics. There is a compelling need for a system to quantify changes in cartilage stress to better understand the role of deformities, injuries, and related corrective surgical procedures.

In this chapter, an overview of the relevant anatomy of the human hip creates a foundation for the following discussion of the clinical motivation for the project. The clinical motivation is used as a basis for the project's specific research objectives that are presented before concluding with an outline of the thesis organization.

## 1.1 Anatomical Background

The human hip is a synovial joint with a ball and socket design that connects the pelvis and femur. The pelvis is formed by the pubis, ishium and ilium bones that are fused after birth to create the acetabulum (Figure 1-1). The superior margin of the ilium is known as the iliac crest and terminates with a bony protrusion called the anterior superior iliac spine (ASIS). Separated from the ASIS by a notch, is the anterior inferior iliac spine (AIIS). The pubic tubercle (PT) is another bony protrusion located on the anterior aspect of the pubis bone (Martini 1998).

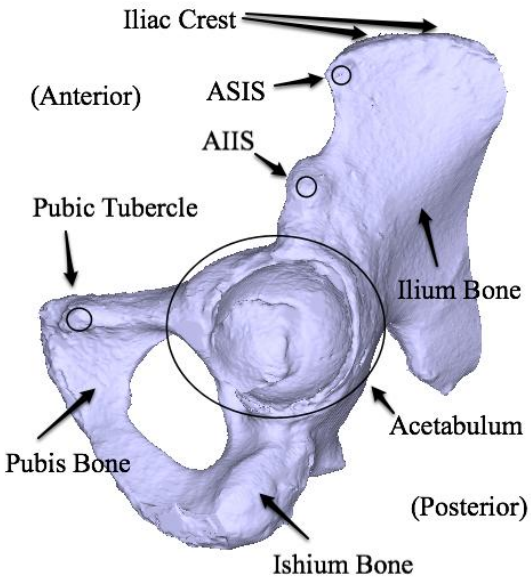


**Figure 1-1: Osseous anatomy of the pelvis.**

The spherical head of the femur and the lunate area of the acetabulum comprise the articular surfaces (Figure 1-2 and Figure 1-3). Both surfaces are covered in a layer of hyaline cartilage, which is a porous collagenous solid matrix. Synovial fluid fills the cartilage pores, intra-articular, and extra-articular joint spaces. The synovial fluid lubricates and provides nutrition for the cartilage (Afoke et al. 1980). Together, the porous cartilage matrix and synovial fluid form a biphasic material (Martini 1998).

Contained within the fovea capitis, a notch on the head of the femur, is the femoral attachment site of the ligamentum teres (Figure 1-2). The other end of the ligament is attached within the fossa of the acetabulum (Martini 1998).

The labrum is a fibrocartilage lip seal with a triangular cross section that extends around the lateral perimeter of the acetabulum from the attachment sites of the transverse acetabular ligament (Figure 1-3). The labrum is integrally attached to both the articular hyaline cartilage and the ossified perimeter of the acetabulum (Martini 1998).

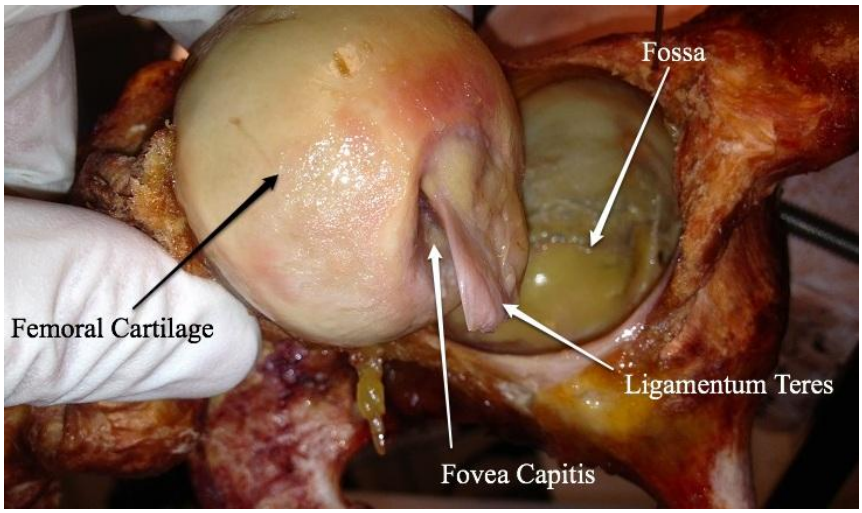


**Figure 1-2: Femoral anatomy shown on cadaver**

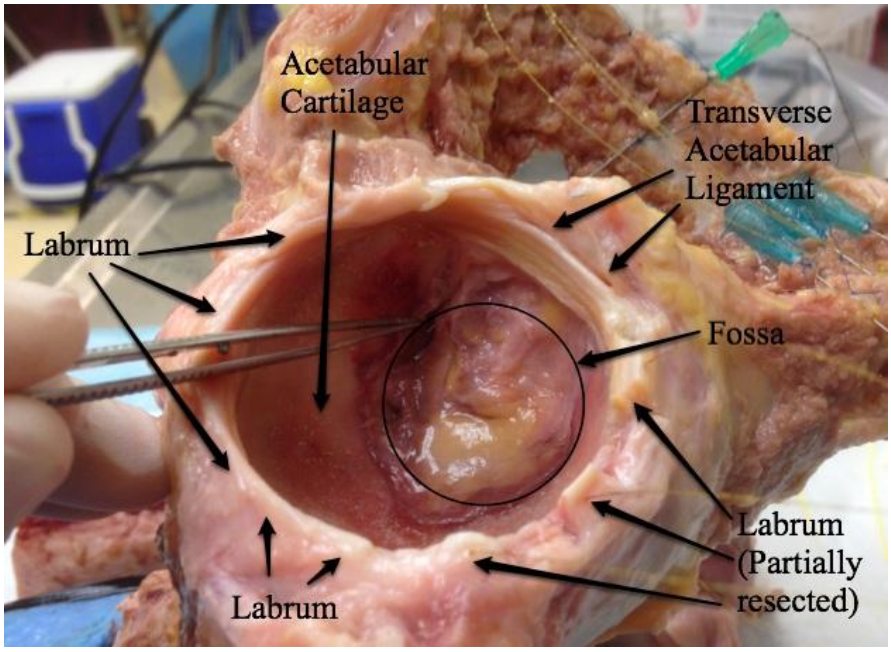


**Figure 1-3: Anatomy of the acetabulum**

Contained within the apex of the acetabulum is the fossa (Figure 1-3), a fat pad that provides a reservoir of synovial fluid for the intra-articular joint space. The transverse ligament spans the acetabular notch providing a medial seal for the intra-articular joint

space. On the interior side of the transverse ligament is the acetabular attachment site of the ligamentum teres (Martini 1998).

The fibrous joint capsule that contains the synovial is encapsulated by several major ligaments that stabilize the joint (Figure 1-4) (Martini 1998). The joint capsule of a healthy hip is thought to maintain a constant volume with no change in extra-articular pressure during flexion/extension and internal/external rotation owing to its hyperboloid shape (Wingstrand et al. 1990; Tarasevicius et al. 2007).

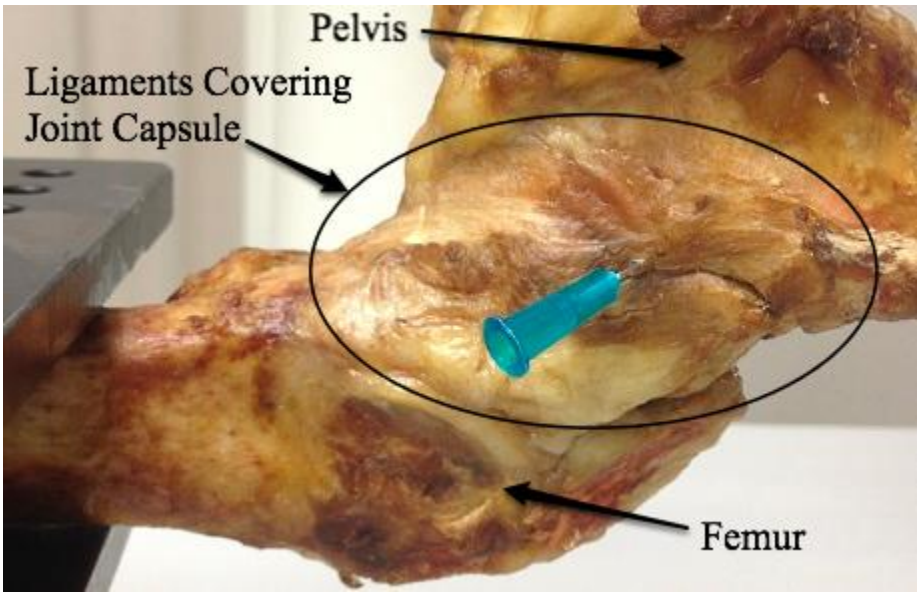


**Figure 1-4: Ligaments covering the joint capsule**

## 1.2 Clinical Motivation

Hip osteoarthritis is a painful and debilitating disease affecting a significant percentage of the population. As joint function becomes severely compromised by degeneration of articular cartilage, surgical intervention is required to resurface the joint with prosthetic

components. In the US alone, approximately 438,000 hip replacement procedures were performed in 2009, increasing to 456,000 in 2010 (HCUPnet 2012).

Early researchers suggested that a subtle developmental deformity of the femoral neck (Murray 1965) and mechanical or structural changes around the hip (Harris 1986) might correlate to subsequent development of osteoarthritis. This led to the development of the hypothesis that osteoarthritis is not primary, but secondary to subtle developmental defects including femoroacetabular impingement (FAI) (Ganz et al. 2003).

Two mechanisms of FAI exist. In the case of pincer impingement an overdeveloped acetabulum results in pinching of the labrum between the osseous rim of the acetabulum and the femoral neck (Figure 1-5b) at the extremes of motion. Cam impingement results from a localized thickening of the femoral neck causing binding of articular cartilage as the aspheric femoral head rotates within the acetabulum (Figure 1-5c) (Macfarlane & Haddad 2010).

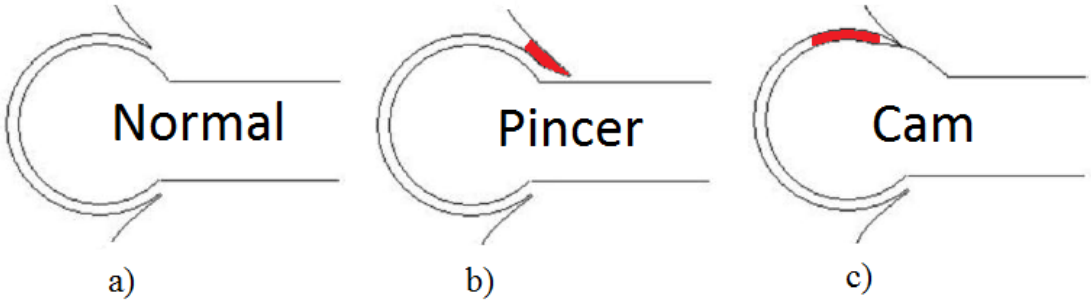


**Figure 1-5: Depiction of femoroacetabular impingement showing: a) normal anatomy b) pincer impingement c) cam impingement. Adapted from Macfarlane et al. (2010).**

Impingements are thought to locally elevate solid matrix stress on cartilage structures (Beck et al. 2005), especially in the case of cam scenarios where circumferential labral lesions and deep cartilage cleavages have been observed (Ganz et al. 2003; Beck et al. 2005). Early surgical intervention aims to modify osseous anatomy to reduce these local

stress concentrations (Leunig et al. 2009). However, it is unclear how much the deformity should be reduced and where exactly to remove the bone. Developing a technique to measure the solid matrix stress in articular cartilage could provide quantitative information that could be compared pre- and post-procedure in cadaveric specimens. Those measurements could ultimately contribute an increase in preventative surgical intervention in younger asymptomatic individuals before damage to cartilage occurs, reducing future care and associated health care costs.

In addition to damage to the acetabular cartilage, pathology of the labrum is often observed in the early stages of osteoarthritis in individuals with FAI (Ganz et al. 2003; Macfarlane & Haddad 2010). *Ex vivo* experimental findings by Ferguson et al. (2003) support the hypothesis from earlier modelling studies (Ferguson et al. 2000a; Ferguson et al. 2000b) that the labrum functions as a lip seal to maintain hydrostatic synovial fluid pressure within the intra-articular space. It is accepted that articular cartilage is a biphasic material where the total contact stress across a contact interface is split between fluid and solid matrix stresses (Park et al. 2003; Pearle et al. 2005; Ateshian 2009). Therefore, it is hypothesized that if the integrity of the labrum seal is compromised, the decrease in synovial fluid hydrostatic pressure would increase cartilage solid matrix stress and strain to maintain equivalent load transfer (Ferguson et al. 2003).

Prior to the work of Ferguson et al., *ex vivo* studies of the total contact stress acting on the cartilage surfaces of the hip were done (Day et al. 1975; Brown et al. 1978; Mizrahi et al. 1981; Rushfeldt et al. 1981; Brown & Shaw 1983; Adams & Swanson 1985; Afoke et al. 1987; Macirowski et al. 1994; Bay et al. 1997; von Eisenhart-Rothe et al. 1997; von Eisenhart et al. 1999). The various methods utilized in these studies are summarized in

Section 2.3, however, a common limitation is that disarticulation of the joint is required to instrument the specimen. Disarticulation compromises the labrum, permanently altering the seal of the intra-articular joint space and thus potentially increasing the solid matrix stress on the articular cartilage.

As a result of the frequently observed coexistence of labral injury and osteoarthritis in patients with FAI, it remains unclear if cartilage damage occurs as a result of labral injury from FAI, or if FAI causes destructive increases in contact stress independent labral pathology. Several clinical questions arise. How should labral tears be treated? Is re-attachment of the labrum effective? Does labral resection increase solid matrix stress in the cartilage and accelerate the deterioration of cartilage?

To explore the relationship between FAI, cartilage solid matrix stress and labral pathology, a technique to measure solid matrix stress in the cartilage is required. As a first step, that technique could be used to validate the hypothesis that labral resection decreases synovial fluid pressure, increasing cartilage solid matrix stress.

## 1.3 Objectives

The goal of this research is to validate a minimally invasive continuous measurement system to simultaneously quantify solid matrix stresses acting on articular cartilage and synovial fluid pressure in intact cadaveric human hip joints. A successful outcome could allow future *ex vivo* comparison of measurements on cadavers from before and after performing surgical procedures for FAI or labral injury. The specific objectives of this work are to:

1) Establish the day to day repeatability of the measurement method with tests on three sequential days for each of three intact cadaveric specimens by applying a cyclic load representative of the standing phase of gait for one hour.

2) Confirm the hypothesis that a reduction in magnitude of hydrostatic synovial fluid pressure as a consequence of labral resection, results in a higher magnitude and/or rate of change of the solid matrix stress in the articular cartilage.

### 1.4 Organization of Thesis

This thesis is organized into chapters. Chapter 1 explains how this project fits within the broader vision of developing a new method to study femoracetabular impingement. In Chapter 2, the relevant background material described in the literature is summarized. Chapter 3 provides a detailed outline of the experimental setup and methods. The novel technique for sensor insertion and fixation which comprises the primary contribution of this work is described in this chapter. Chapter 4 is a discussion of the results and findings. Conclusions and recommendations for future work are included in the final Chapter 5.

# Chapter 2: Contact Mechanics of the Human Hip

In this chapter, a review of the literature is intended to present an understating of contact mechanics, methods for quantification of contact properties, and results from previous studies all taken within context of the clinical motivation and objectives of this thesis.

The chapter begins with a discussion of the anatomical region of interest within the human hip, derived from the clinical and experimental observations followed by an explanation of the specific behaviour of the biphasic cartilage material, located in this region, during load transfer across the joint. The techniques used to measure properties of contact mechanics are then summarized before the results from previous *ex vivo* studies are presented. The subsequent section on the labrum's role in sealing the intra-articular joint space summarizes the previous work on which the research objectives and experimental methods for this thesis are founded. Lastly, for *ex vivo* experiments, an understanding of correct physiological alignment during potting is at the literal foundation of *ex vivo* experimentation.

## 2.1 Anatomical Region of Interest

In order to align with the long-term vision of creating a measurement system for the purpose of *ex vivo* study of pre- and post-operative contact mechanics of cadaveric hip joints with FAI, understanding the appropriate region of interest is critical.

Cam impingement tends to exist predominately in males, occurring more frequently in active athletes (Keogh & Batt 2008). The deformity is most frequent on either the anterior or lateral aspects of the femoral neck commonly resulting in impingement during

flexion and internal rotation (Ito et al. 2001; Ganz et al. 2003; Beck et al. 2005; Laude et al. 2007; Kassarjian et al. 2007; Ganz et al. 2008).

In the case of pincer impingement, an effective increase in coverage by the acetabulum results in contact of the femoral neck on the osseous rim at the extremes of joint motion, pinching the labrum (Ganz et al. 2003; Beck et al. 2005; Kassarjian et al. 2007; Ganz et al. 2008). Pincer impingement is most prevalent in the female population. Osteoarthritis progresses slower as the labrum is thinned by compression but stress on the acetabular cartilage is not mechanically amplified locally as in the cam scenario (Beck et al. 2005; Ganz et al. 2008).

The most likely situation is a combination of impingement mechanisms (Beck et al. 2005) where regions of locally elevated contact stress exist in the anterior and lateral rim of the acetabular cartilage and/or within the labrum.

Early contact mechanics studies were aimed at determining the magnitude and distribution of joint space (Afoke et al. 1980; Afoke et al. 1984) using a casting process in loaded configurations. This concept of casting has also been used in combination with the pressure sensitive film discussed in Section 2.3, in a comprehensive attempt to characterize contact within the joint space (von Eisenhart-Rothe et al. 1997; von Eisenhart et al. 1999). Since the existence of joint space implies a lack of contact by articular cartilage and therefore a lack of contact stress in the cartilage matrix, it is relevant to the current work to understand the theories surrounding joint space in the human hip.

Considerable variability in the size of the joint space in different positions of gait at comparable loads and between specimens was observed (Afoke et al. 1980; Afoke et al.

1984). Contact areas at small loads of 0.25 x body weight (BW) existed around the periphery of the lunate acetabular surfaces near the labrum for 44% (von Eisenhart-Rothe et al. 1997) and 83% of specimens (von Eisenhart et al. 1999) extending toward the interior aspect of the acetabulum at higher loads of 3 x BW(von Eisenhart-Rothe et al. 1997). The remaining specimens experience the opposite pattern where initial contact was confined to the acetabular roof, spreading to the anterior and posterior lunate surfaces as load increased (von Eisenhart-Rothe et al. 1997). In the 1997 study, only the stance phase of gait was evaluated, whereas in 1999 the authors simulated four phases of gait and observed the variation of the initial contact patterns between phases to be minimal.

A universal finding was that specimens frequently exhibited some form of joint space bordering on the fossa that decreased or eventually disappeared with increasing load, while less common were the scenarios of congruent joints or a femur head that appeared smaller in diameter than the acetabulum (Afoke et al. 1980; Afoke et al. 1984; Eckstein et al. 1997; von Eisenhart-Rothe et al. 1997). Sufficient evidence was not gathered in multiple studies (Afoke et al. 1984; von Eisenhart-Rothe et al. 1997) to support the theory, proposed by Bullough et al. (1973), that joint incongruity decreases with age.

Terayama et al. (1980) studied the joint space by sectioning specimens frozen in a loaded configuration. Unlike casting studies, disarticulation was not required and the effects of synovial may have been captured. Examination of the sections showed that the cartilage surfaces had deformed and become congruent, but a fluid filled space ranging from 0.2 to 0.6 mm thick remained, completely separating the cartilage layers. Later analytical models suggest this fluid or gel film is in the order of $10^{-3}$ to $10^{-4}$ mm

(Hlavacek 2002). During a pilot experiment, Dennison et al. (2011) inserted a single 240 μm diameter contact stress sensor into a single location within the intra-articular joint space. As the joint was loaded to simulate single leg standing, the sensor registered contact readings, implying a joint space of less than 240 μm in that location.

Given the prevalence of cam lesions in the anterior and lateral aspects of the femoral neck, there is a high probability of being able to measure increased cartilage contact stress on the corresponding aspects of the acetabulum. Frequent observations that contact initiates around the perimeter of the acetabulum, particularly in the anterior and posterior lunate horns, with joint space disappearing last on regions that border the fossa, indicate favourable conditions for measuring articular contact stress around the perimeter of the acetabulum.

## 2.2 Load Transfer Across Biphasic Articular Cartilage Tissue

Articular cartilage is complex biphasic material consisting of both solid matrix and fluid phases. The solid matrix is composed of a firm gel containing polysaccharide derivatives called chondroitin sulfates which form complexes with proteins to create proteoglycans (Martini 1998, p.128). This porous solid matrix is filled with thick, viscous synovial fluid similar to interstitial fluid but with a high concentration of proteoglycans secreted by cells of the synovial membrane (Martini 1998, p.256). Orientation of collagen fibers within the cartilage solid matrix changes as a function of depth (Pearle et al. 2005) as shown in Figure 2-1 below.

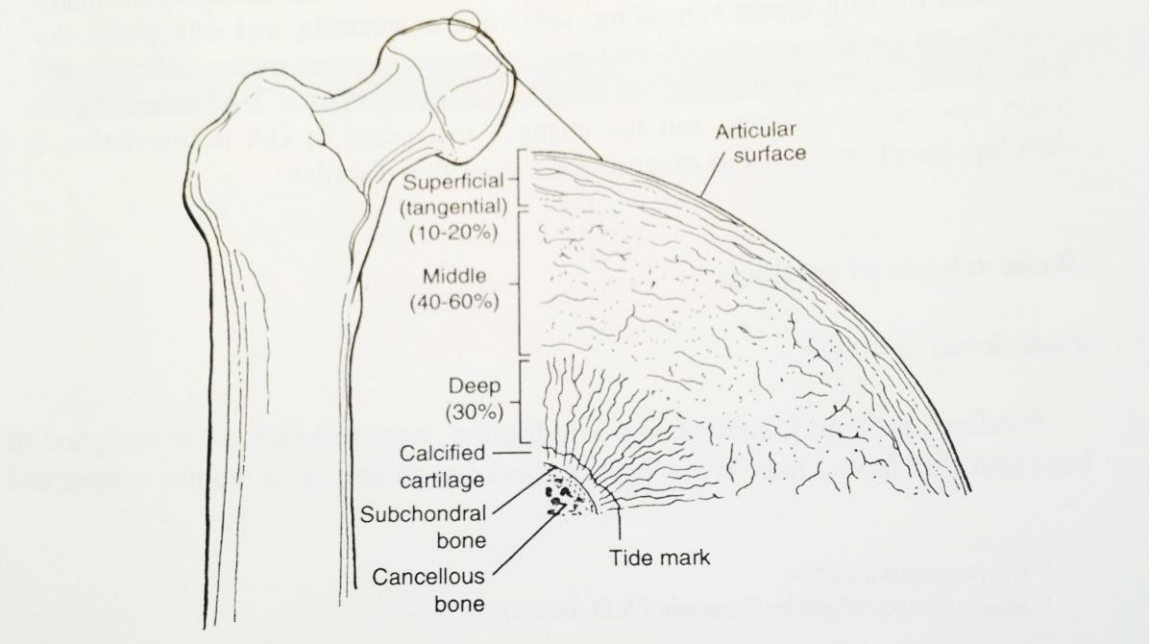


**Figure 2-1: Composition of articular cartilage. Reproduced with permission from (Brinker & Miller 1999)**

The highest density of collagen fibers exists in the superficial or tangential zone where these strong tensile fibers are oriented parallel to the surface resulting in the lowest compressive modulus of the three layers (Pearle et al. 2005). The middle zone contains randomly oriented collagen fibers with an increasingly stiff modulus, while the radial oriented fibers of the deep zone result in the stiffest cartilage with the lowest water content (Park et al. 2003; Pearle et al. 2005). Strain gradients ranging from high at the tangential zone, to low at the deep zone have been demonstrated in porcine specimens (Park et al. 2003; Erne et al. 2005).

The permeability of the solid phase is low causing high interstitial fluid pressurization in the cartilage pores as opposing surfaces are pressed together (Pearle et al. 2005; Ateshian 2009). This interstitial pressurisation serves as a mechanism of load transfer across the joint leaving only a small remainder to be supported by the solid matrix

(Ateshian 2009). In experiments with human cartilage, Park et al. (2003) observed that the maximum fluid load support was 79 ± 11% and 69 ± 15% at the superficial and deep zone respectively, with the cartilage solid matrix supporting the remainder.

Using biphasic theory (Mow et al. 1980), the Euler-Cauchy stress tensor at a cartilage contact interface can be split into apparent fluid and solid matrix stresses (Ateshian 2009). Assuming a state of generalized plane strain exists for small regions of articular cartilage (Dennison et al. 2010), the problem can be considered in two dimensions. The total contact stress, $\sigma$, acting on a contact interface between biphasic articular cartilage and an opposing bearing surface is a function of fluid pressure, $\sigma_f$, and the solid matrix stress, $\sigma_m$. The fraction of apparent contact area, $\varphi$, where the solid matrix of one bearing surface contacts the opposing bearing surface, is derived from the porosity of the cartilage.

$$\sigma = (1-\varphi)\cdot\sigma_f + \sigma_m \qquad \text{(Eqn 1)}$$

The term, $(1-\varphi)\cdot\sigma_f$, represents to total amount of contact stress supported by the synovial fluid and $\sigma_m$ can further be defined as:

$$\sigma_m = \varphi\cdot\sigma_f + \sigma_d \qquad \text{(Eqn 2)}$$

Where, $\sigma_{d,}$ represents the stress contributed by solid matrix deformation. The term, $\varphi\cdot\sigma_f$, is the hydrostatic stress supported by the solid matrix, which inherently couples the fluid and solid matrix phases analytically (Cowin 1990). .

Adams et al. (1999), performed an experiment on square cartilage plugs 12 mm x 15 mm in unconfined compressions using the setup depicted in Figure 2-2. A 900 μm transducer needle with a diaphragm 30 μm thick (McNally et al. 1992) mounted with a miniature strain gauge was used to measure the average pressure over the transducer area of 1.5 mm x 0.75 mm (Adams et al. 1999).

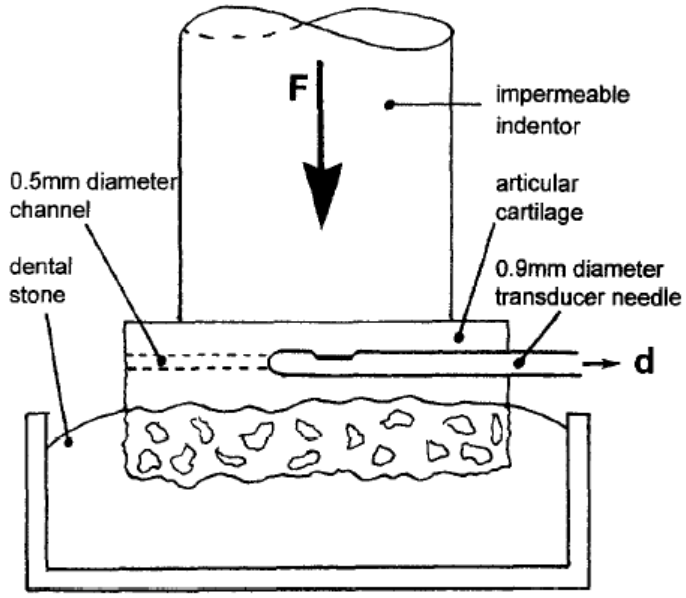


**Figure 2-2: Cartilage plug experiment schematic. Reproduced with permission from Adams et al. (1999).**

With the samples loaded in unaxial, unconfined compression to 2 MPa (Adams et al. 1999), the transducer needle was drawn horizontally through the specimen with the pressure sensitive diaphragm in both vertical and horizontal orientations creating the stress profiles shown in Figure 2-3-a. The linearity of the pressure transducers was verified by steadily increasing the compressive force with the results shown in Figure 2-3-b. In both cases, stresses recorded with the transducer oriented in the vertical direction appeared to differ from the horizontal direction by approximately 0.5 to 1 MPa.

This difference in stress may represent the order of magnitude of the solid matrix stress, $\sigma_m$, from Eqn. 2.

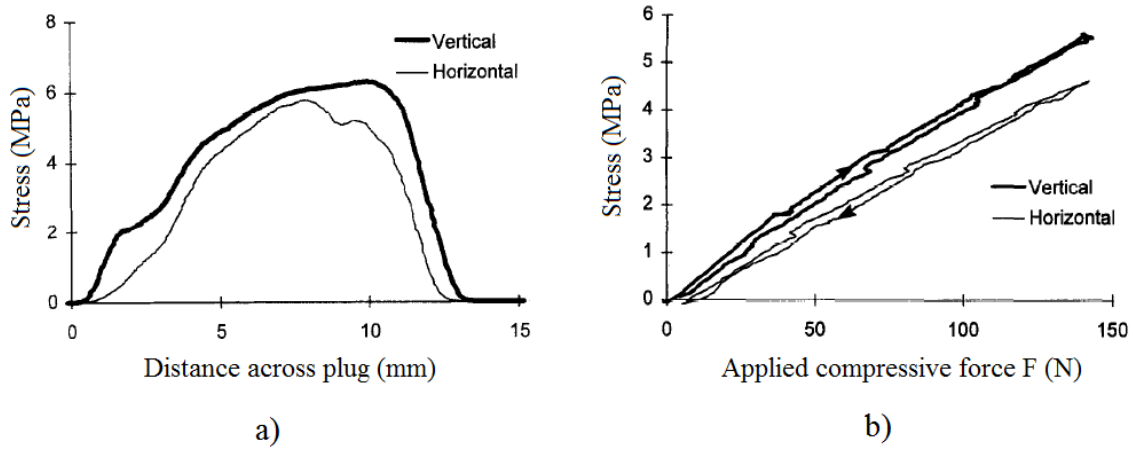


**Figure 2-3: Results from cartilage plug experiments showing (a) stress profile across the plug and (b) linear relationship of measured stress to varying applied force at plug centre. Reproduced with permission from Adams et al. (1999).**

It has been demonstrated that cartilage wear is coupled with increases in the coefficient of friction between the cartilage surfaces (Forster & Fisher 1999; Lizhang et al. 2011) and that the frictional force on these surfaces is proportional to the load carried by the solid matrix (Ateshian 2009). Increases in the solid matrix stress could therefore be a potential indicator of conditions within the joint that are detrimental to cartilage health.

## 2.3 Sensors for *Ex Vivo* Contact Measurements in the Hip

Several types of physical sensing mechanisms have been employed in attempts to measure the contact stresses on articular cartilage in the human hip joint. Brown and Shaw (1983) pioneered the use of miniature piezoelectric transducers (Brown et al. 1978) mounted on the femoral head (Figure 2-4a). Alternatively, several authors have made similar measurements by fixing transducers in the acetabulum (Figure 2-4b/c) (Mizrahi et

al. 1981; Adams et al. 1999). These methods all offer discrete measurements of contact pressure on the cartilage surfaces. A limitation of both of these methods is the sensitivity of the transducers to being mounted either flush with the cartilage surface, or flush with the end of blind bores to ensure minimal artifact in measurements. For sensors mounted in the acetabulum, dehydration and resulting changes in cartilage properties were thought to be the most significant sources of error (Mizrahi et al. 1981; Adams & Swanson 1985).

The most common method employed to date is the use of pressure sensitive film (Figure 2-4d), such as Fuji Prescale® (Fuji Photo Film Co. Ltd., Tokyo, Japan), to make continuous pressure maps over the entire femoral head (Afoke et al. 1987; Konrath et al. 1998; Bay et al. 1997; von Eisenhart-Rothe et al. 1997; von Eisenhart et al. 1999; Anderson et al. 2008). Wu et al. (1998) modelled the effect of inserting pressure sensitive films on articular joint mechanics. The film effective thickness of 0.30 mm and effective average compression modulus that is 100-300 times greater than articular cartilage were found to alter the maximum true contact pressures by 10-26 percent resulting in theoretical measurement errors as high as 14-28 percent (Wu et al. 1998).

Lastly, measurements have been made with instrumented femoral endoprosthesis (Figure 2-4e) (Rushfeldt et al. 1981). The prosthesis is manufactured with pressure sensitive diaphragms and transducers inside the spherical surface. A limitation of using a spherical endoprosthesis instead of the natural femoral head is that local contact pressures are extremely sensitive to subtle changes in geometry of the joint (Anderson et al. 2010). Furthermore, incorrect sizing of the prosthetic femoral head has a dramatic impact on the measured contact pressures (Rushfeldt et al. 1981).

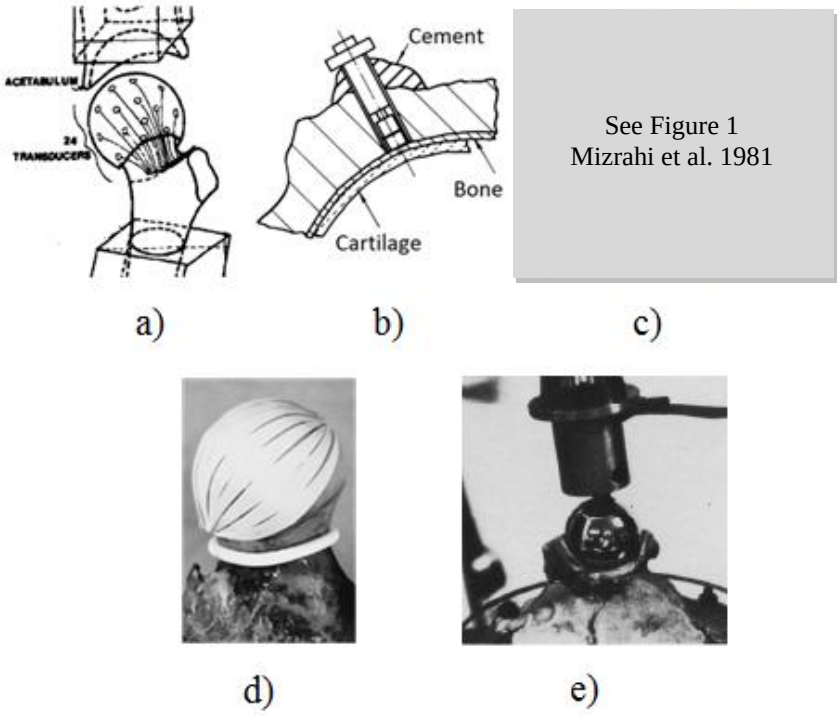


**Figure 2-4: Traditional techniques for contact stress measurement a) femoral head mounted transducers (Brown & Shaw 1983) b) acetabular mounted transducers schematic (Adams & Swanson 1985) c) view of acetabulum with transducers (Mizrahi et al. 1981) d) Fujifilm covering femoral head (Levine et al. 2002) e) instrumented femoral prosthesis (Rushfeldt et al. 1981). All figures reproduced with permission.**

Dennison et al. (2010) performed a pilot study using fiber Bragg grating (FBG) sensors to measure the synovial fluid pressure and contact stress between articular cartilage surfaces simultaneously in two intact hip specimens. The hydrostatic pressure sensor shown in Figure 2-5 below was manufactured with a 10 mm fiber Bragg grating (FWHM BW < 0.2 nm, reflectivity > 90%, Polyimide™ fiber, Micron Optics, Atlanta, GA) by reducing the fiber diameter to 50 μm using hydrofluoric acid to improve sensitivity similar to the design of Dennison and Wild (2008a). A silicon (Down Corning 3140 RTV, Midland, MI) diaphragm at the distal tip of the sensor acts as the effective sensing area.

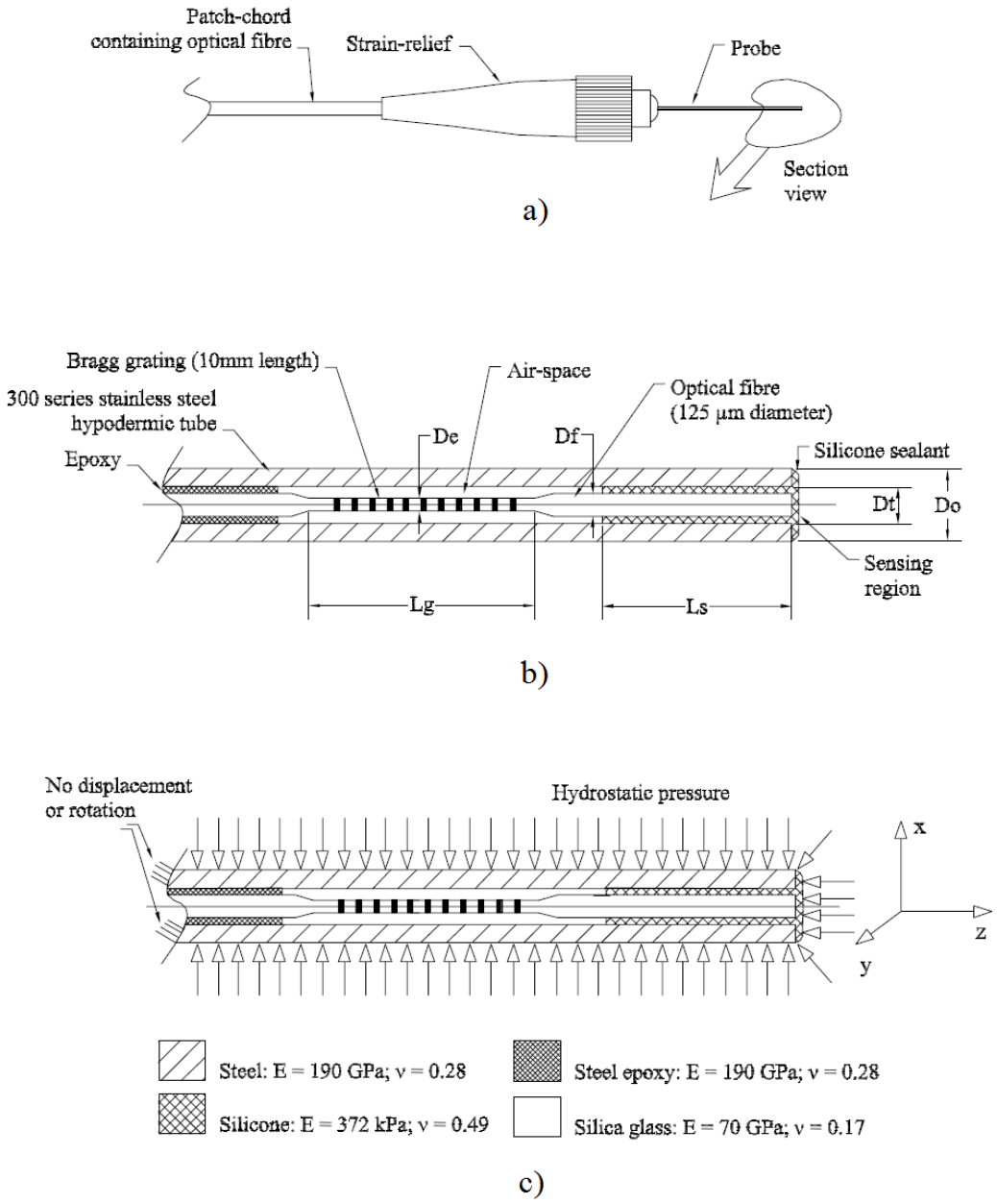


**Figure 2-5: Etched hydrostatic pressure sensor (a) overall sensor, (b) section view of tip and (c) strain relief provided by steel housing when exposed to hydrostatic pressure. Reproduced with permission from Dennison and Wild (2008a).**

The transverse contact stress sensor used by Dennison et al. (2010) was assembled according to the schematic shown in Figure 2-6 using a 1 mm FBG (FWHM BW < 1.5 nm, reflectivity > 50%, Polyimide™ fiber, Micron Optics, Atlanta, GA) grating etched

to 70 μm in diameter. The 15 mm length volume maintaining 240 μm diameter (32 gauge) Polyimide™ sheath creates a Poisson effect on the concentric silicon annulus (Dow Corning -1953, Midland, MI) transforming transverse contact stress on the sheath into detectable axial strain in the FBG (Dennison et al. 2010). These contact stress sensors offer a novel method to study contact stress on articular surfaces that can be inserted into the joint without disarticulation resulting in a more physiologically representative scenario than previous studies.

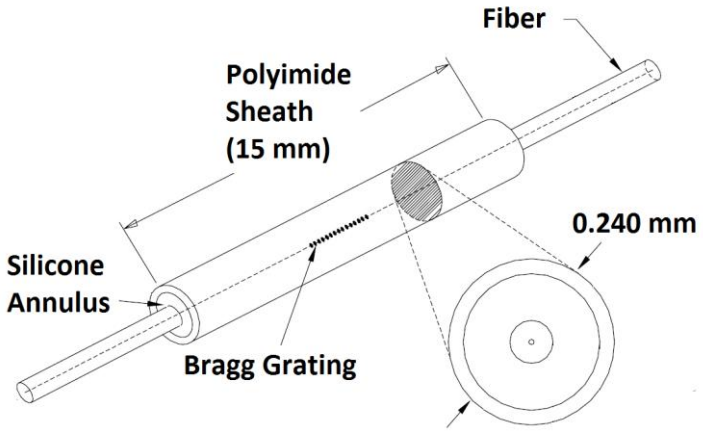


**Figure 2-6: Schematic of contact force sensor. Reproduced with permission from Dennison et al. (2010).**

Disarticulation is one of the major limitations with existing sensing techniques in light of recent work highlighting the importance of the labrum seal and synovial fluid in load transfer across the joint. The modelling work of Ferguson et al. (2000a; 2000b) explains the importance of the labrum in maintaining hydrostatic pressure within the joint which is integral to reducing the magnitude of stress on the solid matrix phase of the articular cartilage. An *ex vivo* study confirmed this hypothesis by using a 1 mm diameter x 0.30 mm pressure transducer implanted within the fossa to measure the hydrostatic synovial

fluid pressure within the intra-articular joint space of intact specimens before and after labral resection (Ferguson et al. 2003).

In summary, to improve upon the limitations of disarticulation and introduction of a film into the joint space, a sensing technology is required that can be inserted into specimens where the joint remains intact. Achieving this with sensors 0.24 mm in diameter located within the joint space (Dennison et al. 2010), or implanted in articular cartilage, may serve to reduce impact on contact mechanics when compared with the use of a continuous film throughout the joint space.

## 2.4 Key Findings of *Ex Vivo* Contact Studies

Using load-deflection curves, Day et al. (1975) found the average stress on the acetabular cartilage surface was 1.54 MPa ± 0.38 MPa, and the maximum recorded stress was 2.2 MPa. These values represent average stress over substantial areas of the acetabular cartilage and can be compared to the values in Table 2-1 below, which are derived from either discrete or continuous sensing techniques for the stance phase of gait. In most cases, peak pressures are substantially higher than the average stress over the contact area, supporting the theory that local variations in cartilage properties, congruency, geometry, and impingement result in high peak contact stress.

**Table 2-1: Summary of Peak and Average *Ex Vivo* Contact Stress Measurements for Stance Phase of Gait**

| Author | Max Applied Load | Peak Stress [MPa] | Average Stress [MPa] | Peak/Average [MPa] |
|---|---|---|---|---|
| Day 1975 et al. (1975) | 1350 – 2250 N | 2.2[1] | 1.54 | ~ 1.4 |
| Rushfeldt et al. (1981) | 1350 – 2250 N | 9.3 - 11 | 2.53 – 3.72 | ~3.3 |
| Mizrahi et al. (1981) | 500 N | 1.2 | | |

[1] Represents the maximum average stress from the multiple sections of contact area

| | | | | |
|---|---|---|---|---|
| Brown and Shaw (1983) | 2700 N | 8.8 | 2.92 | 3.02 |
| Adams and Swanson (1985) | 4.17 x BW | 5.26 – 8.57 | | 1.8 – 3.3 |
| Afoke et al. (1987) | 1.3 – 2.15 x BW | 2.9 – 8.6 | | |
| Michaeli et al. (1997) | 800 - 1200 N | ~ 8 | | |
| von Eisenhart-Rothe et al. (1997) | 0.5 BW / 3 x BW | 5 - 7 / 8 - 9 | | |
| Konrath et al. (1998) | BW | 5.7 - 7.5 | 3.3 - 4.6 | |
| Von Eisenhart et al. (1999) | 3.45 x BW | 7.7 ± 1.95 | | |
| Anderson et al. (2008) | 2.38 – 2.6 x BW | > 10 | 4.4 - 5.0 | |
| Dennison et al. (2010) | 0.75 x BW | 0.12[2] | | |

In an early study, several anomalies in the acetabular cartilage were frequently observed. Firstly, the presence of a thin triangular shaped layer of fibrocartilage located at the zenith of the acetabulum of some specimens was observed to carry double the average contact stress (Day et al. 1975). The second was a lunate band of softened and/or delaminated cartilage along the lateral rim of the acetabulum which generally supported a stress approximately that of the average throughout the joint (Day et al. 1975). This later anomaly may be consistent with the recent theory of cam impingement which tends to produce flap-like cleavage lesions in a similar area (Beck et al. 2005; Ganz et al. 2008; Chegini et al. 2009).

There appear to be three main patterns of contact pressure distribution throughout all the *ex vivo* studies as summarized below in Table 2-2. Terminology differs slightly between publications, however, qualitatively the explanations of the three terms in the table are consistent.

**Table 2-2: Explanation of Common Contact Patterns on the Acetabular Cartilage Surface**

| Distribution | Explanation |
|---|---|

[2] Based on a single measurement location within the specimen

| | |
|---|---|
| Bicentric | • Double maximum peaks, one located on each of the anterior and posterior lunate surfaces<br>• Consistent with incongruent joint hypothesis |
| Axisymmetric | • Single stress peak in the superior acetabular dome<br>• Consistent with hypothesis that femur head could be smaller in diameter than the acetabulum in these specimens |
| A-P Ridge | • Combination of bicentric and axisymmetric patterns<br>• Resembles a ridge of peak stress running roughly anterior-posterior in orientation |

The most commonly observed contact patterns for the single leg stance phase of gait on hemipelvis specimens were the bicentric or A-P ridge profiles with large variation in the gradient of the distributions between individuals (Rushfeldt et al. 1981; Brown & Shaw 1983; Afoke et al. 1987; Bay et al. 1997; von Eisenhart et al. 1999). It is hypothesised that the geometry of the hip joint is incongruous, analogous to a spherical ball thrust into a gothic arch where the arch is engineered to deform and distribute contact stress over the entire surface as load increases (Afoke et al. 1980). The bicentric profile in particular, supports the hypothesis of incongruent geometry by design from observations of more even distribution of contact stress with increasing loads (von Eisenhart-Rothe et al. 1997; von Eisenhart et al. 1999).

Konrath et al. (1998) performed a study observing that contact originated around the peripheral margin of the acetabulum, again supporting the incongruent theory. The authors concluded that in disarticulated full pelvis specimens, the effect of resecting the labrum, transverse ligament or both, had a negligible effect on contact stress and distribution. (Konrath et al. 1998). However, Ferguson et al. (2003) later performed an *ex vivo* study of hydrostatic pressure within the fossa of intact hip specimens which was thought to represent the hydrostatic fluid pressure within the intra-articular joint space. In

that study, labral injury resulted in a decreased ability of the joint to maintain synovial fluid pressure. The author hypothesized that the decrease in fluid pressure may have resulted in an increase in solid matrix stress to maintain the overall resultant force transfer across the joint, however, these contact stresses were not measured (Ferguson et al. 2003).

Though limited in resolution by only four transducers, the study by Mizrahi et al. (1981) suggests that the zenith of the acetabulum is the least likely area to be subject to excessively high pressure in any joint position, again suggesting the load is commonly transferred in either a bicentric or A-P ridge pattern. Rushfeldt et al. (1981) performed a study of only two specimens but observed one case of each of the bicentric and axisymmetric distributions. Rushfeldt et al. (1981) also noted that a time dependant decrease in peak and average contact stress was observed in both specimens.

By contrast, the research of Adams and Swanson (1985) using discrete instrumentation of the acetabulum, and supported by the film study of von Eisenhart-Rothe et al. (1997), observed that the transducers at or near the zenith of the acetabulum frequently experienced the highest stress. As noted in Table 2-1, the highest loads were applied by Adams and Swanson (1985) and may have resulted in excessive deformation of cartilage and osseous anatomy leading to high stress on the superior dome of the acetabulum. Partial dehydration of the cartilage, which changes its dimensions and properties, was thought to be the greatest source of error affecting the accuracy of the transducer calibration (Adams & Swanson 1985).

In specimens with the axisymmetric distribution, contact at the zenith of the acetabulum was consistently present at both low and high loads (von Eisenhart-Rothe et

al. 1997) and often in all phases of gait (Afoke et al. 1987; von Eisenhart et al. 1999). The axisymmetric distribution is hypothesized to arise from a femoral head that is smaller in diameter than the acetabulum, concentrating the load on a single point of contact at the stress pole. An experiment measuring contact stress as a function of fit indicated that a prosthesis undersized by 2 mm resulted in a roughly axisymmetric distribution (Rushfeldt et al. 1981).

Brown and Shaw (1983) observed that for small angles of flexion (10°) the contact pattern shifted over the femoral head correspondingly. Beyond 10°, resemblance with the neutral pattern was not as clear. The inferred average contact area was approximately 17 $cm^2$. In 92% of cases, the peak stress fell within 30° of the line of action of the joint load resultant, but no consistent direction of deviation from the loading axis was observed (Brown & Shaw 1983).

Several authors have validated that the experimentally determined load based on sensor response is consistent with the applied load as shown in Table 2-3, adding credibility to the calibration of sensing mechanisms.

**Table 2-3: Comparison of Experimentally Measured Load to Actual Applied Load**

| Author | Experimental Determined Load [N] | Actual Applied Load [N] |
|---|---|---|
| Brown and Shaw (1983) | 12.9% higher | - |
| Bay et al. (1997) | 2265 +/- 835 (intact)<br>2304 +/- 397 (explanted) | 2194 +/- 199 |
| Konranth et al. (1998) | 2230 +/- 1195 | 2060 +/- 890 |

Bay et al. (1997) performed a unique film contact study comparing observations from complete intact pelvic specimens including simulated abductor muscle function and

vertical loading of the sacrum. The same specimens were then explanted into the hemipelvis configuration typically used. The intact configuration exhibited contact in anterior and posterior regions, while explanting the configuration resulted in a 60% and 65% decrease in contact area of the posterior and anterior regions respectively. Mean stress increased in the superior acetabular dome of the explanted configurations by 28% with downward trends observed in the pressures of the other regions. This suggests that the pelvis, when functioning as a whole, is able to deform in a manner that serves to distribute stress optimally throughout the joint (Bay et al. 1997).

In the pilot study by Denison et al. (2010), one single point fiber optic transverse contact stress sensor with a 1 mm gauge length was inserted into the intra-articular space near the superior region of the acetabulum. Hydrostatic pressure was simultaneously recorded within the fossa as the joint was subject to a cyclic force of 0.75 x BW ± 0.25 x BW in an orientation representative of the stance phase of gait. The absolute contact stress inferred from the force response of the sensor was low as shown in Table 2-1. This pilot study represents only a single point within a highly variable distribution, however, the contact stress and hydrostatic pressure readings correspond well with the cyclic applied load adding credibility to the sensing method.

The *ex vivo* research to date has confirmed several important aspects regarding the magnitude and distribution of contact pressure throughout the joint. Both discrete sensing and continuous pressure sensitive film methods tend to produce recurring patterns of bicentric, A-P ridge, or axisymmetric distributions. Of these, the bicentric or ridge patterns tend to be the most frequent with the bicentric pattern supporting the concept of incongruent joint geometry by design. The axisymmetric distribution, while less

common, is indicative of an undersized femoral or prosthetic head. Lastly, the validation that experimentally determined loads are comparable to known applied load adds credibility to the calibrations of these measurement techniques.

## 2.5 Role of the Labrum as a Hydrostatic Seal

Several studies support the hypothesis that the labrum forms a lip seal against the femoral head serving to maintain hydrostatic pressure synovial fluid pressure in the joint space and reduce solid matrix stress on the cartilage. This has been modelled (Ferguson et al. 2000a; Ferguson et al. 2000b) and confirmed in an experimental *ex vivo* loading study (Ferguson et al. 2003).

During the experimental work, Ferguson et al. (2003) measured the synovial fluid pressure *ex vivo* in the fossa of six intact hemipelvis hip specimens. The joint capsule was removed but the labrum was left intact and a pressure transducer was inserted into the fossa. The instrumented specimens were mounted on a materials testing machine in a temperature regulated fluid bath while a step load of 75% of donor bodyweight (BW) was applied. The results in Figure 2-7 show an abrupt increase in synovial fluid pressure followed by an exponential decay to a steady value near zero. After repeating the test without the labrum, the maximum synovial fluid pressure measured was nominally lower and the rate of decay faster. The overall joint consolidation was also higher without the labrum, implying increased cartilage stress and strain, however, no measure of the solid matrix stress was made (Ferguson et al. 2003). The resulting hypothesis is that due to the biphasic load transfer (Section 2.2), decreases in hydrostatic pressure should result in a corresponding increase in solid matrix stress (Ferguson et al. 2003).

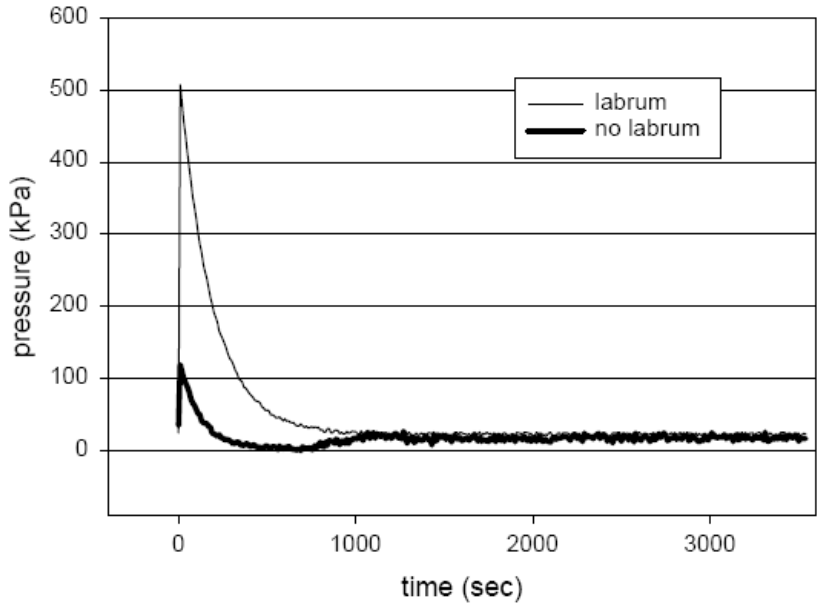


**Figure 2-7: Synovial fluid pressure measured in the fossa of an intact hip specimen before and after labral resection. Reproduced with permission from Ferguson et al. (2003).**

Ferguson et al. (2003) was a pioneering study in that the labrum of the specimens remained intact during the experiments. The joint was not disarticulated as in the earlier *ex vivo* contact studies summarized in Section 2.4. The experiments in this thesis have been modelled after the work of Ferguson et al. (2003).

## 2.6 Physiological Alignment During Specimen Potting

Correct physiological alignment of an *ex vivo* specimen is defined by two aspects: the relative orientation of the femur to the acetabulum of the pelvis and the absolute orientation of the acetabulum to the axis of experimental loading.

Relative orientations of several *ex vivo* studies are shown below in Table 2-4. The absolute orientation of the resultant force is also included. Where not specified or easily inferred from the studies, values were not included. The term vertical refers to the vector created by the intersection of the coronal and sagittal planes.

Bergmann et al. (1993) observed during an *in vivo* study using an instrumented femoral prosthesis, that the peak force during gait was recorded when the long axis of the femur was at 5º relative flexion. To achieve this angle with a specimen transected at the midpoint of the femur, the proximal femoral shaft must be aligned with an additional 8º (Bergmann et al. 1993) or 10º (von Eisenhart-Rothe et al. 1997) of flexion due to the anterior curve of the femur in the sagittal plane. Other authors have either stated or implied the use of 0º of relative flexion although citations for this rationale are often not included (Afoke et al. 1980; Afoke et al. 1984; Afoke et al. 1987; Adams & Swanson 1985; Bay et al. 1997; Konrath et al. 1998; Ferguson et al. 2003).

Adduction of the femoral shaft 9º relative to the acetabulum in the coronal plane has been repeatedly accepted as physiologically representative by multiple studies shown in Table 2-4. The assumption may have originated from the work of Pauwels (1935) as cited by Bergmann et al. (1993), or from Steindler (1955) as cited by Afoke et al. (1980).

Table 2-4 implies acceptance through repeated experimental configurations that 0º of relative internal rotation is representative of the stance phase of gait. Neutral internal rotation is achieved when the linea aspera of the femur is directly posterior (Konrath et al. 1998).

For normal walking, Bergmann et al. (2001) observed the average direction for the resultant force vector acting on the acetabulum to be 13º medial from vertical in the coronal plane. *Ex vivo* studies have commonly used resultant force directions of 13º (Greaves et al. 2009; Greaves et al. 2010) or 16º (Afoke et al. 1980; Afoke et al. 1984; Afoke et al. 1987; Ferguson et al. 2003) medial of vertical.

**Table 2-4: Comparison of Orientation for Specimen Potting Used for Single Leg Stance Phase of Gait in *Ex Vivo* Studies**

| Study | Relative Flexion (Sagittal Plane) | Relative Adduct. (Coronal Plane) | Relative Internal Rotation | Absolute Acetabular Resultant Force (medial of vertical) | Applied Load (% BW) | Original Source for Alignment |
|---|---|---|---|---|---|---|
| (Afoke et al. 1980)<br>(Afoke et al. 1984)<br>(Afoke et al. 1987) | 0º | 9º | **0º** | 16º | 1.3 | (Steindler 1955)<br>(Bombelli 1976) |
| (Adams & Swanson 1985) | 0º | n/a | **0º** | 18.8º | 1.62 | (Paul 1976) |
| (Bay et al. 1997) | 0º | 15º | **0º** | 33.5º | 1.00 | n/a |
| (von Eisenhart-Rothe et al. 1997) | 15º* | 8º | **0º** | n/a | 0.5 - 3.00 | (Bergmann et al. 1993) |
| (von Eisenhart et al. 1999) | 5º | 11º | n/a | n/a | 3.45 | (Witte et al. 1997) |
| (Konrath et al. 1998) | 0º | 15º | 5 - 10º | 25º | 1.00 | (McLeish & Charnley 1970) |
| (Ferguson et al. 2003) | 0º | 9º | **0º** | 16º | 0.75 | n/a |
| (Greaves et al. 2009)<br>(Greaves et al. 2010) | 13º | 5º | **0º** | 13º | 2.3 | (Bergmann et al. 1993)<br>(Bergmann et al. 2001) |
| | **13º**** | | | | | (Backman 1957)<br>(Bergmann et al. 1993) |
| | | **9º** | | | | (Pauwels 1935)<br>(Steindler 1955)<br>(Afoke et al. 1980)<br>(Bergmann et al. 1993) |
| | | | | **13º** | 2.38 | (Bergmann et al. 2001) |
| Values most strongly cited | **13º** | **9º** | **0º** | **13º** | 2.38 | |
| | | | | | | |
| | * Proximal femur must be mounted at 15º flexion to simulate 5º flexion of long femoral axis due to assumption of 10º anterior curve of femur in sagittal plane | | | | | |
| | ** Similar to (*), simulation of the of 5º flexion of the long femoral axis, requires the proximal end of the femur to by mounted at additional 8º flexion due to anterior curve. This differs from (*) in that correction provided by (Bergmann et al. 1993) is 8º whereas (von Eisenhart-Rothe et al. 1997) has approximated this number as 10º. | | | | | |

As explained previously, the positions of 13º flexion, 9º adduction, and neutral internal rotation are defined for the femur relative to the acetabulum during the stance phase of gait. The absolute position of the acetabulum is described by observations that, during standing, the Anterior Superior Iliac Spine (ASIS) and Pubic Tubercle (PT) are found to be aligned vertically when viewed from the sagittal plane, and the right and left ASIS are aligned horizontally in the coronal plane (Bay et al. 1997; Konrath et al. 1998; Greaves et al. 2009).

In previous *ex vivo* studies, two types of hip specimens have been tested using a material testing machine. Full pelvis specimens (Figure 2-8-a) are intended to provide a realistic representation of physiological loading and have been used in a limited number of studies (Bay et al. 1997; Widmer et al. 1997; Konrath et al. 1998). The more common approach is to use a hemipelvis specimen (Figure 2-8-c) and perform an alignment correction of angle, θ (Figure 2-8-b), to ensure approximate physiological loading (Day et al. 1975; Brown et al. 1978; Afoke et al. 1980; Mizrahi et al. 1981; Brown & Shaw 1983; Afoke et al. 1984; Adams & Swanson 1985; Afoke et al. 1987; von Eisenhart-Rothe et al. 1997; von Eisenhart et al. 1999; Ferguson et al. 2003). Hemipelvis specimens are more economical than full pelvis specimens.

In the full pelvis specimen, the direction, θ, of the resultant force vector, J, is defined by the summation of the applied force vector, W, and abductor simulation force vector, A (Figure 2-8-b). Zero net moment exists about the joint centre. In the case of a hemipelvis specimen, as A is non-existent, the effective direction of the resultant force vector, J, aligns with the vertical applied load axis of the material testing machine. The reaction force vector, W, is now equal in magnitude and shares a line of action with the resultant force, J, to avoid creation of a moment about the hip joint centre (Figure 2-8-c).

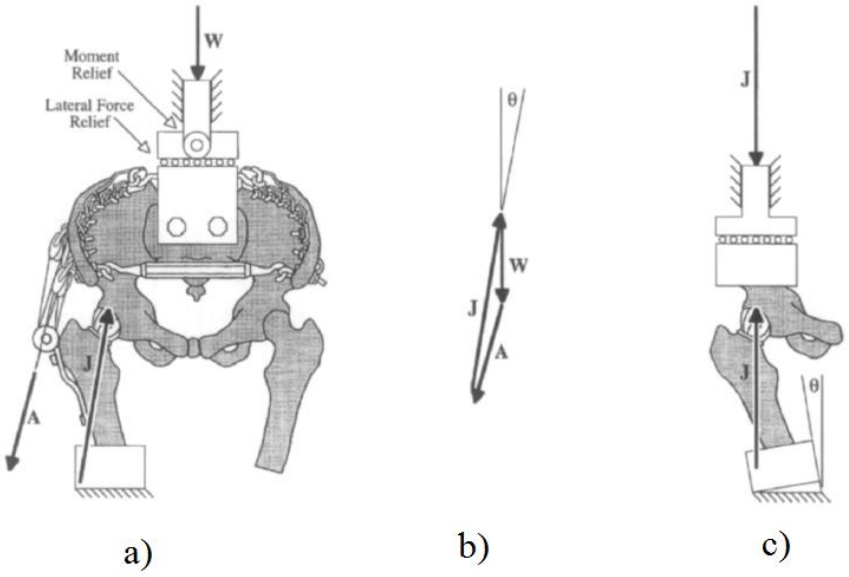


**Figure 2-8: (a) Forces acting on a full pelvis specimen; (b) angle, θ, of resultant force resolved using vectors; (c) hemipelvis potted with correction θ to maintain resultant force direction through joint. Reproduced with permission from Bay et al. (1997)**

A suitable angular correction, θ, is 13º medial of vertical as measured *in vivo* by Bergmann et al. (2001). Using this correction, the ultimate orientation for potting the iliac crest of a hemipelvis specimen is with the ASIS and PT vertical in the sagittal plane and the PT rotated 13º medially about the joint centre in the coronal plane. The complementary position of the proximal femoral shaft is then at 13º flexion and neutral rotation. In the coronal plane, the position of the proximal femur is 22º medial of vertical (9º relative adduction to the acetabulum) from the vertical axis of the material testing machine. This position describes simulation on a material testing machine of the stance phase of gait where the peak force for normal walking of 2.38 x BW was measured by Bergmann et al. (2001) during *in vivo* experiments.

# Chapter 3: Experimental Setup and Methodology

This chapter explains the steps involved in completing the experimental work for this thesis. This chapter begins with the calibration procedure for the sensors that will be used in the subsequent *ex vivo* measurements. The contact stress and hydrostatic pressure sensors are calibrated for their intended purpose before a second calibration to determine sensitivity to thermal drift is performed. The experimental method continues with the preparation and potting of the specimens and insertion of the calibrated sensors into the articular cartilage and fossa of the joint. The position of the sensors is then quantified using a radiographic approach. After instrumentation of the specimen is complete, it is transported to a materials testing machine. The setup of the materials testing machine and subsequent application of representative physiological loading are intended to closely follow the methods of Ferguson et al. (2003) as discussed in Section 2.5. An explanation of the parameters for data collection is included before a summary of the four day testing protocol. The initial three days of testing are intended to establish repeatability of the measurement technique before a change is introduced by resecting the labrum on the final day. The chapter concludes with an explanation of how labral resection was performed.

## 3.1 Contact Stress Sensor Calibration

Dennison et al (2010) confirmed that the response of contact stress sensors constructed according to the schematic in Figure 2-6 is relatively independent of the modulus of the contacting material. Calibrations performed between steel gauge blocks (Class 0, 24.1 mm x 24.1 mm, steel, Mitutoyo Can., Toronto, ON) and Viton® rubber differed by only 9.5% (Dennison et al. 2010). For the current experiment, multiple contact stress sensors were fabricated similar to the schematic in Figure 2-6 with the only deviations being a

reduction of the Polyimide™ sheath length to 10 mm and a 1 mm FBG from a different supplier (FWHM BW < 1.5 nm, reflectivity > 50%, Polyimide™ fiber, Technica SA, China).

Calibration of the contact stress sensors was completed individually using the setup in Figure 3-1 and Figure 3-2. To maximize repeatability and consistency, calibrations were performed between steel gauge blocks without Viton® rubber.

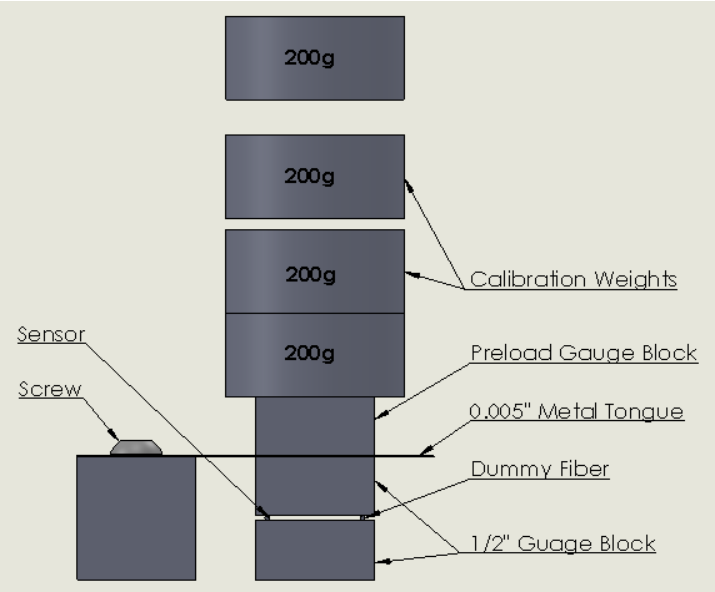


**Figure 3-1: Side view of contact stress sensor calibration setup**

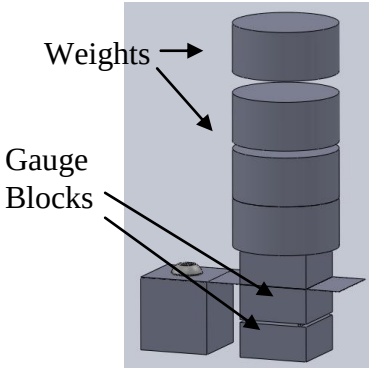


**Figure 3-2: Contact stress sensor calibration setup**

The sensor and dummy fiber of equivalent diameter function as simple supports between the two gauge blocks. A thin 0.005" spring steel tongue rests on top of the second gauge block to isolate traction forces that arise when stacking calibration weights. A third gauge block placed on top of the tongue acts as a preload to keep the tongue seated. Once the preload is applied, the sensor is considered zeroed.

Calibration data points were collected by manually clicking a button in a custom LabView™ program (32 bit Version 10.0.1 SP1, National Instruments Inc., Austin, TX), to automatically record sensor wavelengths without transcription errors. The program records data from a 4 channel 1550 nm band FBG optical interrogator (PXIe-4844, National Instruments Inc., Austin, TX) at 10 Hz and analog inputs from a 16-bit analog data acquisition card (PXIe-6341, National Instruments Inc., Austin, TX) at 1000 Hz. Both cards are mounted in a 9-slot PXIe chassis (PXIe-1078, National Instruments Inc., Austin, TX) with an integrated computer controller (PXIe-8133, Intel® Core i7-820QM, 4 GB RAM, National Instruments Inc., Austin, TX).

After taking an initial zero point, individual 200g calibration weights (Model 80850147, ASTM Class 6, OHAUS Corp., NJ) were stacked concentrically on top of the centre of the gauge blocks to a maximum of 2 kg. The calibration mass is distributed evenly over the two simple supports, the sensor and dummy fiber, creating a uniform linear load profile of 0 to 0.98 N/mm as the mass varies from 0 to 2 kg.

A calibration data point was taken 5 seconds after each change in weight to avoid time dependent viscoelastic effects of the silicon annulus (Ngoi et al. 2004). Data points were collected as each weight was removed to calculate hysteresis. This procedure was repeated for each sensor at angular positions of $0^{o}$, $60^{o}$, and $120^{o}$ to account for

imperfections in concentricity during fabrication. For sensor V-M each angular position was repeated three times.

Calibrations for one sensor, V-M, were also repeated after soaking the sensor in phosphate buffered saline (PBS) solution (pH 7.4) for one hour until the sensor response reached a steady state. The sheath was kept moist during the re-calibration. For the wet re-calibration, two trials at each of the three angular positions were performed.

For each contact stress sensor, the individual sensitivities in $pm \cdot (N \cdot mm^{-1})^{-1}$ for the angular orientation are calculated as the slope of a linear fit between the sensor wavelength response and the applied uniform distributed load. The overall mean regression calculated sensitivity for the sensor is computed as the average of the sensitivities for all angular positions. Sensitivities are converted from $pm \cdot (N \cdot mm^{-1})^{-1}$ to pm/MPa by multiplying by the sensing area. The sensing area is calculated as the product of the sensor diameter, 0.24 mm, and FBG gauge length, 1 mm.

### 3.2 Hydrostatic Pressure Sensor Calibration

The hydrostatic pressure sensor was prepared in accordance with the schematic in Figure 3-3 with the only deviation being the use of a 1mm FBG (FWHM BW < 1.5 nm, reflectivity > 50%, Polyimide™ fiber, Technica SA, China). To remain consistent with previous experiments (Dennison et al. 2008a; Dennison et al. 2008b; Dennison et al. 2008c; Dennison & Wild 2008b) the hydrostatic pressure calibration apparatus shown in Figure 3-3 was used to calibrate the sensors over a pressure range of 0 to 1 MPa in 0.1 MPa increments. The calibration was repeated three times.

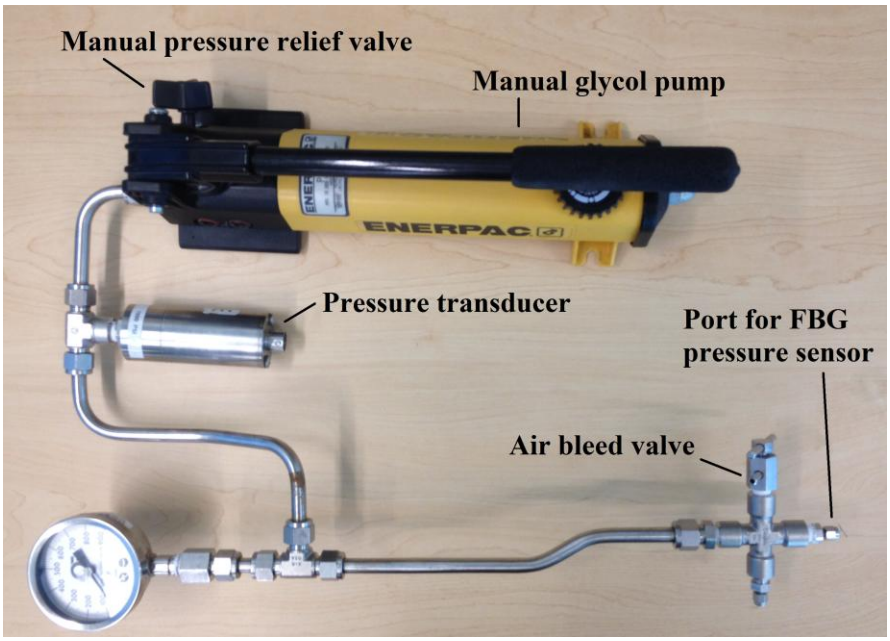


**Figure 3-3: Hydrostatic pressure calibration setup**

After bleeding the air from the glycol hydraulic system, a manual pump with relief valve (ENERPAC P141, Milwaukee, WI) was used to vary the fluid pressure. The pressure transducer (OMEGA PX300-2KGV, accuracy ±34 KPa, Stamford, CT) analog output and FBG wavelength response were recorded using the same equipment and LabView™ program as in Section 3.1.

## 3.3 Temperature Calibration of Both Sensor Types

Sensitivity to temperature was assessed for both transverse contact force and hydrostatic pressure sensors using an environmental chamber (Figure 3-4). In both cases the sensors were attached to a suitable thermal mass whose temperature was monitored with a resistive temperature device (RTD) (0-100ºC, ±0.015ºC at 0ºC, PR-11-2-100-1/16-6-E, Omega, Stamford, CT) and RTD signal conditioner (accuracy <0.2% FS, linearity <0.1% FS, DRF-RTD-115VAC-0/100C-0/10, Omega, Stamford, CT). Calibration data was collected using a ramped temperature profile. A gradient of 5ºC above the response

of the RTD was maintained manually in the environmental chamber as temperature increased before the thermal mass was permitted to air cool with the chamber door open. Analog temperature output and FBG wavelength response were recorded using the same custom LabView™ program as in Section 3.1.

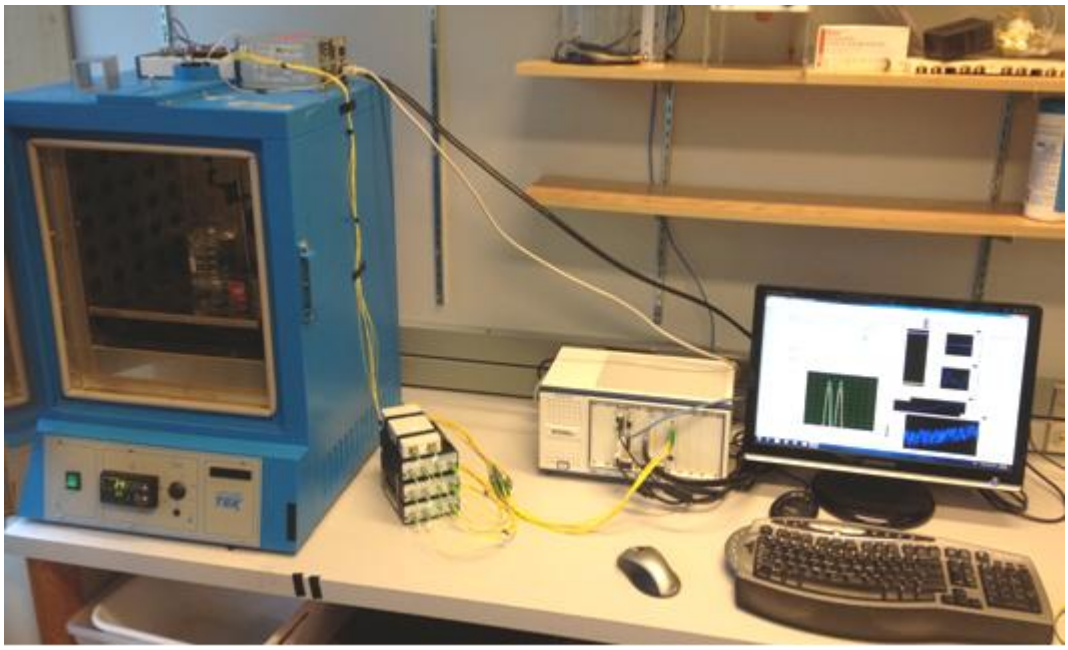

**Figure 3-4 : Environmental chamber with sensors located inside for temperature calibration**

The transverse contact stress sensors were bundled to the RTD (Figure 3-5) and suspended in a water bath within the environmental chamber. Calibration data was collected in 1ºC increments for a range of 10ºC during heating and cooling.

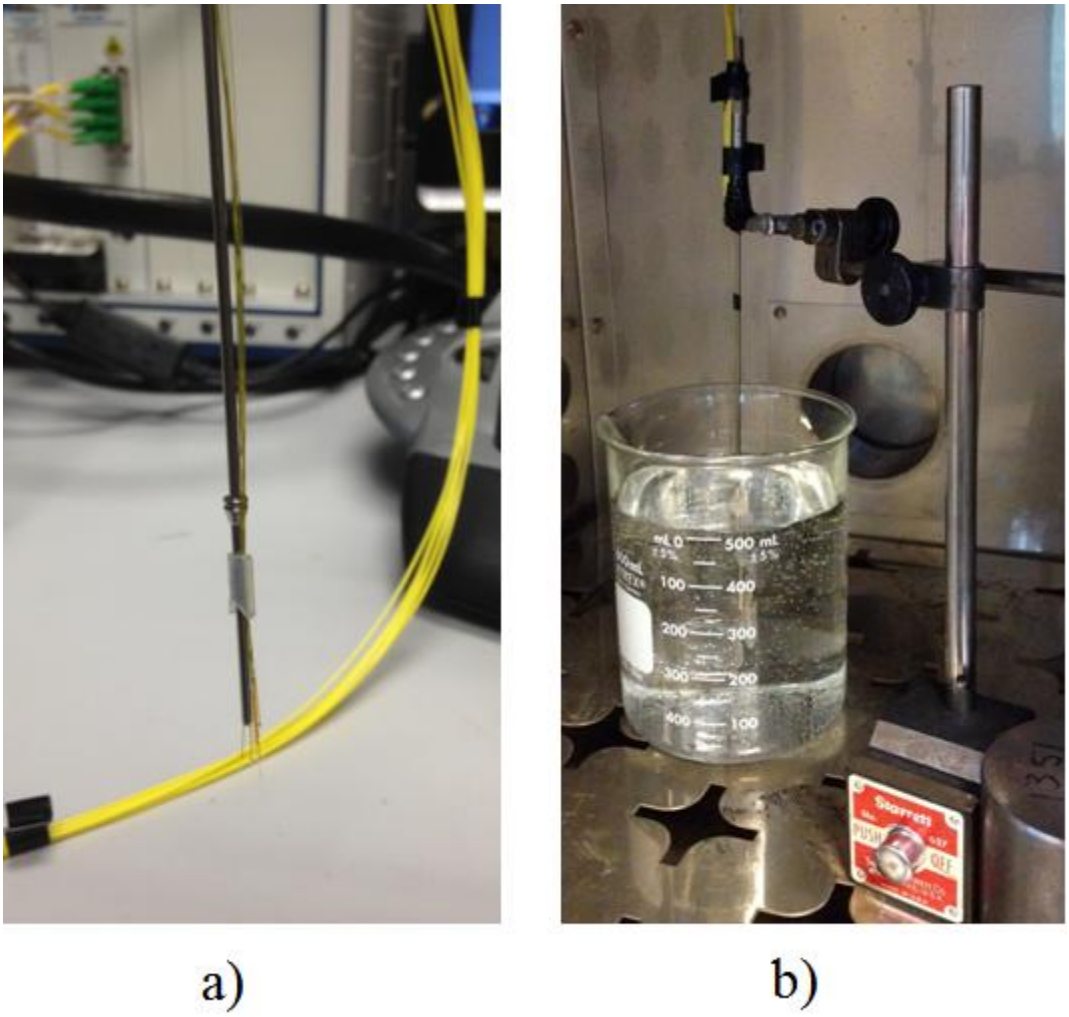


**Figure 3-5: (a) Contact stress sensors bundled to RTD temperature probe; (b) beaker of water inside environmental chamber with RTD probe and sensors at mid-depth**

The hydrostatic pressure sensors were also calibrated in batch fashion within the environmental chamber. A one inch thick aluminum plate was used as a thermal mass as shown in Figure 3-6. The sensors and RTD were temporarily fixed to the plate using a small amount of UV cure epoxy near the sensor tips and electrical tape. A plastic cover was placed over the sensors to create a dead space and reduce the effects of convection within the environmental chamber. Similar to the contact stress sensors, calibration data was collected in 1ºC increments for a range of 10ºC during heating and cooling.

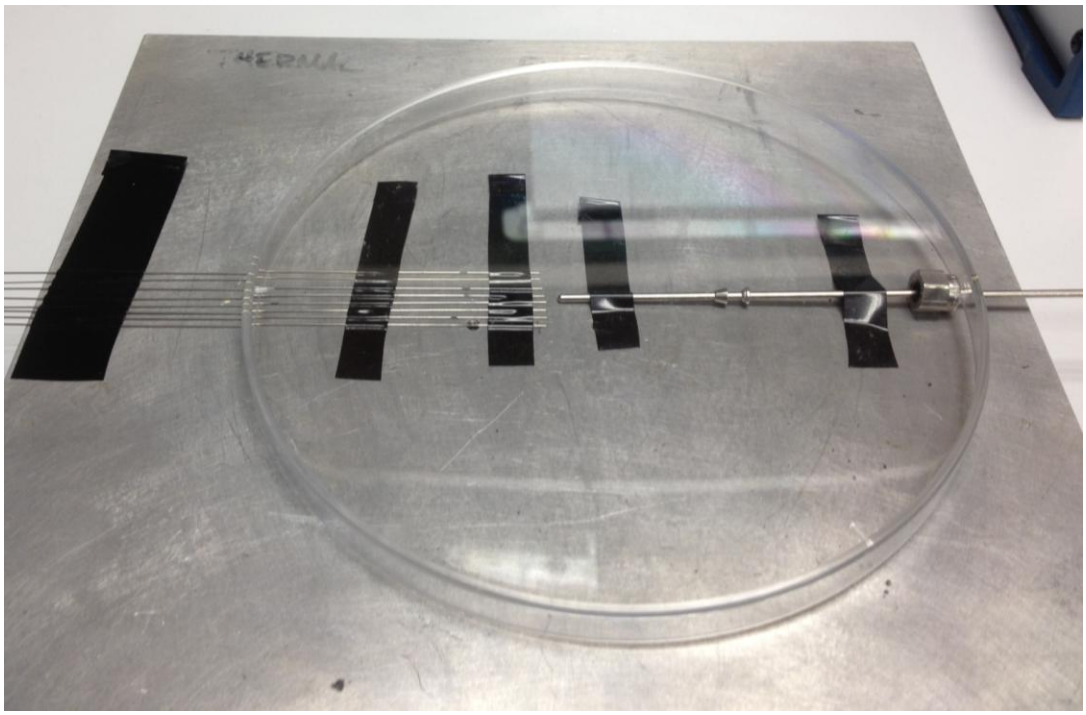

**Figure 3-6: Hydrostatic pressure sensors (left) and RTD probe (right) attached to thermal mass**

## 3.4 Specimen Preparation and Potting

Three fresh hemipelvis hip specimens were obtained by the Centre for Hip Health and Mobility (CHHM) which is a University of British Columbia Senate-approved organization affiliated with the Vancouver Coastal Health Authority. The donors had no documented medical history pertaining to the hip. Each specimen was harvested within 24 hours post-mortem and stored at -20 ºC. Table 3-1includes the donor information.

**Table 3-1: Donor Information**

| | Life Legacy ID number | CHHM Number | Sex | Age | Side | Donor Body Weight |
|---|---|---|---|---|---|---|
| Specimen 1 | 10-09022 | H1340 | M | 60 | Left | 75.3 kg (709 N) |
| Specimen 2 | 10-07001 | H1333 | M | 78 | Left | 88.9 kg (872 N) |
| Specimen 3 | 10-09059 | H1341 | M | 64 | Right | 114 kg (1117 N) |

Prior to potting, each specimen was thawed and all soft tissue was removed except the joint capsule. Following dissection, each specimen was inverted, attached to a fixture with three adjustable rotational degrees of freedom (Figure 3-7) and aligned in the potting container for fixation with PMMA.

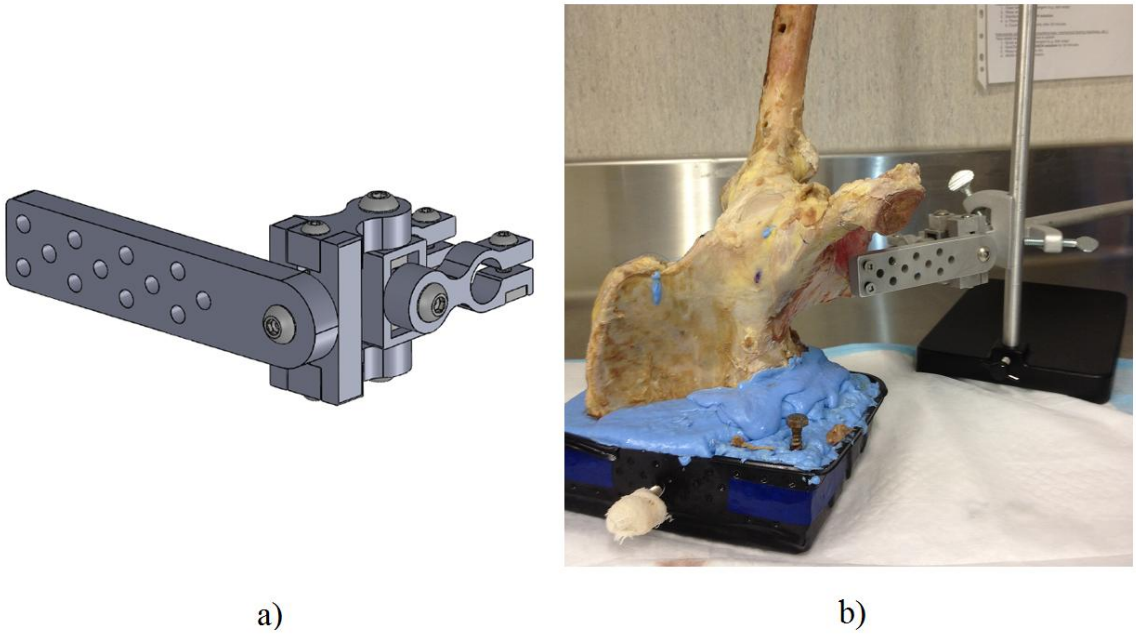

a) b)

**Figure 3-7: (a) Adjustable alignment fixture for specimen potting (b) attached to laboratory stand and specimen while the blue PMMA hardens**

A protocol was developed to align the hemipelvis in the correct absolute position and fixate it with polymethyl-methacrylate (PMMA) cement (Fastray 0921386, Harry J. Bosworth® Co., Skokie, IL). The detailed alignment and potting procedure is explained in Appendix A. As explained in Section 2.6, the pubic tubercle (PT) of the pelvis was rotated 13º of medial about the joint centre, from normal alignment when standing, while maintaining correct alignment of the pelvis in the sagittal plane.

The femoral shaft does not need to be potted, as an adjustable fixture (Figure 3-21) has been developed to attach the femur to the load cell of the material testing machine (Section 3.7).

### 3.5 Sensor Insertion

The two types of FBG sensors used to instrument the specimens are contact stress sensors (V-series) and a hydrostatic pressure sensor (PDB-series). After preparing the specimen, as explained in Section 3.4, both types were inserted using hypodermic needles, starting with the contact stress sensors. The contact stress sensors were implanted within the middle zone (Figure 2-1) of the acetabular cartilage by puncturing and passing through the labrum (Figure 3-8). The hydrostatic pressure sensor was inserted into the fossa by puncturing the soft tissue in the inferior-medial region of the joint.

Three contact sensors (V-I, V-K and V-L) were used in all specimens (Figure 3-8) and three additional sensors (V-M, V-P, and V-R) were used only on Specimen 3 (Figure 3-9).

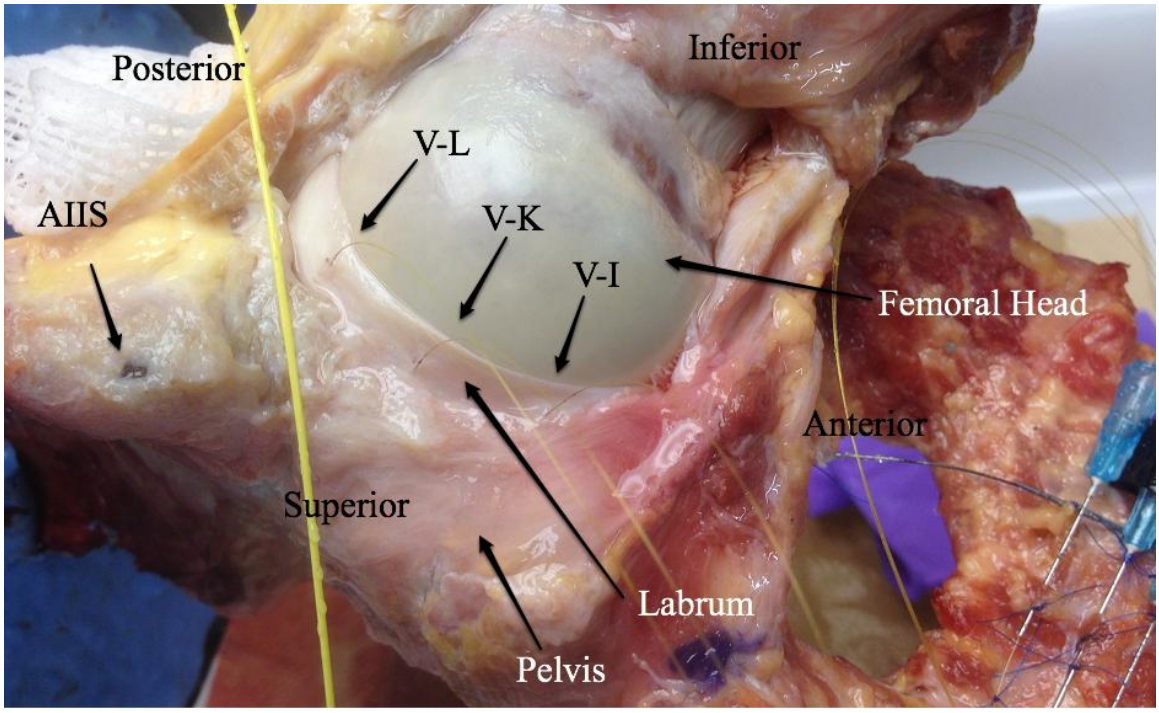


**Figure 3-8: Three contact stress sensors inserted through the labrum in Specimen 2**

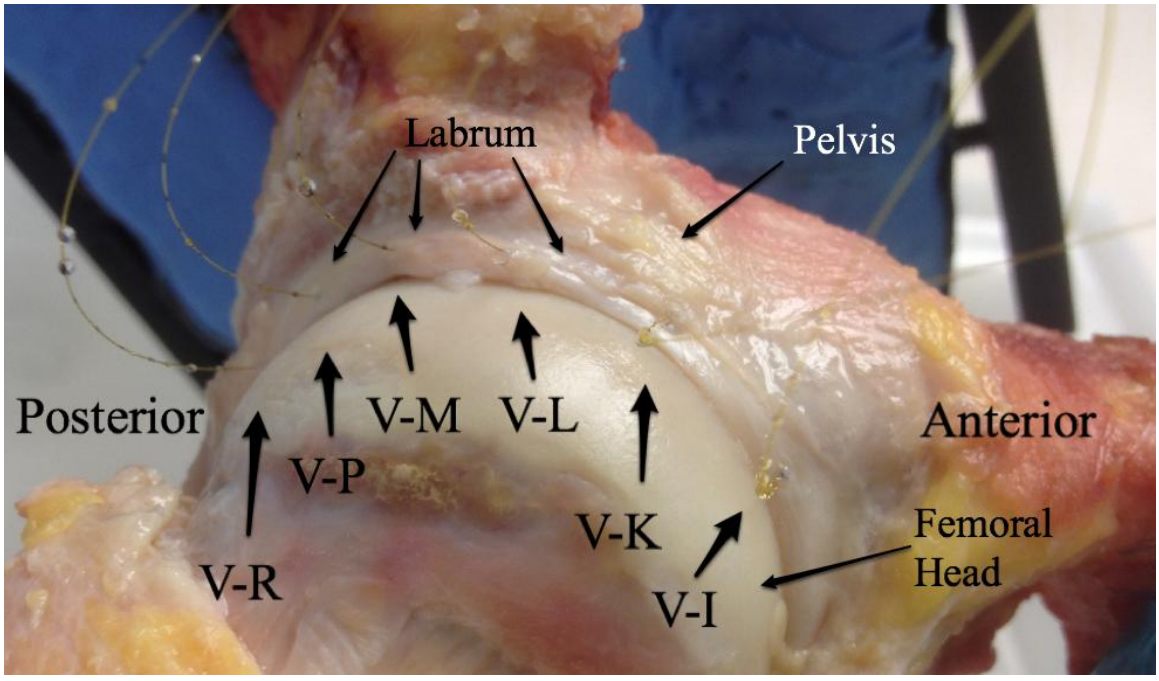


**Figure 3-9: Six contact stress sensors inserted into Specimen 3.**

The contact stress sensors were inserted in alphabetical order with the lowest alpha character always in the most anterior location. The alpha symbol increases as placement becomes more posterior (Figure 3-10) and the position of each sensor is quantified using the procedure in Section 3.6. The hydrostatic pressure sensor was always inserted within the fossa.

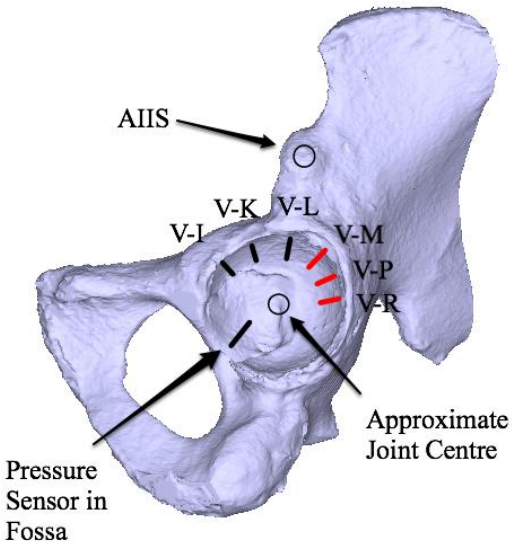


**Figure 3-10: Radial Position of sensors on 3-D model of pelvis**

The surgical research suite (Figure 3-11) at the CHHM was used for the insertion of all sensors. A hip distracter apparatus was used to secure a specimen in position for radiographic imaging with a fluoroscopy C-arm (Arcadis Orbic ISO-C; Siemens AG, Munich, Germany).

To insert each contact sensor into the cartilage, a 25 gauge, one inch long hypodermic needle (Precision Glide 305125, BD Co., Franklin Lakes, NJ) was used as a cannula with a 0.010" steel wire (B000P0NVU6, Amazonsupply.com), used as a trochar to keep the needle bore clear (Figure 3-12).

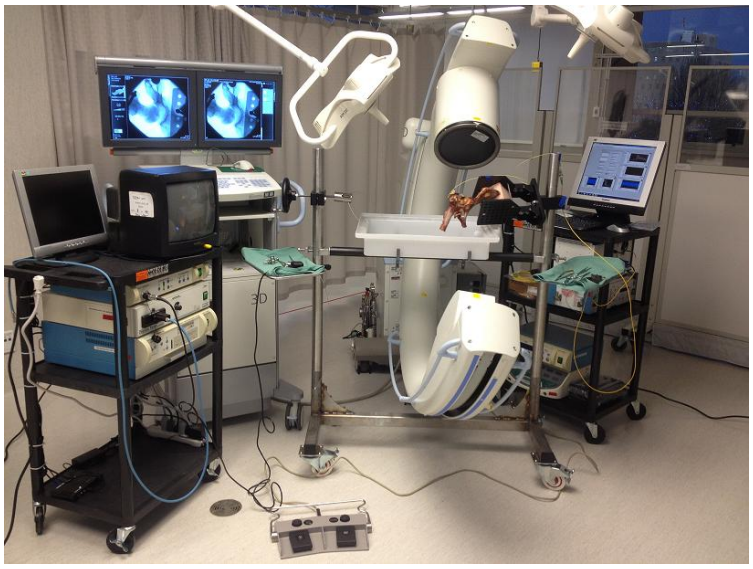

**Figure 3-11: Surgical suite at CHHM showing a hip specimen secured in place on the hip distraction apparatus within the field imaging of the C-arm.**

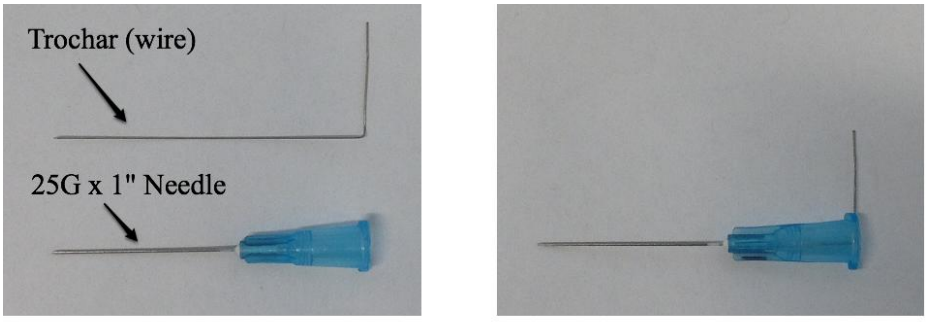


**Figure 3-12: (a) 25G x 1" needle and 0.010" wire trochar individually and (b) assembled.**

The labrum was exposed for insertion of the contact stress sensors by creating a 30 mm x 30 mm window in the anterior joint capsule (Figure 3-13). For Specimen 3, the window was extended an additional 30 mm in the posterior direction. The puncture site for the first needle inserted into the labrum (V-L) was located along the line connecting the AIIS and joint centre. Use of the AIIS as a reference point is explained in Section 3.6.

The puncture sites of the needles anterior of the AIIS, were located at 13 mm and 26 mm along the labrum from the line connecting the AIIS and joint centre. Using an average femoral head size of 50 mm (Rushfeldt et al. 1981) and an additional 5 mm thickness for the labrum, the resulting radius from the joint centre to the exterior surface of the labrum is 30 mm. For target angular positions of 25º ad 50º anterior of the AIIS, this corresponds to arc lengths of 13 mm and 26 mm along the labrum.

Due to a limited practical window size in the joint capsule, the needles located posterior of the AIIS in Specimen 3 were inserted at 10, 20, and 30 mm posterior of the reference line, targeting angular positions of 20º, 40º, and 60º.

The trajectories of all needles aimed to converge at the approximate joint centre. For Specimen 3, where six needles were used, they were inserted as two batches of three.

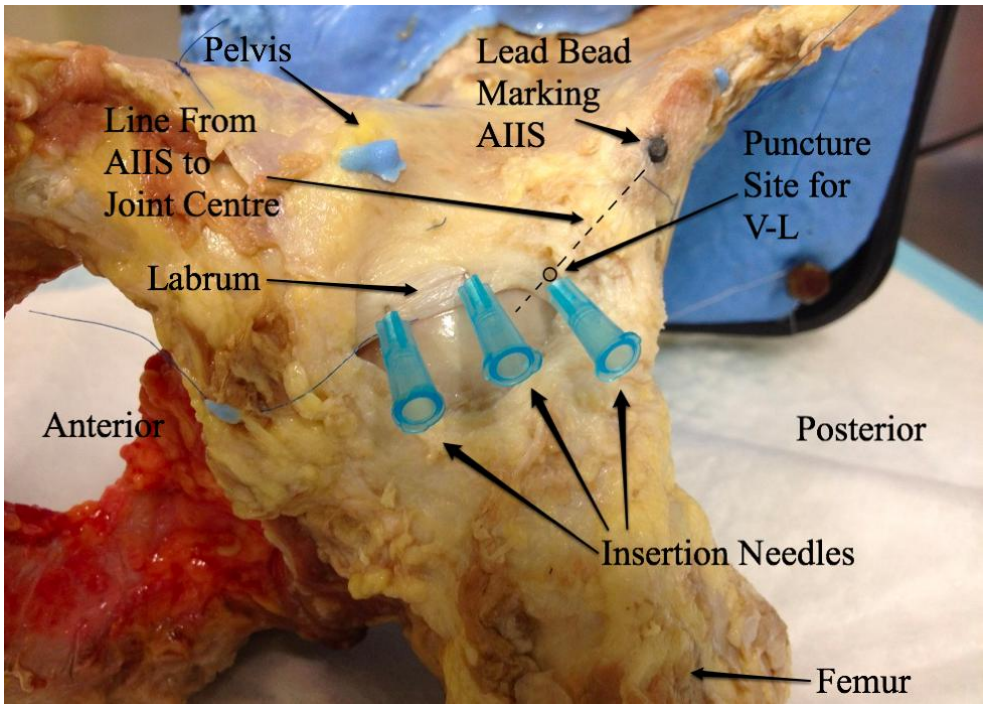


**Figure 3-13: Window in anterior joint capsule used to insert three needles through labrum into acetabular cartilage of Specimen 2**

For each contact stress sensor insertion needle, the labrum was punctured at mid height, with the trochar wire inside the needle. The needle tip abruptly contacts the osseous perimeter of the acetabulum. At this point, changing the angle of attack of the needle, guided by radiographic images from the fluoroscopy C-arm, allows the needle tip to be positioned inside the rim of the acetabulum (Figure 3-14-a).

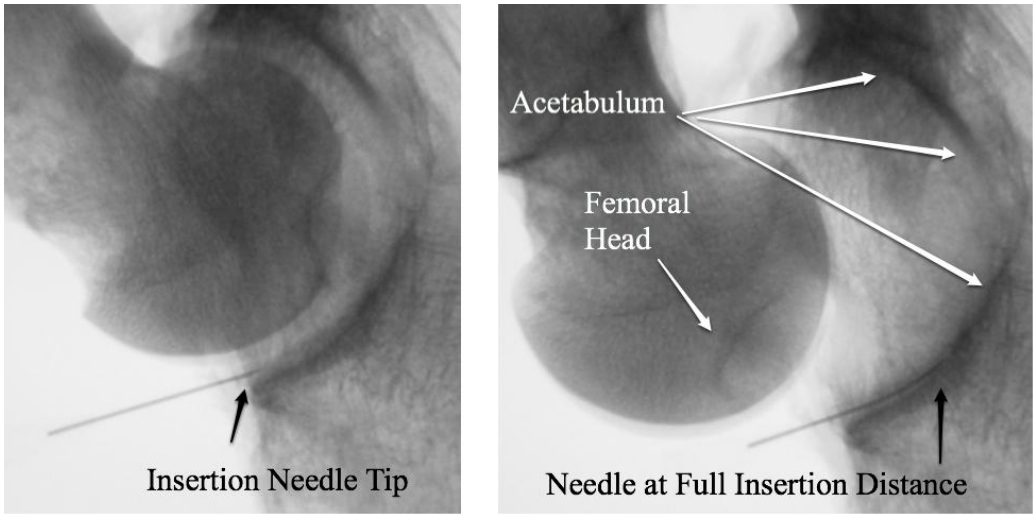


**Figure 3-14: Radiographs of needle for sensor insertion in acetabular cartilage with (a) needle tip inside rim of acetabulum and (b) inserted to full depth 15 mm.**

Once the tip of the needle is located on the interior edge of the acetabular rim, the orientation of the chisel tip of the hypodermic needle guides the path of the needle through the cartilage. By rotating the orientations of the chisel tip (Figure 3-15), the needle can be advanced by feel. First, the "digging" action is used to bury the needle tip deep into the cartilage. Then by rotating the needle 180$^{o}$, the "bouncing" action can be used to advance the needle 1-2 mm within the cartilage before switching back to the

digging action to ensure the needle tip remains below the cartilage surface. This iterative procedure is repeated until the needle has reached the full depth of 15 mm relative to the puncture in the surface of the labrum (Figure 3-14-b). Ultimately, the sensor sheath will occupy the distal 10 mm of the needle with the FBG sensing area located 5 mm from the tip of the needle.

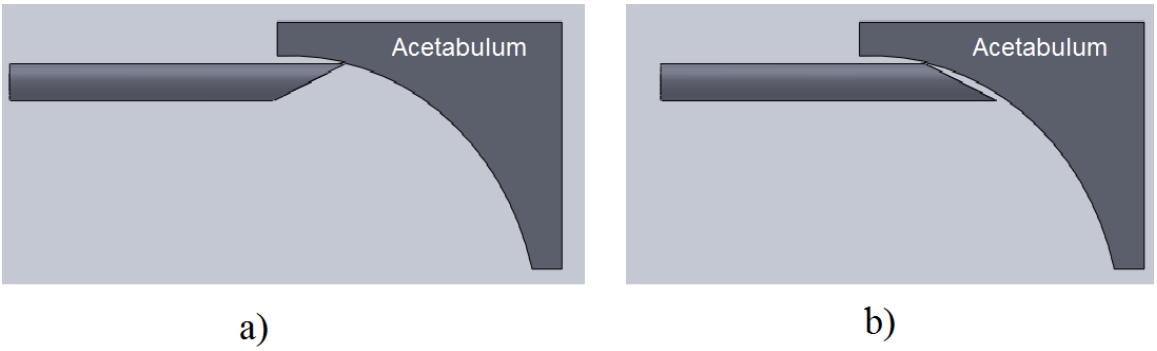


**Figure 3-15: Insertion needle contacting bone/cartilage interface showing (a) digging action and (b) bouncing action (needle not to scale).**

After all of the needles have been inserted and their positions quantified using the procedure in Section 3.6, the wire trochars are removed from the needle bores. A mark is placed 15 mm from the distal end of the each contact stress sensor before being inserted into the appropriate needles. Axial force is applied to the optical fiber as the needle is fully withdrawn along the fiber. The mark on the sensor is used to visually confirm that the sensor remains implanted at the correct depth of 15 mm from the labral puncture after the needle has been removed.

Once inserted within the acetabular cartilage, the sensors on all specimens were strain-relieved using sutures (5-0 Prolene™ 8720, Ethicon™ Inc., Somerville, NJ) to secure the insertion needles, and a loop of fiber to the ischium of the pelvis (Figure 3-16).

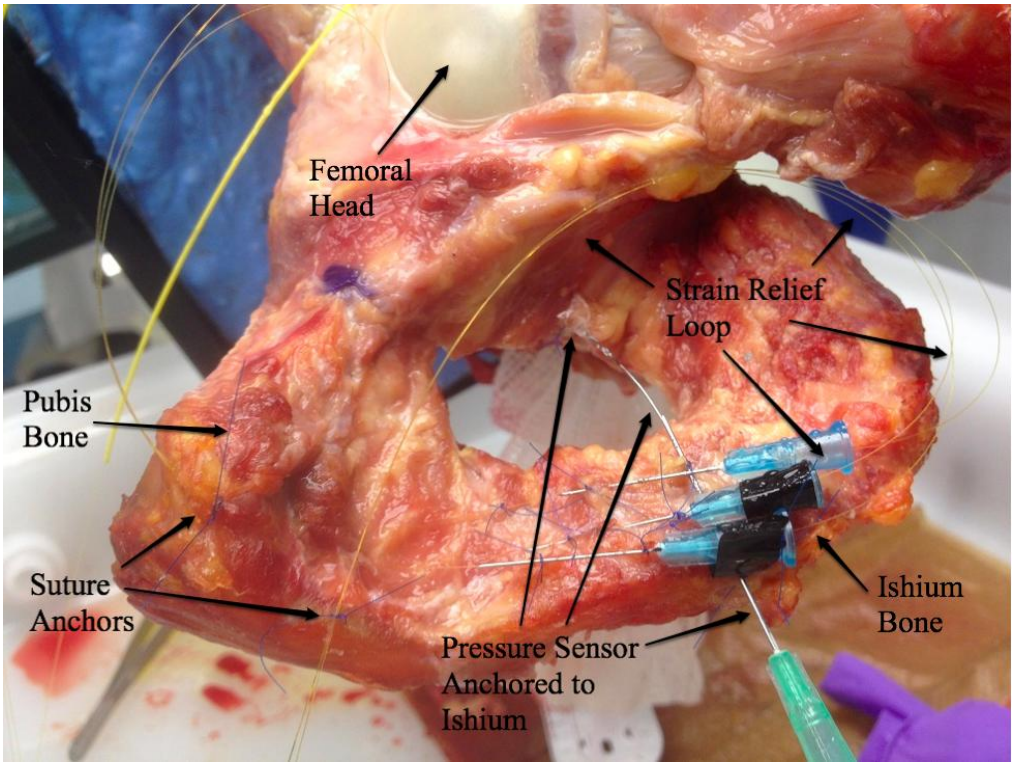


**Figure 3-16: Strain relief loop and three blue contact stress sensor insertion needles secured with sutures. Pressure sensor entering the fossa and green insertion needle are visible.**

Friction and cartilage swelling were the sole means of fixation of the sensors within the cartilage for Specimens 1 and 2. In an attempt to improve sensor fixation in Specimen 3, a small amount of cyanoacrylate adhesive (Loctite® 401, Henkel Corp. Westlake, OH) was applied to each sensor fiber at the site where it pierced the labrum before strain relieving the fibers in a manner consistent with the other specimens.

After the contact stress sensors were inserted and strain relieved, the hydrostatic pressure sensor was inserted to a depth of 25 mm within the fossa (Figure 3-16). Using a 21 gauge, 1.5" long hypodermic needle (Precision Glide 305167, BD Co., Franklin

Lakes, NJ) the pressure sensor was positioned in the fossa under radiographic guidance (Figure 3-17).

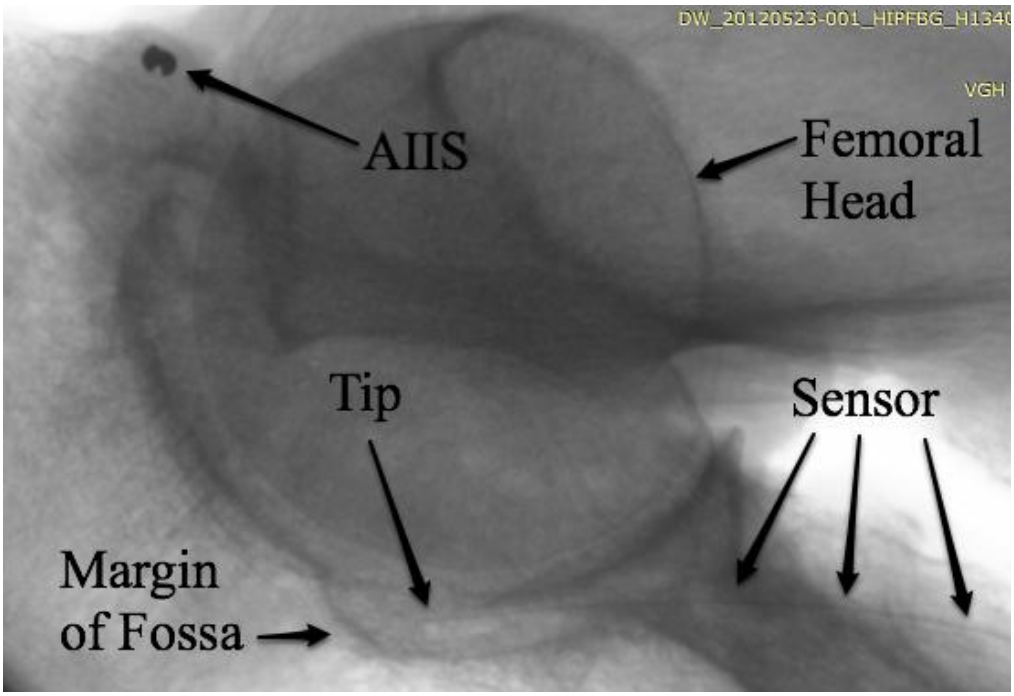


**Figure 3-17: Hydrostatic pressure sensor (faint line travelling horizontally at bottom) within the outline of fossa of Specimen 1 (H1340)**

The pressure sensors insertion needle was secured to the ishium using sutures and cyanoacrylate (Figure 3-16). A purse-string suture was tied around the sensor at the site where it enters the soft tissue of the fossa and then covered with cyanoacrylate adhesive to ensure a good seal. Strain relief was provided by adding cyanoacrylate to the tip of the sensor housing where it entered the tip of the needle, as the needle was well fixated to the ishium. As a final step, the hydrostatic pressure sensor position was quantified using the procedure in Section 3.6.

### 3.6 Radiographic Technique for Quantifying Sensor Location

The locations of the contact stress sensor insertion needles and the hydrostatic pressure sensor were quantified by using an adaptation of a novel radio-stereometric analysis (RSA) technique developed by Amiri et al (2011; 2012) at CHHM.

The contact stress sensors contain no radio-opaque material and therefore cannot be identified on radiographs. In order to quantify the radial position of the sensors, the position of the metallic insertion needles relative to the anatomy was used. Care was taken to ensure that the contact stress sensors remained in the original position of the insertion needles as the needles were withdrawn (Section 3.5). The hydrostatic sensor was housed with a stainless steel tube and could be imaged in its final position once the insertion needle had been withdrawn (Figure 3-17).

After inserting a batch of needles or the hydrostatic pressure sensor in the desired locations within the specimen, RSA or biplanar radiographic images of the joint were taken with the C-arm (Figure 3-18). An optoelectronic tracking system (Optotrak Certus; NDI, Waterloo, Canada) was used to record the orientation of the C-arm for each radiograph using three infrared emitting diode arrays attached to specific areas of the C-arm (Amiri et al. 2011). The diode arrays on the C-arm are registered, using the Optotrack, to form the basis of a calibrated coordinate system during initial experimental setup (Amiri et al. 2011).

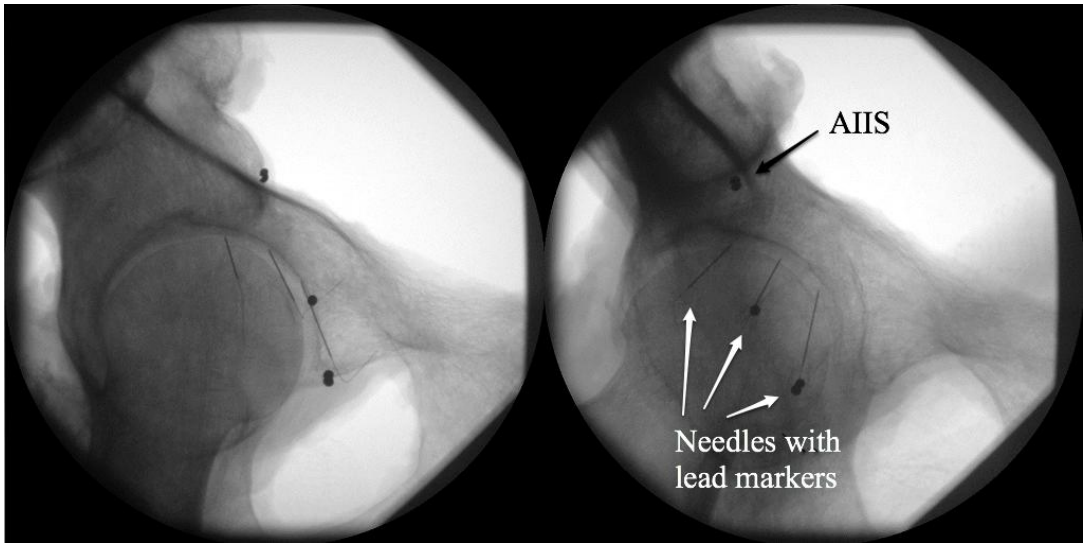


**Figure 3-18: Sample biplanar radiographic images taken at planes 25º apart for Specimen 1. Lead beads are used to identify the AIIS and the insertion needles.**

Using custom experimental software (Amiri et al. 2011), the biplanar radiographs were calibrated with the corresponding Optotrack data. The calibrated images were then loaded to a graphical user interface where the osseous landmarks of the pelvis and the insertion needles or pressure sensor were registered into the previously constructed calibrated coordinate system (Amiri et al. 2012). The anatomical landmarks were registered using a single point for the AIIS and a best fit sphere for the acetabulum. The insertion needles or hydrostatic sensor were registered by fitting splines along the visible lengths. All but the distal 10 mm of the splines, the region of the needle containing the sheath of the contact stress sensors or sensing tip of the pressure sensor, was then truncated.

A 3-D mesh model of the pelvic osseous anatomy was constructed from computer tomography (CT) scans taken of the specimens prior to sensor insertion. The 3-D model of the anatomy was registered into the calibrated coordinate system using the JointTrack

Bi-planar (SourceForge 2011), an open source software program provided by the University of Florida.

Once the needles or hydrostatic sensor, anatomical landmarks, and 3-D model are registered in a common coordinate system, calculation of relative positions is possible (Amiri et al. 2011; Amiri et al. 2012). The spherical approximation of the acetabulum is used to define a radial coordinate system for sensor location. The line from the spherical joint centre to the AIIS is defined as 0º with positive angular position specified in the anterior direction. The radial position, θ, of each insertion needle or the hydrostatic pressure sensor can be calculated relative to this 0º reference point (Figure 3-19).

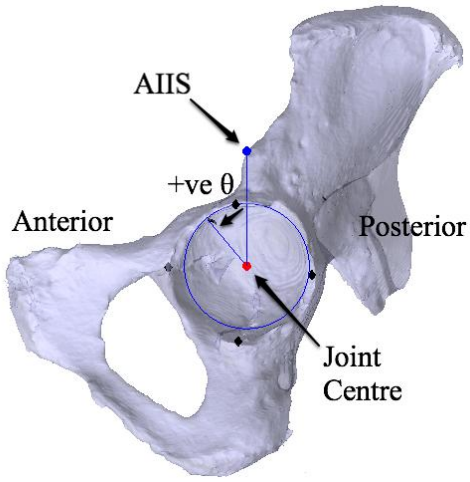


**Figure 3-19: Example of radial position angle, θ, relative to the line connecting the AIIS and joint centre. The angle is positive in the anterior direction.**

The target radial positions of the first three sensors are 0º, +25 º and +50º, and the target positions for sensors inserted posterior of the AIIS are -20º, -40º and -60º, as explained in Section 3.5.

### 3.7 Material Testing Machine Experimental Setup

A material testing machine (Instron 8874, Norwood, MA), located in the iCord lab at the Blusson Spinal Cord Centre on the site of the Vancouver General Hospital, was used to apply the physiological load discussed in Section 3.8, to each instrumented specimen.

The instrumented specimen was submersed in a 13 L fluid bath (Figure 3-20-a) of phosphate buffered saline (PBS) and protease inhibitor solution (Appendix C) and placed on the material testing machine. Three ball bearing parallels (TEC-50205, Thomas Skinner, Richmond, BCV) were placed between two 1/4" x 14" x 14" stainless steel plates on the base of the material testing machine to eliminate traction forces from the base of the fluid bath (Figure 3-20-b). A thermocouple, attached to an analog signal conditioner (Super MCJ, Omega Engineering Inc., Stamford, CT), was positioned 25 mm below the surface of the bath surface to monitor the temperature of the fluid.

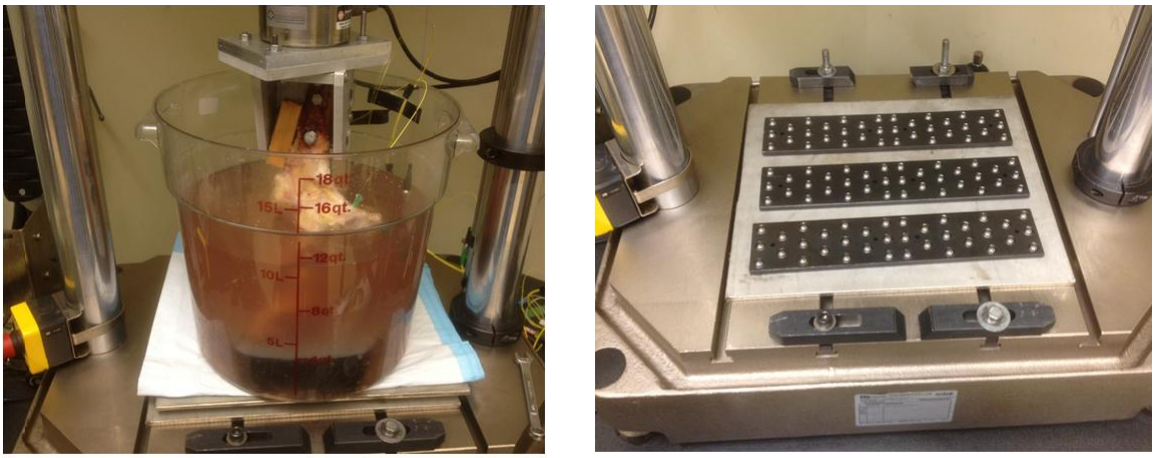


**Figure 3-20: Material testing machine experimental setup showing (a) fluid bath containing specimen and (b) ball bearing parallels to eliminate traction forces**

While submerged in the fluid bath, the specimen was attached to the material testing machine using an adjustable fixture with two 1/4" diameter bolts (Figure 3-21). The curved slot allows the adduction angle of the femoral shaft to be varied from 0º to 45º. Flexion is fixed at 13º ventral by the inclined front plate of the fixture and the adduction angle of the femoral shaft is set to 22º medial, as explained in Section 2.6, using a laser level before the two bolts are tightened (Figure 3-21-a). A safety stopper is inserted between the femoral shaft and edge of the fixture (Figure 3-21-b).

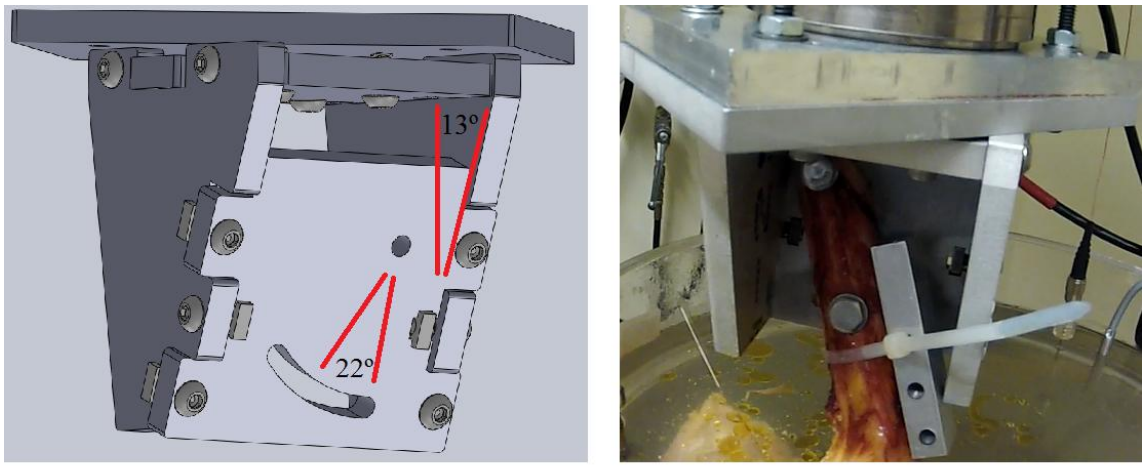


a) b)

**Figure 3-21: Adjustable fixture to mount femoral shaft to material testing machine; (a) angle of flexion is fixed at 13º, however, adduction is adjustable from 0º to 45º using the curved slot; (b) an aluminum block is used as a safety stopper.**

## 3.8 Representative Physiological Loading

A quasi-static load profile similar to Ferguson et al. (2003) was used in the current work. Ferguson et al. (2003) performed two types of tests:

1. Quasi-static creep load of 0.75 x BW for 3600 seconds
2. Sinusoidal creep test of 0.75 ± 0.25 x BW for 3600 seconds

In the current work, a sinusoidal creep load profile was chosen to capture semi-dynamic data. To represent physiological loading, the upper load limit of 2.38 x BW was chosen in accordance with the maximum force measured during normal walking in the *in vivo* study by Bergmann et al. (2001).

The complete load profile is shown in Figure 3-22. First, a preconditioning load of 20 N was applied for approximately one second to centre and seat the joint. The mean test load was intended to approximate a step load, however, the practical load rate limit of the material testing machine was 500 N/s. Once the mean load value has been reached, a sinusoidal variation of 25% BW at 1 Hz is imposed. The sinusoid is maintained for 3600 seconds before unloading at a slower rate of 100 N/s.

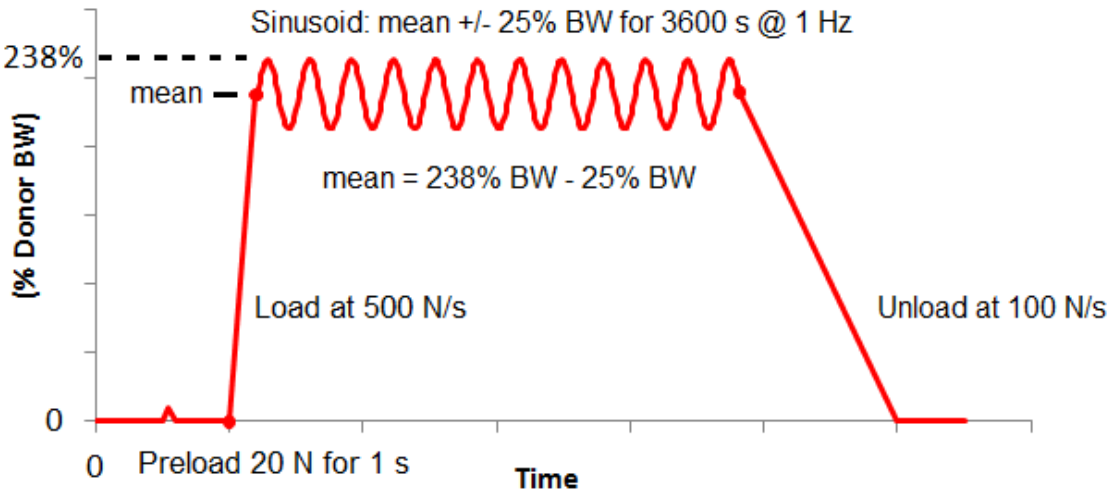


**Figure 3-22: Compressive sinusoidal creep load profile**

## 3.9 Data Acquisition During Experiments

The combined DAQ/optical interrogator system and software from Section 3.1 was used to collect all experimental data.

Analog voltage outputs from the material testing machine are recorded for the load cell and linear variable differential transducer attached to the linear actuator. The thermocouple analog voltage from the external amplifier is also recorded.

The experimental data was recorded at a rate of 10 Hz, which is the sampling rate of the optical interrogator. Analog inputs were sampled simultaneously at 1000 Hz and the mean of each sequential 100 points was calculated and recorded with the optical signal at 10 Hz.

## 3.10 Testing Protocol

Each specimen was tested over four sequential days. Days 1 to 3 were intended to establish repeatability of the measurements with the labrum intact. On Day 4, labral resection was intended to alter joint mechanics. The specimens were stored overnight in the fluid bath while surrounded by ice to reduce tissue decomposition (Figure 3-23).

**Figure 3-23: Specimen in fluid bath surrounded by ice for overnight storage between tests**

At the beginning of each test day, the fluid and specimen were installed on the material testing machine as explained in Section 3.7. To accelerate warming of the bath and

specimen to room temperature, a 500 W immersion heater (03046-00, Cole-Parmer, Montreal, QC) and 20 L aquarium pump were placed in the bath until the fluid reached room temperature, at which point the heater was removed.

The sensor response was monitored for 1 - 2 hours until the wavelength response from all FBG sensors stabilized, indicating the specimen and bath had reached thermal equilibrium. The pump was removed before testing began.

The detailed testing protocol for all four days is included in Appendix B.

### 3.11 Labral Resection

On the final day of testing, the anterior labrum was resected over the entire window in the joint capsule. The circumferential detachment of the labrum from the osseous rim of the acetabulum was thought to be clinically relevant as observed in FAI patients (Section 1.2). The labrum was resected with a scalpel leaving only small tabs or notches in the areas where the contact sensors pass through into the acetabular cartilage (Figure 3-24).

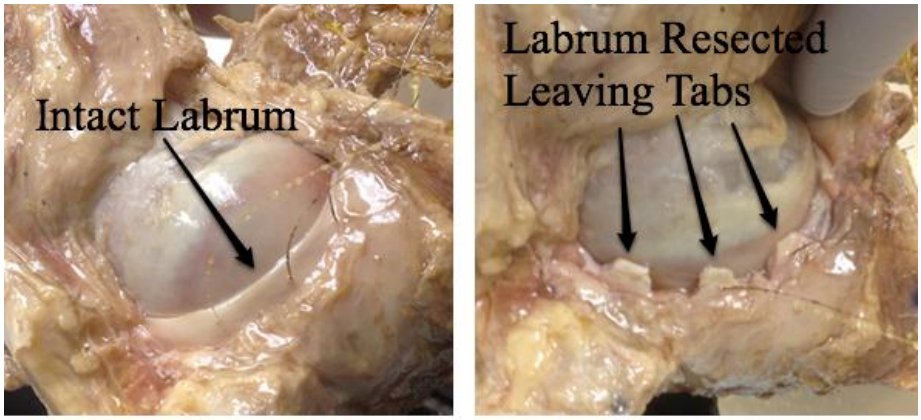


**Figure 3-24: Specimen 1 (a) before and (b) after resection of the anterior labrum leaving tabs where the contact stress sensors pass through the labrum**

After labral resection, the testing protocol was continued, explained in Appendix B.

# Chapter 4: Experimental Results and Discussion

The experiments in this thesis represent an attempt to take a significant step forward along the research path outlined in Chapter 1. Previously, the contact stress sensors had been modelled and calibrated in laboratory conditions before performing a pilot study on two cadaveric hips (Dennison et al. 2010). The pilot study was a single day, proof of concept experiment where one contact stress sensor was placed in the intra-articular joint space without emphasis on fixation or quantifying the location. The results of the experiment were sufficiently encouraging to justify scaling to the scope of this thesis.

During the course of the experimental work for this thesis, challenges were encountered, such as a femoral fracture and equipment failure reducing the amount of data available for comparison. Resource constraints required the use of non-ideal, pathological specimens. Lastly, analysis of the data revealed previously un-encountered artifacts in the contact stress sensor measurements. These limitations are discussed throughout the subsections.

This chapter presents the results and integrated discussion of the experimental work performed following the methods in Chapter 3. The chapter starts with the calibration sensitivities for both types of sensors used in the *ex vivo* measurements before presenting and discussing the repeatability of placement of these sensors within the joint. The durability of sensor fixation and inherent dependence on cartilage quality are the subject of the following two subsections.

The chapter continues with presentation and discussion of the experimental data collected for hydrostatic pressure in the fossa, consolidation of the joint, contact stress in

the acetabular cartilage, and temperature of the fluid bath in that respective order. A discussion of the study strengths and limitations concludes the chapter.

## 4.1 Sensor Calibration Results

Both the contact stress and hydrostatic pressure sensors were calibrated according to the methods in Section 3.1. Consistently, linear relationships between the sensor wavelength response and the known calibration values were observed (Figure 4-1).

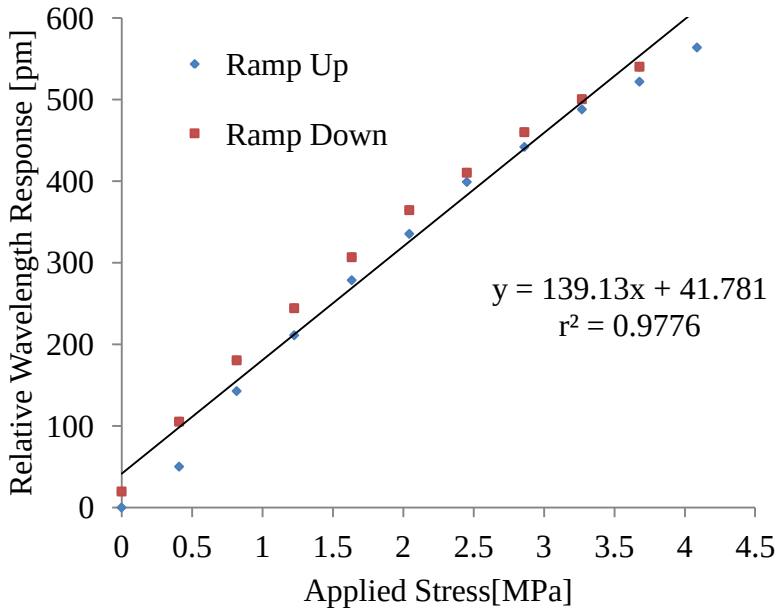


**Figure 4-1: The typical linear relationship between wavelength response and applied calibration stress value for one trial of contact stress sensor V-P**

The primary mean regression calculated sensitivities and sensitivity to thermal fluctuations are reported in Table 4-1 for both types of sensors.

**Table 4-1: Sensor Calibration Summary**

| Sensor Type | Mean Regression Calculated Sensitivities (min r^2) | STDEV of Mean Senstivities | Max Hysteresis (Average Hysteresis) | Temperature Sensitivity (min r^2) | Max Hysteresis |
|---|---|---|---|---|---|
| Contact: | [pm/MPa] | | | [pm/°C] | |
| V-I | 100.0 (0.963) | σ = 13.4 | 24.1% (9.4%) | 12.8 (0.997) | 6.2% |
| V-K | 117.1 (0.967) | σ = 13.4 | 12.0% (3.7%) | 15.5 (0.989) | 8.8% |
| V-L | 105.7 (0.984) | σ = 8.3 | 9.0% (3.4%) | 13.1 (0.999) | 3.2% |
| V-M | 145.0 (0.976) | σ = 4.3 | 11.4% (3.4%) | 12.6 (0.999) | 3.4% |
| V-P | 128.5 (0.965) | σ = 11.8 | 15.0% (5.9%) | 14.2 (0.994) | 7.5% |
| V-R | 108.4 (0.970) | σ = 11.5 | 13.4% (6.1%) | 13.6 (0.983) | 11.7% |
| Pressure: | [pm/MPa] | (3 trials) | | [pm/°C] | |
| PDB-5 | -169.2 (0.994) | σ = 3.7 | 6.7% | 10.6 (0.941) | 17% |

The sensitivity values in Table 4-1 are consistent with published values of contact stress sensors of the same design. Dennison et al. (2010) reported a sensitivity of 561.4 ± 6.6 pm·(N·mm$^{-1}$)$^{-1}$), or in alternate units 134.7 ± 1.6 pm·MPa$^{-1}$ for three angular positions with minimum correlation coefficient of 0.988. The standard deviation is notably higher in the current calibrations, ±4.3 to ±13.5 pm·MPa$^{-1}$, when compared with the value of ±1.6 pm·MPa$^{-1}$ from Dennison et al.(2010).

An explanation for the discrepancy in standard deviation of the sensitivities is the high hysteresis values in Table 4-1. These values were observed most frequently at the lowest calibration loads. This may result from the flexible tongue on the calibration apparatus (Figure 3-1 and Figure 3-2) not fully isolating the gauge blocks from the traction forces created when manually adding or removing calibration weights. Transmission of traction forces could cause translation of the top gauge block and consequently twisting of the two simple supports, affecting the sensor response. As the calibration loads increase in

comparison with the magnitude of the traction forces and the simple supports deform, the sensor becomes more isolated from torsion strains resulting in a lower average hysteresis as shown in Table 4-1. This hysteresis would also impact the strength of the linear correlation used to calculate the sensitivities.

The temperature calibrations in Table 4-1 were included to demonstrate the order of magnitude of the thermal effects if isothermal conditions were not maintained. The sensitivities remain close to published values of 10.6 pm/°C for FBG's in bare fiber (Measures 2001). As explained further in Section 4.3, an isothermal fluid bath for the specimens sufficiently prevents temperature drift in sensor response.

It was observed that when soaked in water or PBS+ solution the contact sensors experienced a gradual increase in wavelength response, while unstrained, which reached a steady value after one hour. In Table 4-1, the contact stress sensors were calibrated dry. Calibration was repeated for sensor V-M after soaking in room temperature PBS+ solution, as specified in Section 3.1. The mean sensitivity of sensor V-M when dry was $145.0 \pm 4.3$ pm·MPa$^{-1}$ for nine trials. After soaking in PBS+ for one hour, this value decreased by 6.3% to $139.5 \pm 4.2$ pm·MPa$^{-1}$ for six trials (Table 4-2).

Previous researchers have found that the Polyimide™ used in the contact stress sensor sheath, swells in the presence of water until saturated (Kronenberg et al. 2002; David et al. 2012). Swelling of the Polyimide™ sheath in the contact sensors likely constricts the silicon annuls, generating axial strain in the FBG and the resulting increase in wavelength response. Due to the complexity of calibrating the sensors in the saturated state, dry calibration values for sensitivities were used for the *ex vivo* experiments.

**Table 4-2: Calibration of Sensor V-M Before and After Soaking in PBS+ Solution**

| | Mean Sensitivities (min r^2) | STDEV of Means | Max Hysteresis (Average Hysteresis) |
|---|---|---|---|
| **V-M Dry:** | [pm/MPa] | | |
| 3 trials @ 0º | 148.2 (0.982) | σ = 1.9 | 7.3% (2.6%) |
| 3 trials @ 60º | 140.6 (0.983) | σ = 1 | 11.3% (4.4%) |
| 3 trials @ 120º | 146.2 (0.976) | σ = 4.8 | 8.3% (3.1%) |
| **Overall Dry:** | **145 (0.976)** | **σ = 4.3** | **11.3% (3.3%)** |
| **V-M Wet:** | [pm/MPa] | | |
| 2 trials @ 0º | 139.5 (0.98) | σ = 3.5 | 11.5% (6.1%) |
| 2 trials @ 60º | 136 (0.974) | σ = 2.9 | 15.9% (6.3%) |
| 2 trials @ 120º | 132.2 (0.978) | σ = 3.6 | 9.1% (4%) |
| **Overall Wet:** | **135.9 (0.974)** | **σ = 4.2** | **15.9% (5.5%)** |

## 4.2 Accuracy and Repeatability of Sensor Placement

Using the imaging procedure in Section 3.6, the locations of all sensors within the specimens were recorded as displayed in Figure 4-2.

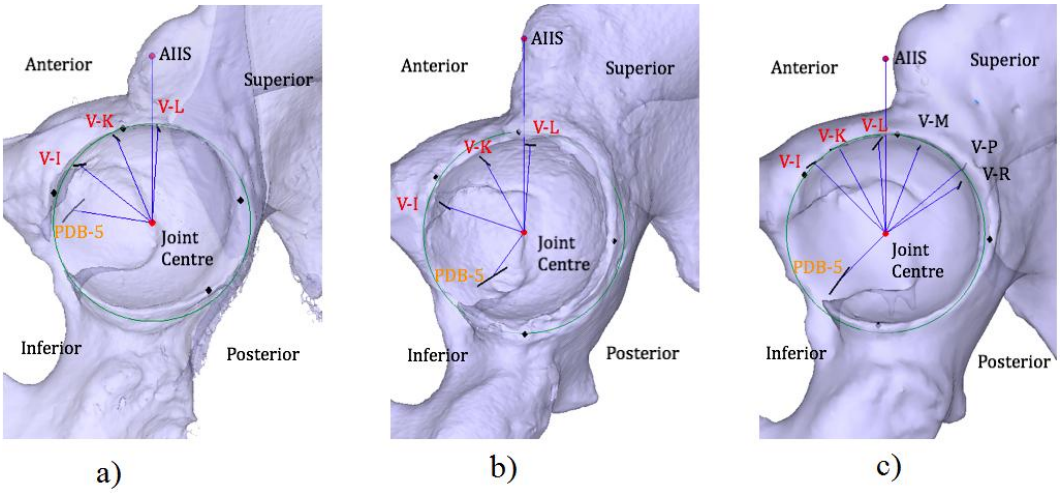


**Figure 4-2: Radial position of all sensors for (a) Specimen 1, (b) Specimen 2 and (c) Specimen 3. Positive angular displacement is anterior of the AIIS. The image of Specimen 3 (right hip) has been flipped horizontally to match the images of 1 and 2 (left hips)**

The target angular position of V-L was 0º relative to the AIIS with V-K and V-I at +25º and +50º respectively (Section 3.6). The experimental mean position of V-L was observed to be -1º ± 5º, with the V-K and V-I located at +27º ± 3º and +56º ± 14º respectively (Table 4-3). The published accuracy and precision of the imaging technique are 1.03 mm/1.45º and 0.26 mm/0.57º respectively (Amiri et al. 2012).

**Table 4-3: Summary of Radial Sensor Positions**

| | V-I | V-K | V-L | V-M | V-P | V-R | PDB-5 |
|---|---|---|---|---|---|---|---|
| Specimen 1: | +51° | +23° | -4° | - | - | - | +81° |
| Specimen 2: | +72° | +29° | -4° | - | - | - | +145° |
| Specimen 3: | +45° | +29° | +5° | -21° | -50° | -57° | +135° |
| Mean | +56° | +27° | -1° | | | | +120° |
| STDEV | (σ=14°) | (σ=3°) | (σ=5°) | | | | (σ=34°) |

The small sample size of this study is insufficient to determine significance of the repeatability of sensor insertion, however, the results above are a positive indication of a potentially repeatable method. The three sensors used in all specimens were placed in radial positions with standard deviations as low as ±3º between specimens (Table 4-3). The additional sensors V-M, V-P and V-R that were used in Specimen 3 were inserted at -21º, -50º and -57º, compared with their desired positions of -20º, -40º and -60º (Section 3.5). Sensors V-M and V-R are within ±3º of the intended position, however, an error is suspected in the registration of sensor V-P from the biplanar radiographs. By inspection of Figure 3-9, the angular position of the posterior three contact stress sensors is highly

uniform compared with the near overlapping position of sensors V-P and V-R in Figure 4-2.

The hydrostatic pressure sensor was initially placed at +81º in the anterior-inferior region of the fossa of Specimen 1, resulting in sensor malfunction (Section 4.3). For Specimens 2 and 3, the insertion location was revised, locating the sensor in the posterior-inferior region of the fossa at +145º and +135º respectively. The later region of the fossa resulted in successful pressure measurements (Section 4.5).

The insertion distance of the sensors into the acetabulum is illustrated by the position of the distal 10 mm of the insertion needles in the acetabulum (Figure 4-3). Consistent qualitative results in the figure below provide a degree of confirmation of similar insertion distances into the acetabulum, for all sensors, using the insertion procedure (Section 3.5). The distance of the needle tip to the osseous perimeter could not be quantified using the computer-assisted process.

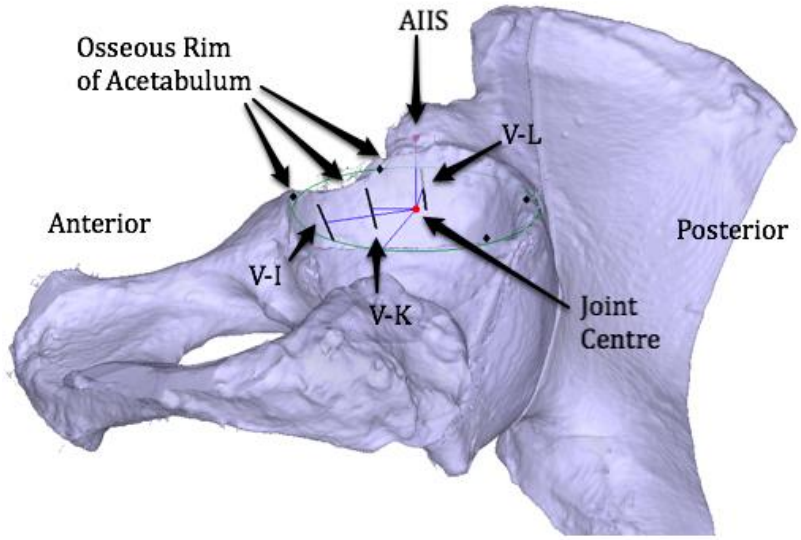


**Figure 4-3: Tilted view of acetabulum from Specimen 1 showing typical consistent insertion distance below the rim of the acetabulum.**

### 4.3 Durability of Sensor Fixation

During the 4-day test protocol (Section 3.10) that was carried out for each specimen, several issues regarding the durability of fixation of the sensors were observed (Table 4-4). For Specimen 1 on all days, pressure sensor malfunction compromised data and on Day 3, there was an error with the DAQ equipment resulting in a complete loss of data for all measurements. For Specimen 3 on Day 1, sensor V-I was damaged by excessive bending or strain and on Day 3, catastrophic failure of the femur stopped the test and damaged sensor V-R.

**Table 4-4: Operational Status of All Sensors Throughout Testing**

| | V-I | V-K | V-L | V-M | V-P | V-R | PDB-5 |
|---|---|---|---|---|---|---|---|
| **Specimen 1:** | | | | | | | |
| Day 1 | OK | OK | OK | - | - | - | Error! |
| Day 2 | OK | OK | OK | - | - | - | Error! |
| Day 3 | Error! | Error! | Error! | - | - | - | Error! |
| Day 4 | OK | OK | OK | - | - | - | Error! |
| **Specimen 2:** | | | | | | | |
| Day 1 | OK | Dislodged | Ok | - | - | - | OK |
| Day 2 | OK | Dislodged | Ok | - | - | - | OK |
| Day 3 | OK | Dislodged | Dislodged | - | - | - | OK |
| Day 4 | OK | Dislodged | Dislodged | - | - | - | OK |
| **Specimen 3:** | | | | | | | |
| Day 1 | OK | OK | Dislodged | Dislodged | OK | OK | OK |
| Day 2 | Broken | OK | Dislodged | Dislodged | OK | OK | OK |
| Day 3 | Broken | OK/Error! | Dislodged | Dislodged | OK/Error! | OK/Broken | OK/Error! |
| Day 4 | Broken | OK | Dislodged | Dislodged | OK | Broken | OK |

On Specimen 3 Day 2, the signal of sensor V-I was observed to attenuate in the first 20 seconds of testing before disappearing completely, which is symptomatic of a localized pinch or sharp bend of the fiber pigtail or sensor. The signal for V-I did not recover as the

load was removed, indicating that the optical pathway had been broken. It is possible that V-I followed a curved through the labrum to enter the cartilage of the acetabulum resulting in excessive pinching of the fiber as load increased.

Two contact stress sensors were grossly dislodged from their initial position in each of Specimens 2 and 3 (Table 4-4). However, this may be a result of pathology as discussed in Section 4.4. From this point forward, only contact sensors where three or more days of data are available, will be discussed. These are limited to all three sensors in Specimen 1, sensor V-I in Specimen 2, and sensors V-K and V-P in Specimen 3.

For Specimens 2 and 3, where successful pressure measurements were made (Section 4.5), the pressure sensor was located in the posterior-inferior region of the fossa at +145º and +135º respectively. On Specimen 1, the pressure sensor was inserted in the anterior-inferior region of the fossa at only +81º and no pressurization was recorded. Malfunction of the pressure sensor is thought to have resulted from excessive bending strain on the pressure sensor housing, potentially from passing through the ligamentum teres which attaches in the anterior-inferior region of the fossa. Specimen 1 is omitted from discussions regarding pressure data from this point forward.

## 4.4 Effect of Cartilage Quality on Durability of Sensors

After the final day of testing, each specimen was disarticulated (Figure 4-4), to confirm correct sensor insertion and inspect the integrity of the cartilage surfaces. In all specimens the sensors were inserted in the middle or deep zones of the cartilage and no evidence of piercing the superficial surface was present.

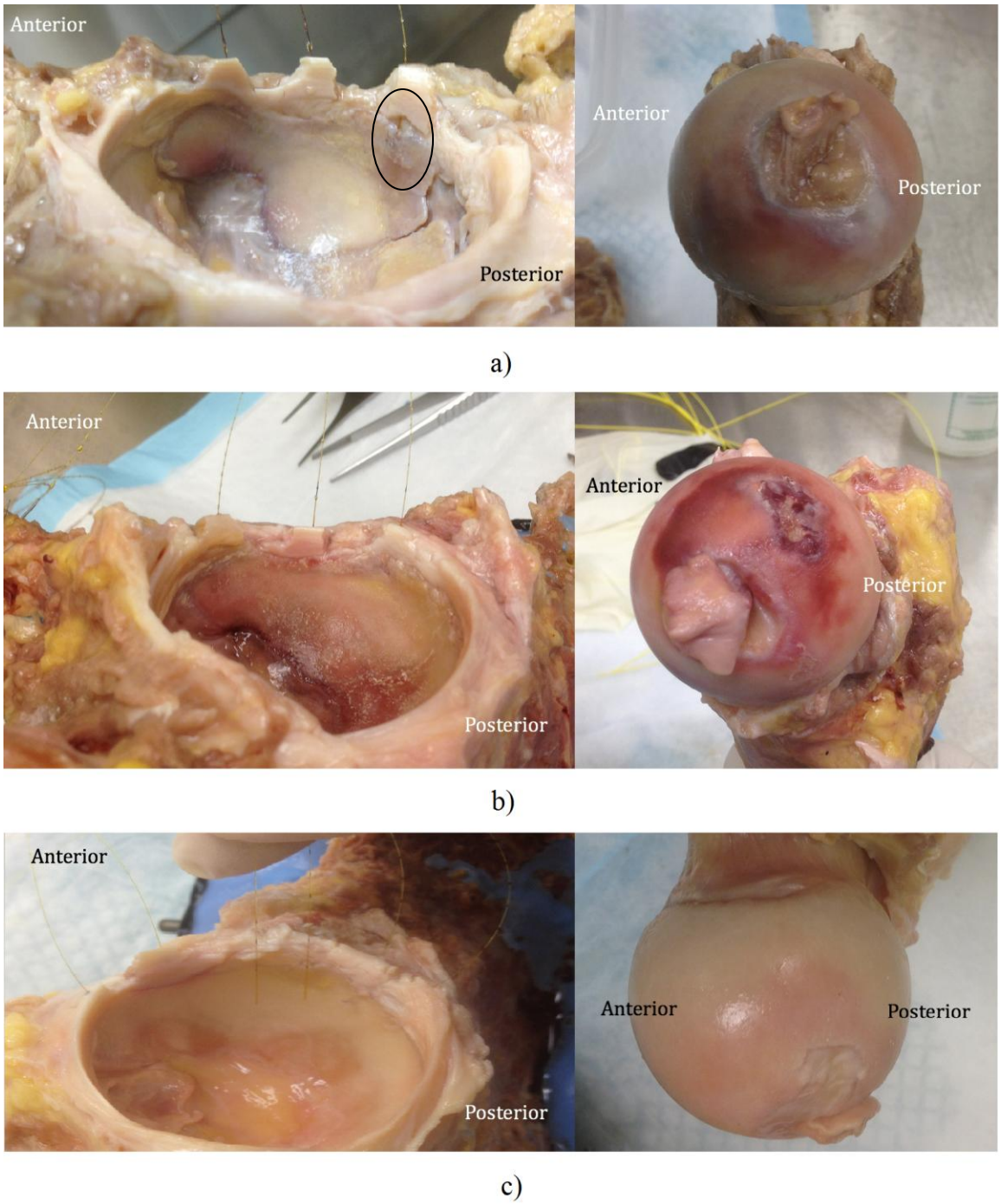


**Figure 4-4: Cartilage surfaces from (a) Specimen 1 (cartilage deterioration at the insertion site of sensor V-L circled), (b) Specimen 2 and (c) Specimen 3 after disarticulation on the final day of testing.**

When the contact stress sensors were removed following disarticulation, it was difficult to withdraw the sensors that were inserted into healthy cartilage. Sensors that were inserted into fibrillated areas of the labrum or pathological acetabular cartilage were either dislodged during transportation to the material testing machine and subsequent testing, or were easily withdrawn after disarticulation. In all specimens, lesions and discoloration of the cartilage on the femoral head were observed with the most severe lesions located on the posterior regions.

For Specimen 1, the anterior labrum and acetabular cartilage appeared normal and sensors V-I and V-K were difficult to remove from this region. In contrast, V-L was easily removed from the fibrillated area of the labrum and deteriorating acetabular cartilage adjacent to a major cartilage cleavage exposing the subchondral bone. Part of the sheath of sensor V-L was visible where cartilage was missing at the attachment site of the labrum to the acetabulum (circled in Figure 4-4-a), however the FBG region of the sensor was implanted under the surface of adjacent cartilage.

In Specimen 2 (Figure 4-4-b), the cartilage throughout the acetabulum appeared slightly calcified but otherwise normal. The labrum showed signs of fibrillation only in the region where sensors V-K and V-L were located. These two sensors became dislodged by approximately 50% of their insertion distance, resulting in the FBG residing in the labrum. Sensor V-I was difficult to remove from the intact labrum and cartilage.

The cartilage in Specimen 3 showed the least degeneration. The only pathology was a labral lesion directly in line with the radial position of the AIIS (Figure 4-5). Sensors V-L and V-M passed through the lesion and were fully dislodged during testing despite the use of cyanoacrylate in an attempt to bond the sensors to the labrum.

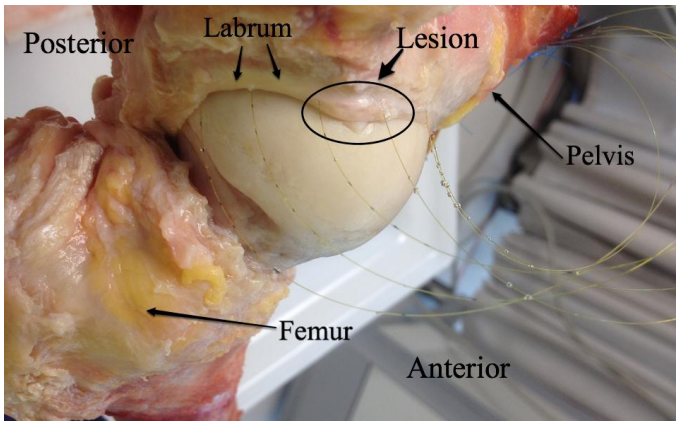


**Figure 4-5 : Sensors passing through lesion in labrum of Specimen 3**

As indicated by the frequency with which contact sensors become dislodged when passing through pathological areas of the labrum or articular cartilage, the integrity of sensor fixation appears highly dependent on the localized tissue quality in this small number of samples.

## 4.5 Hydrostatic Pressure Measurements in the Fossa

Hydrostatic pressure in the fossa was successfully measured for Specimens 2 and 3 only, as explained in Section 4.3. When viewed on a short timescale (Figure 4-6), the pressure sensor response is in phase and increases with applied load for both specimens.

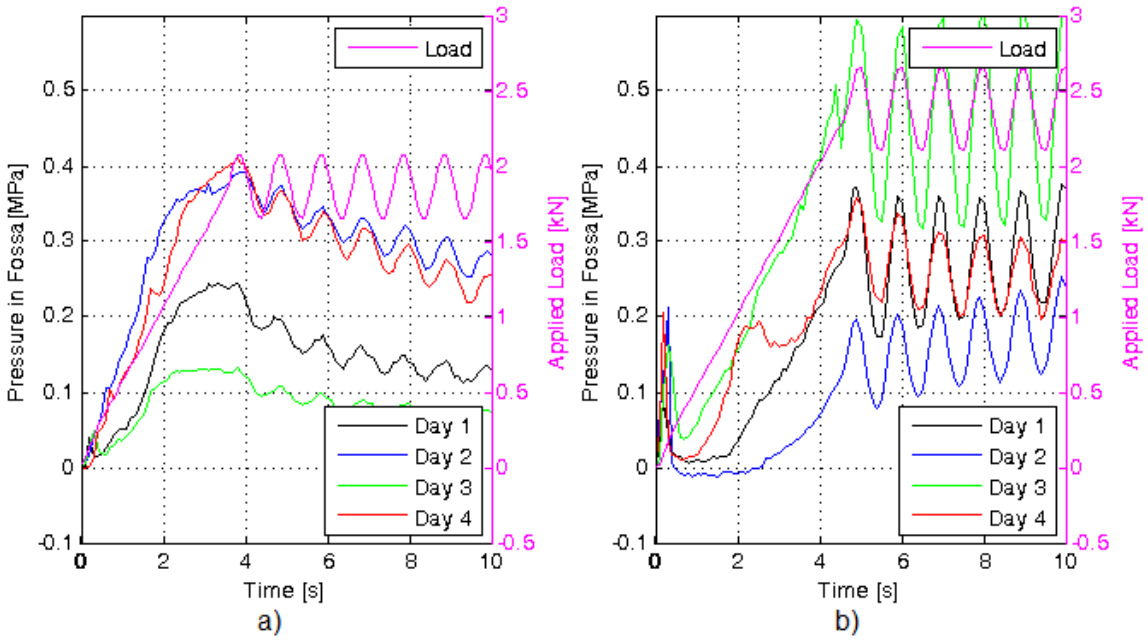


**Figure 4-6: Hydrostatic synovial fluid pressure and applied load vs time for (a) Specimen 2 and (b) Specimen 3.**

The initial rise to a peak pressure in response to a steady increase in applied load by the materials testing machine is expected as explained in Section 2.2, since hydrostatic load transfer comprises 69% to 79% (Park et al. 2003) of the load transfer across the joint. As the load increases, the hydrostatic pressure is expected to climb as a result of the sealing function of the labrum (Ferguson et al. 2000a, p.200; Ferguson et al. 2000b) and contacting surfaces of the articular cartilage (Hlavacek 2002; Ateshian 2009). Both specimens a exhibited a pseudo-linear initial increase in pressure, however, slippage of the femur on the adjustable mounting fixture (Figure 3-7) occurred between 2 to 4 seconds on Day 4 for Specimen 3, resulting in a distinct step. An initial delay in pressurization is noted in Specimen 3.

The maximum transient pressure was reached in both specimens within the first 100 seconds of the test (Figure 4-7).

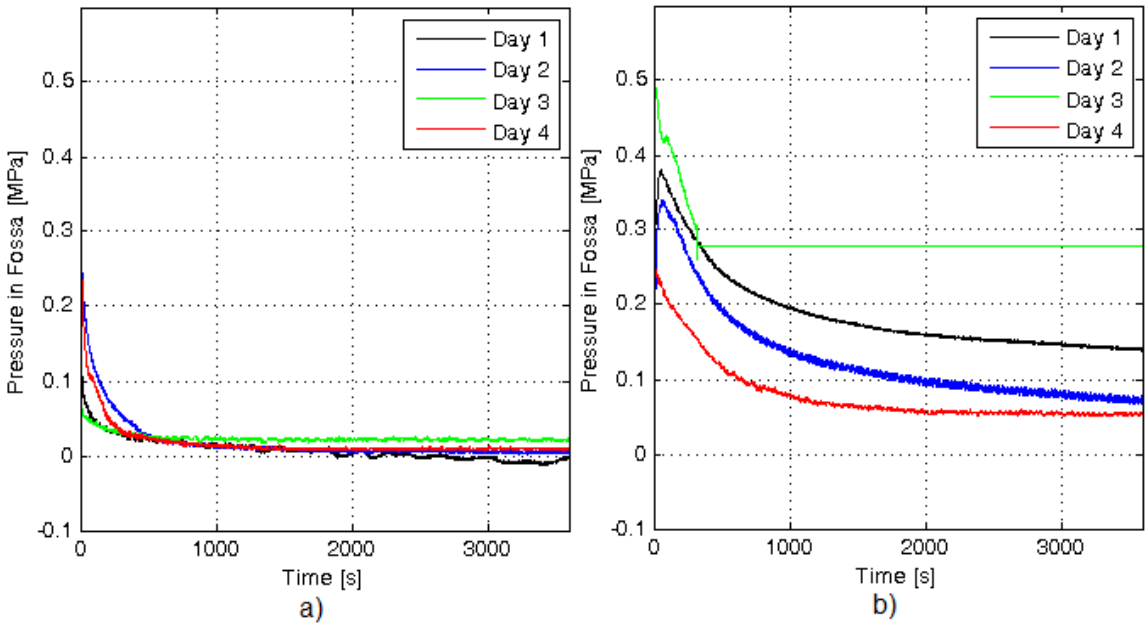


**Figure 4-7: Hydrostatic synovial fluid pressure measured in the fossa vs. time for (a) Specimen 2 and (b) Specimen 3. For clarity, a one second moving average was used, starting at the first peak of the sinusoidal loading cycle at 4.0 sec and 5.2 sec for Specimens 1 and 2 respectively.**

In contrast to Ferguson et al. (2003), no clear qualitative difference in the pressure response was observed between the intact labrum (Day 1 to 3) and without the labrum (Day 4) (Figure 4-7). The expected pressure response (Figure 2-7) was a consistent, nominally higher maximum pressure and slower decay with the labrum, than without the labrum, based on the work of Ferguson et al. (2003) as described in Section 2.5.

For both Specimens 2 and 3, the greatest relative difference between the maximum observed pressure during the test and the final mean pressure occurred on the day without the labrum.

**Table 4-5: Summary of Hydrostatic Pressure Measurements in the Fossa**

| | Max Pressure [MPa] | Mean Last 20 sec. [MPa] | Difference [MPa] |
|---|---|---|---|
| **Specimen 2:** | | | |
| Day 1 | 0.24 | 0.00 | 0.25 |
| Day 2 | 0.39 | 0.00 | 0.39 |
| Day 3 | 0.13 | 0.02 | 0.11 |
| Mean | 0.26 ($\sigma = 0.13$) | 0.01 ($\sigma = 0.01$) | 0.25 ($\sigma = 0.14$) |
| Day 4 | 0.41 | 0.01 | 0.40 |
| **Specimen 3:** | | | |
| Day 1 | 0.38 | 0.14 | 0.24 |
| Day 2 | 0.34 | 0.07 | 0.27 |
| Day 3 | 0.59 | n/a | n/a |
| Mean | 0.44 ($\sigma = 0.14$) | 0.11 ($\sigma = 0.05$) | 0.25 ($\sigma = 0.02$) |
| Day 4 | 0.36 | 0.05 | 0.31 |

Using a cyclic load profile similar to the current study, Ferguson et al. (2003) observed peak pressures of 0.550 ± 0.056 MPa with the labrum intact that were reduced to 0.195 ± 0.145 MPa without the labrum, that decayed to a common near-zero value. As in Table 4-5, the peak pressure for Specimen 2 of 0.41 MPa without the labrum was higher than the mean maximum pressure of 0.26 ± 0.13 MPa for days with the labrum. In the case of Specimen 3, the peak pressure without the labrum, 0.36 MPa, was lower than the mean pressure of 0.440 ± 0.14 MPa for the days with the labrum intact, however, the specimen was mounted with a slightly different orientation after fracture of the femur. While Specimen 2 decayed consistently to a near zero value similar to Ferguson et al. (2003), the mean values at the end of the test for Specimen 3 were 0.14 MPa and 0.07 MPa for days with the labrum and 0.05 MPa without the labrum (Table 4-5).

The greatest difference between the maximum pressure and the final mean pressure for both specimens was observed on the final day, which contrasts with the implied observation of Ferguson et al. (2003) that the difference between maximum and final pressures decreased after labral resection.

Disagreement between previous findings and the current experiments may arise from differences in experimental procedures. Ferguson et al. (2003) performed a series of four 1 hour consolidation tests on each specimen, the later two after labral resection, each separated by a 1 hour period for the cartilage to recover and rehydrate. More recent studies have shown that up to 16 hours is required for full cartilage thickness recovery in dead tissue (Greaves et al. 2009) which may be required to fully restore joint behaviour. Pressure measurement in the fossa may be highly sensitive to the alignment of the joint on the material testing machine. In the current work, both specimens were removed and remounted onto the material testing machine each sequential day, possibly decreasing the repeatability. It is thought Ferguson et al. (2003) left the specimens attached throughout the entire testing protocol, reducing this uncertainty.

Lastly, pathology of the labrum noted in Section 4.4 for Specimens 2 and 3 may imply that the sealing function of the labrum had already been compromised. This may explain the lack of a dramatic difference in synovial fluid pressure following labral resection for this small number of samples.

### 4.6 Overall Joint Consolidation

The materials testing machine linear actuator displacement provides an indication of joint consolidation including the deformation of osseous anatomy and shifting within the potting material. The magnitude of the displacement exhibits high variability between

sequential days of testing (Figure 4-8-a). To make a more standardized comparison, the data is zeroed relative to the value at the peak of the first sinusoidal cycle (Figure 4-8-b) and referred to here after as the standardized displacement.

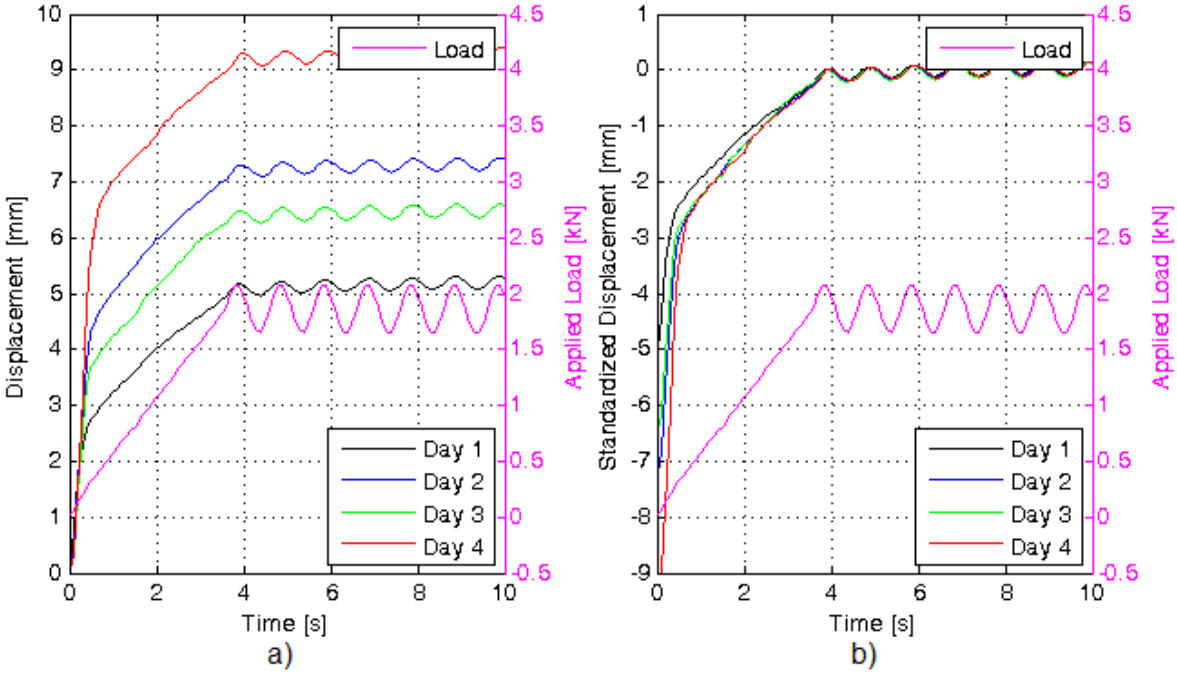


**Figure 4-8: Displacement of linear actuator and applied compressive load (pink) vs time for Specimen 2, shown as (a) absolute and (b) standardized relative to the peak value of the first sinusoidal cycle at 4.0 sec. Positive values indicate consolidation of the joint.**

It is hypothesised in this thesis, that absolute displacement values (Figure 4-8-a) exhibit high variability between days partially because the force used to seat the joint before testing was only 5-10 N. The joint displaces significantly throughout the initial portion of loading until more substantial loads of approximately 500 N are reached (Figure 4-8-b). Seating the joint with a low force is difficult, however, excessive preload could expunge fluid from the joint space reducing the hydrostatic pressure in the fossa.

Specimens 1 and 2 show a decrease in overall standardized displacement for sequential days with the labrum intact (Figure 4-9-a/b). Observations on the final day of testing, without the labrum, were an increase in standardized displacement for Specimen 1 and the same profile for Specimen 2. It is possible that decreases in standardized displacement between sequential days results from incomplete cartilage thickness recovery between tests.

Specimen 3, in which the femur failed, showed the opposite trend with increasing standardized displacement for the intact labrum and a dramatic increase on Day 3 before fracture (Figure 4-9-c). The data without the labrum was collected after the femur had been remounted and shows an increase in consolidation from previous days. Slippage of the femur in the mounting fixture occurred in the first 4 sec on the day without the labrum, however, the data was standardized at 5.2 sec reducing the impact.

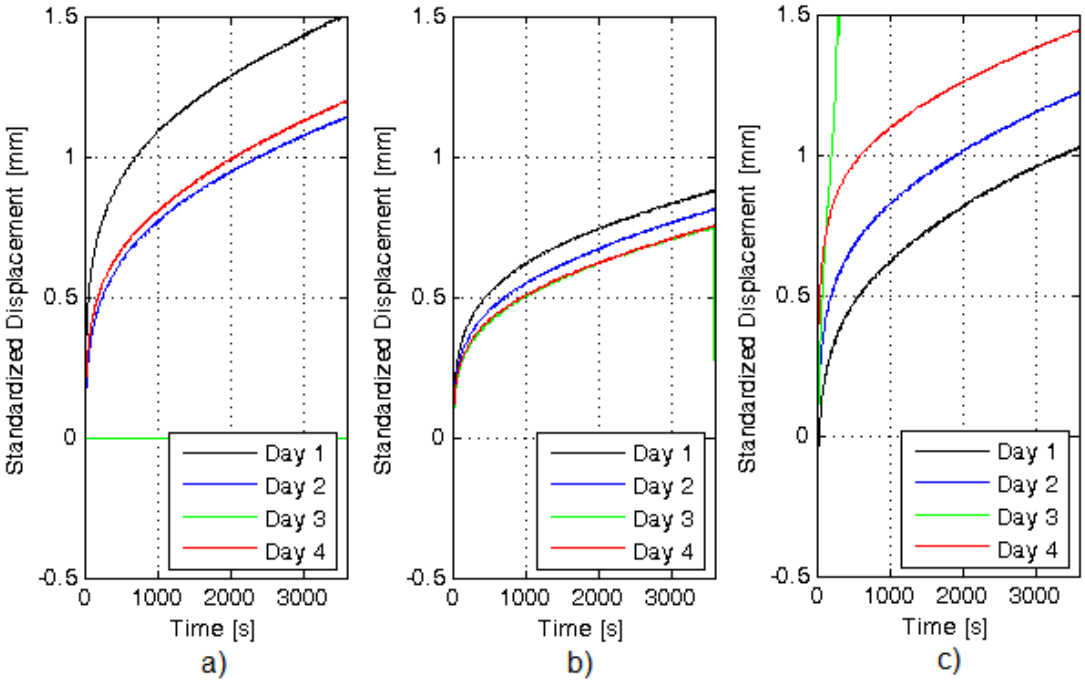


**Figure 4-9: Standardized linear actuator displacement vs time for (a) Specimens 1, (b) Specimen 2 and (c) Specimen 3. For clarity, a one second moving average was used, starting**

**at 3.3, 4.0 and 5.2 seconds for Specimens 1, 2, and 3 respectively. Positive values indicate consolidation of the joint.**

The normalized displacement in Table 4-6 is calculated as the standardized displacement divided by the peak applied load of 238% BW from Section 3.8.

**Table 4-6: Normalized Final Displacement of Linear Acutator**

| | Specimen 1 [μm/N] | Specimen 2 [μm/N] | Specimen 3 [μm/N] |
|---|---|---|---|
| Day 1 | 0.89 | 0.42 | 0.39 |
| Day 2 | 0.67 | 0.39 | 0.46 |
| Day 3 | n/a | 0.36 | n/a |
| **Mean** | **0.78** | **0.39** | **0.42** |
| STDEV (σ) | 0.15 | 0.03 | 0.05 |
| | | | |
| **Day 4** | **0.71** | **0.36** | **0.54** |
| % Increase | -9% | -5% | 24% |

.

Comparison of the values for Specimens 2 and 3 with the labrum intact, show similar mean normalized displacements of 0.39 ± 0.03 μm/N and 0.42 ± 0.05 μm/N, respectively (Table 4-6). The mean value for Specimen 1 with intact labrum was nearly double at 0.78 ± 0.15 μm/N.

After resecting the labrum, a decrease in normalized displacement of 5% and 9% respectively for Specimens 1 and 2 was observed (Table 4-6). By contrast, Specimen 3 agreed with the work of Ferguson et al. (2003), exhibiting a 24% increase in normalized displacement without the labrum. Ferguson et al. (2003) observed a 21% increase ($p = 0.02$) in the final displacement following labral resection from 0.824 ± 0.126 μm/N to 0.997 ± 0.232 μm/N. The normalized mean displacements for days with the labrum, in

Table 4-6, were nominally lower that the observations of Ferguson et al. (2003) by 5.3%, 53% and 49% for Specimens 1, 2 and 3 respectively.

As explained in Section 4.5, additional possible explanations for discrepancies between the results and Ferguson et al. (2003) are the differing cartilage recovery periods and repeated removal of the specimens from the material testing machine.

## 4.7 Solid Matrix Stress Contact Measurements in Cartilage

A high degree of variability from day to day was observed in the response of the six contact stress sensors for which data on three or more days was collected. Included are all three contact stress sensors from Specimen 1 (Figure 4-10), one sensor from Specimen 2 (Figure 4-11), and two sensors from Specimen 3 (Figure 4-12).

Two sensors registered sustained solid matrix stresses above zero. These were Specimen 1 V-L on Day 2 reaching 0.21 MPa and Specimen 3 V-P on Day 4 reaching 0.69 MPa. Dennison et al. (2010) observed similar peak values of 0.16 ± 0.03 MPa and 1.5 ± 0.06 MPa from two specimens for five trials of a single similar contact stress sensor using a smaller load of 50% body weight. The measurements of 0.21 MPa and 0.69 MPa are also on the same order as the findings of Adams et al. (1999) that directional total contact stress measurements differed by 0.5 to 1 MPa between orthogonal orientations for physiological loads in cartilage plug specimens. The difference between orthogonal directional measurements may approximate the magnitude of the solid matrix stress (Section 2.2).

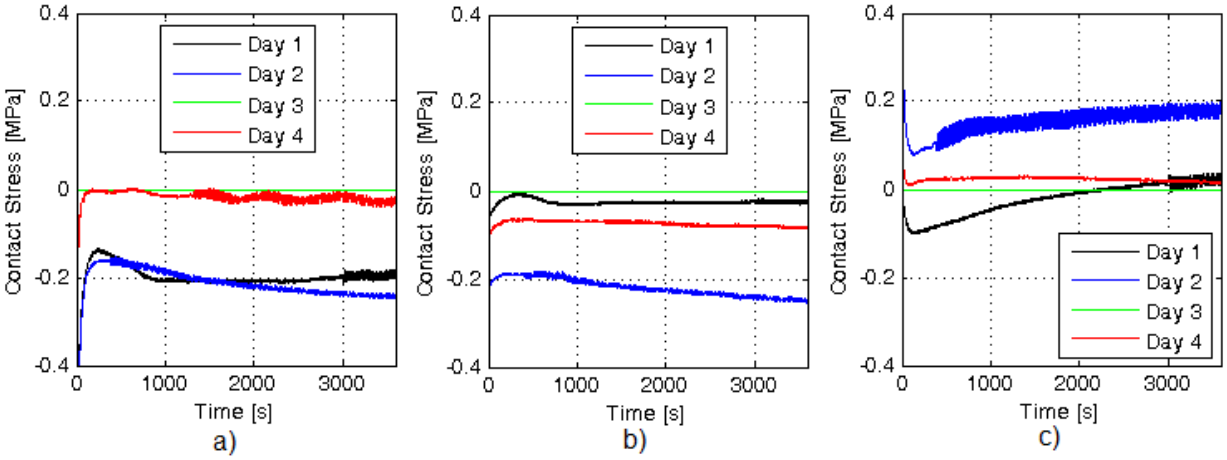


**Figure 4-10 : Solid matrix stress vs. time, Specimen 1 sensors (a) V-I, (b) V-K and (c) V-L**

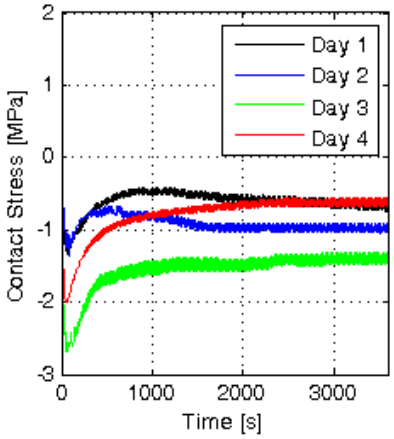


**Figure 4-11: Solid matrix stress vs. time for Specimen 2 sensor V-K**

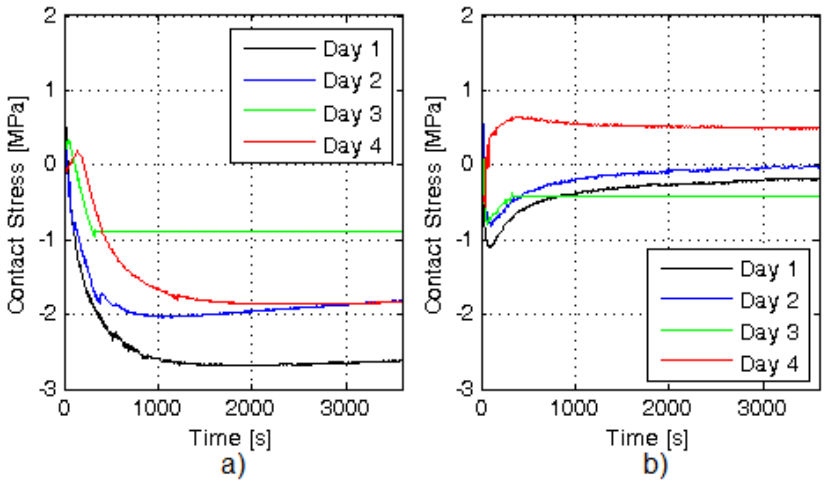


**Figure 4-12: Solid matrix stress vs. time for Specimen 3 sensors (a) V-I and (b) V-P**

Compared with the findings of previous *ex vivo* studies in Section 2.4, the measurements of 0.21 MPa and 0.69 MPa for the solid matrix stress are nominally lower than contact stress values in other studies. From inspection of Table 2-1, measurements of peak contact stress generally fall on the order of 5 to 10 MPa with average contact stress ranging between 2.5 to 5.0 MPa. While the sensors used in the current experiments are sensitive only to the solid matrix stress, pressure sensitive films and other transducers, used in Section 2.4, also capture some component of the hydrostatic synovial fluid stress. These combined measurements may be interpreted as a measure of total contact stress and are expected to be higher than measurements of only the solid matrix stress subcomponent. The advantage of using fiber optic sensors over the other methods is that disarticulation of the joint is not required to insert fiber optic sensors.

Scenarios where the solid matrix stress decreases to a negative value upon loading, using Figure 4-10-a as a typical example, reveal the potential influence of cross-sensitivity to other phenomenon including bending, axial strain, or torsion of the sensors. The contact stress sensors use a volume maintaining sheath to transform applied transverse force into Poisson strain of the silicon annulus and concentric FBG (Dennison et al. 2010). The resulting wavelength response to transverse loading is therefore always positive (Dennison et al. 2010).

Qualitative inspection of Figure 4-10-a/c and Figure 4-12-b shows similarity, with respect to the overall shape of the sensor response profile between sequential days of testing with the labrum intact, for each of the three sensors. Although vertical offsets exist between results, as in Figure 4-10-c, the similar shape of the profiles demonstrates a

degree of repeatable relative change throughout the tests. The observation that the sensors in Figure 4-10-a/b, Figure 4-11, and Figure 4-12-b consistently reach steady long-term values implies loading conditions for the sensors reach a state of equilibrium by the end of the test.

The difference between the maximum and minimum values of solid matrix stress for each sensor showed variability between specimens. However, the three sensors in Specimen 1 ranged from 0.09 to 0.52 MPa while the two sensors from Specimen 3 ranged from 3.7 and 4.2 MPa, which show indications of consistency of different positions within the same specimen (Table 4-7).

**Table 4-7: Difference Between Maximum and Minimum Solid matrix stress Observations for t=1 to 3600 Seconds**

| | Mean Days 1-3 [MPa] | Day 4 [MPa] | % Change on Day 4 |
|---|---|---|---|
| **Specimen 1:** | | | |
| V-I | 0.52 ($\sigma$ = 0.06) | 0.45 | -13% |
| V-K | 0.09 ($\sigma$ = 0.01) | 0.06 | -33% |
| V-L | 0.28 ($\sigma$ = 0.15) | 0.12 | -57% |
| **Specimen 2:** | | | |
| V-I | 2.4 ($\sigma$ = 0.79) | 2.0 | -16% |
| **Specimen 3:** | | | |
| V-K | 4.2 ($\sigma$ = 0.31) | 1.5 | -63% |
| V-P | 3.7 ($\sigma$ = 0.38) | 4.1 | 10% |

Sensor V-P in Specimen 3 is a promising result based on the fact that similar profiles and long-term values (Figure 4-12-b) were observed for sequential days with the intact labrum, followed by a greater maximum/minimum difference and nominally higher, positive value after labral resection. This result is representative of the expected

measurements based on the findings of previous *ex vivo* experiments by Ferguson et al. (2003) that a decrease in synovial fluid pressure in the fossa and increase in overall joint consolidation are observed after labral resection. The decrease in pressure and increase in consolidation are hypothesised to increase cartilage matrix solid stresses to maintain equivalent load transfer across the joint (Section 2.2). The contact stress sensors measure the cartilage solid matrix stress (Section 2.2).

When comparing the mean difference between maximum and minimum for the intact labrum with the difference after labral resection, in all sensors except Specimen 3 sensor V-P, there was a reduction in difference on the final day without the labrum. In addition to the lowest difference between maximum and minimum commonly being observed after labral resection, the greatest nominal maximum and/or long-term steady values were observed in four of the sensors without the labrum.

When examining the contact stress sensor response on a timescale of five seconds, inconsistency in the phase relationship between sensor response and applied load is observed both between sensors and between sequential days for the same sensor. As shown in Figure 4-13, the sensor response can be characterized in one of three ways: in phase with the applied load, out of phase by $\pi/2$, or out of phase by $\pi$. The phase shift for all sensors is included in Table 4-8,

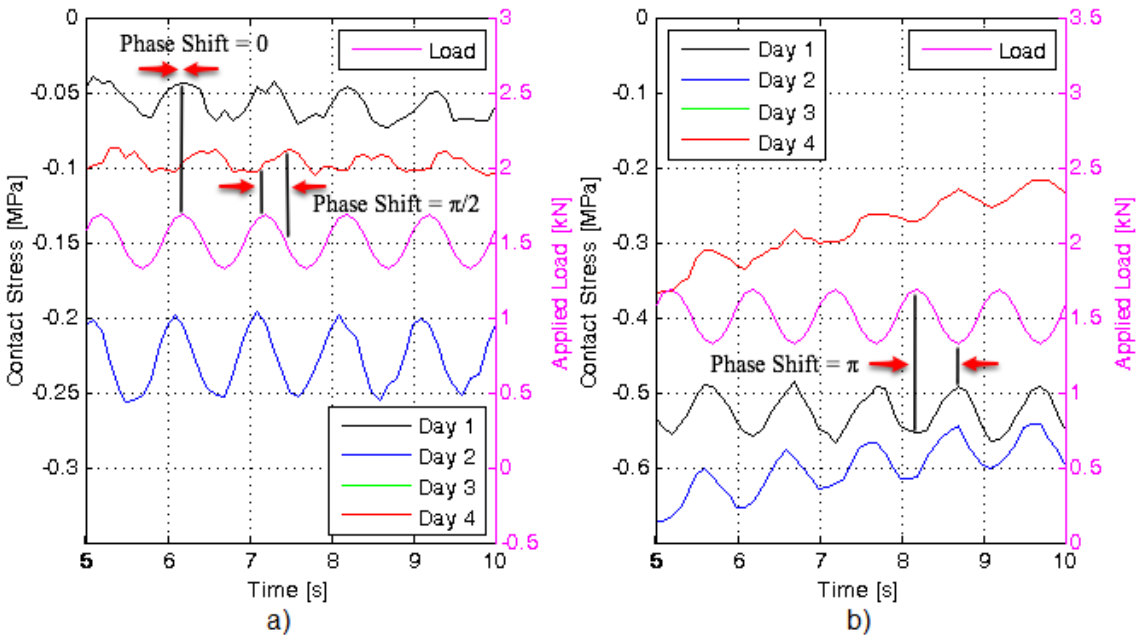


**Figure 4-13: Examples of contact stress sensor response phase shifts of 0, π/2, and π from applied compressive load (pink) in Specimen 1 for (a) sensor V-K and (b) sensor V-I.**

**Table 4-8: Summary of Phase Shift Throughout Testing**

| | V-I | V-K | V-L | V-M | V-P | V-R |
|---|---|---|---|---|---|---|
| **Specimen 1:** | | | | | | |
| Day 1 | π | 0 | π/2 | - | - | - |
| Day 2 | π | 0 | π/2 | - | - | - |
| Day 3 | - | - | - | - | - | - |
| Day 4 | π | π/2 | π/2 | - | - | - |
| **Specimen 2:** | | | | | | |
| Day 1 | π/2 | - | π | - | - | - |
| Day 2 | π/2 | - | π | - | - | - |
| Day 3 | π/2 | - | - | - | - | - |
| Day 4 | π/2 | - | - | - | - | - |
| **Specimen 3:** | | | | | | |
| Day 1 | 0 | π | - | - | π | π |
| Day 2 | - | π | - | - | π | π |
| Day 3 | - | π | - | - | π | π |
| Day 4 | - | π/2 | - | - | π/2 | - |

An indication that further investigation is required to characterize the influence of bending, axial strain or torsion, is the presence of a non-zero phase shift between the cyclic solid matrix stress measurements and the applied load. In the summary of the 27 entries in Table 4-8 for the phase shift between sensor response and applied load, 52% (14) were out of phase by $\pi$, 37% (10) were out of phase by $\pi/2$, and only 11% (3) were in phase. The case of a phase shift of $\pi$, where decreasing applied load results in increasing sensor response (Figure 4-13-b), may be symptomatic of an artifact, such as bending, being relieved as the applied load is decreased.

As mentioned previously, the qualitative consistency of some of the profiles and the existence of long-term steady values is encouraging. If axial strain, bending, torsion are affecting the measurements, these phenomenon appear to have the greatest influence as the applied load is ramped up to maximum value in the initial 3 to 5 second, where the highest overall consolidation is observed (Figure 4-8-b). Once the joint has reached a more quasi-static state after the peak load has been reached, an approach could be developed to zero the sensors to observed trends in response from that point forward.

In summary, it is difficult to draw conclusions regarding the repeatability of measurements from day to day or the effect of labral resection on solid matrix stress within the articular cartilage due to a combination of measurement artifacts, small number of specimens, and the fact that data is missing for Day 3 from both Specimens 1 and 3.

### 4.8 Temperature

As shown below in Table 4-9, in all tests except the first day of Specimen 1, the temperature drift of the surface of the uncirculated fluid bath between the start and finish

of the test was between +0.1 ºC and -0.4 ºC. For Specimen 1 Day 1 the temperature drift over 1 hour was -2.9 ºC.

**Table 4-9: Fluid Bath Temperature Drift Measured Between Start and Finish of Test**

| | Specimen 1 [°C] | Specimen 2 [°C] | Specimen 3 [°C] |
|---|---|---|---|
| Day 1 | -2.9 | -0.3 | 0.0 |
| Day 2 | -0.4 | 0.1 | 0.1 |
| Day 3 | n/a | -0.2 | n/a |
| Day 4 | 0.0 | -0.1 | -0.2 |

Although Specimen 1 Day 1 experienced a higher temperature drift at the bath surface, the rate of change of temperature inside the joint at the sensor location was not sufficient to affect the sensor response.

Using the sensitivities from Section 4.1, the predicted change in wavelength response for a temperature drift of -2.9 ºC is approximately -38 pm, -47 pm, and -39 pm for sensors V-I, V-K, and V-l respectively. This would correspond to a gradual decrease in contact stress observations of 0.38 MPa, 0.39 MPa, and 0.37 MPa for sensors VI, V-K and V-L respectively during testing on Day 1 only. The change in response would be reflected in the experimental data if the rate of change of temperature at the centre of the joint was similar to that of the bath surface. Inspection of Figure 4-10 does not show any indication of a drop in solid matrix stress on the first day of testing compared with subsequent days where the still fluid bath remained isothermal at the surface. As a result, all data has been analysed treating the bath as isothermal.

## 4.9 Study Strengths

Two types of fiber optic sensors were manufactured and calibrated with sensitivities consistent to those in previous work by Dennison et al. (2010). The method used to insert the contact stress sensors within the middle zone of the cartilage and quantify their location using a RSA radiographic approach shows promise, justifying further investigation. Implantation of all sensors using only hypodermic needles lends itself to future study where sensors could be inserted into specimens through a fully intact joint capsule or into other hard to access areas. Fixation based on the degree of force required to remove sensors after disarticulation indicates healthy areas of the cartilage or labrum are the most suitable for sensor implantation.

Although results of the fluid pressure measurements in the fossa and overall joint consolidation were not in agreement with findings of previous experiments by other researchers, the response of the data collected for both of these quantities was in phase with the applied load, suggesting correct sensor function.

Again, while the contact force sensors did not validate either of the primary research objectives of this study, encouraging observations were made. Findings indicate that repeatable measurements from day to day, and validation of changes in solid matrix stress after labral resection may be possible with further work to reduce measurement artifact from cross-sensitivities.

A room temperature fluid bath of sufficiently large thermal mass was successful in maintaining isothermal conditions throughout the one hour tests.

## 4.10 Study Limitations

The use of hemipelvis specimens improves economic feasibility at the cost of potential errors when potting the specimens in representative physiological alignment. Without the

other half of the pelvis, the medial-lateral tilt of the hemipelvis in the coronal plane must be performed by visually comparing a foam model of the pelvis. The potential for substantial deviation from physiological alignment at this step could affect joint mechanics and subsequent observations from the fiber optic sensors.

The 16 hour recovery period (Greaves et al. 2009) for the cadaveric articular cartilage requires the specimens to be repeatedly removed from the material testing machine and reattached. Sensitivity of both the fiber optic sensor responses and the measure of overall joint consolidation to changes in the alignment of the specimen on the materials testing machine have not been quantified, and could contribute substantially to errors. Particularly challenging is the alignment of neutral rotation once the specimen is attached to the material testing machine. Aligning the specimen in neutral rotation is done by visual inspection, however, the significant increase in opacity of the fluid bath throughout sequential days of testing makes this increasingly difficult.

The contact force sensors perform consistently in laboratory conditions when calibrated for transverse contact force, however, when used *in situ* cross-sensitivity artifacts from axial strain, torsion, bending, and swelling of the sheath in the presence of water may affect the measurements. Some of these artifacts have been quantified, such as swelling of the sheath, however, others such as bending remain unknown and are difficult to quantify.

Lower than expected durability and fixation of the contact force sensors within the articular cartilage, particularly in pathalogical regions, resulted in successful data collection for only 50% of the contact stress sensors that were inserted into the specimens.

Because the specimens could not be refrozen overnight while instrumented with the fragile sensors, the only means available to slow decomposition of the specimens during overnight storage was cooling the fluid bath by surrounding it with ice. This may not have been sufficient to prevent changes to the tissue over the four days of testing.

The use of small 5 to 10 N preload to seat the joint at the beginning of testing made it difficult to ensure a common zero point for displacement at the beginning of the test between days. A higher preload may excessively expunge fluid from the joint space and fossa affecting the pressure measurements, while the low preload makes accurate consistent measurement of the overall consolidation difficult.

Lastly, all specimens exhibited some degree of cartilage degeneration and/or pathology of the labrum even though the donor information sheets did not state previous medical history pertaining to the hip. Given the variable physiological condition of the specimens, the small sample size, and the inconsistent response of the optical sensors, it is not possible to draw significant conclusions regarding results from the experimental measurements.

# Chapter 5: Recommendations and Conclusion

As in the opening remarks for Chapter 4, this study faced many challenges throughout the experimental work. Although several limitations were identified, positive incremental steps were made toward realizing the research objectives. The following subsections contain recommendations to address the limitations identified in Chapter 4 and a summary of the major conclusions from the study.

## 5.1 Recommendations for Future Work

It is suggested that the complexity of the protocol could be reduced, to improve the probability of consistent completion of the complete protocol. This could be achieved in several ways including, reducing the cartilage recovery period so that the specimen does not need to be removed from the material testing machine. Additionally, eliminating the fluid bath and finding an alternate way to keep the joint space and tissues hydrated would reduce the complexity of sensor fixation. Lastly, adding incremental verification steps to confirm proper sensor function *in situ* as each sensor is fixated may allow diagnosis of artifact and an opportunity to correct it before executing the test protocol.

Further characterization of the contact force sensor of the current design, to cross-sensitivities from bending, torsion, and axial strain or the use of a sensor immune to these artifacts (Dennison & Wild 2012) may improve repeatability of the measurements from day to day. After these artifacts are quantified in laboratory conditions, characterization of the contact force sensor response in cartilage plug tests similar to the work of Adams et al. (1999) may lead to more clear interpretation of *ex vivo* results.

The durability of fixation of the contact stress sensors in the labrum and articular cartilage could be improved through the use of micro sutures in the surface of the labrum.

Adhesive could be used to bond the optical fiber connected to the sensors to the sutures instead of the smooth moist surface of the labrum. An investigation of the preload required to seat the joint and bring cross-sensitivity artifacts in the solid matrix stress measurements to a quasi-static state could improve the understanding of when to zero the response of the contact stress sensors and start recording overall joint consolidation.

The complexity of correctly potting hemipelvis specimens combined with the uncertainty of proper anatomical orientation outweighs the economic benefit of obtaining these specimens. In future work, a recommended approach would be to obtain full pelvis specimens and add markers for anatomical planes before separating each specimen into two hemipelvises. Literature also indicates that the use of full pelvis specimens with abductor muscle simulation may be more physiologically representative than the hemipelvis configuration using in this study (Bay et al. 1997).

## 5.2 Conclusions

The intent of this study was the development of a method for continuous, simultaneous measurement of hydrostatic synovial fluid pressure in the fossa and solid matrix stress within the articular cartilage matrix of cadaveric hemipelvis specimens using fiber optic sensors. This method seeks to improve upon the existing gold standard of contact studies which is the use of pressure sensitive films. These films are limited to capturing only a measure of the peak stress over the contact area. They also require introduction of a foreign film into the joint space and disarticulation of the joint before testing, both of which are hypothesized to permanently alter contact mechanics.

The primary objectives of this thesis were to establish the day to day repeatability of the method over three sequential days of testing before resecting the labrum on the fourth day of testing to observe changes in joint behavior.

Although the samples size was insufficient to determine significance, the mean radial positions of the contact stress sensors used in all hips were quantified to be -1º ± 5º, 27º ± 3º and 56º ± 14º relative to the AIIS compared with target values of 0º, 25º, and 50º. The locations were quantified using a system with a published accuracy and precision of 1.03 mm/1.45º and 0.26 mm/0.57º respectively (Amiri et al. 2012).

Limitations of the durability and fixation of the contact stress sensors in the acetabular cartilage resulted in successful data collection from only 50% of the inserted sensors, highlighting challenges with fixating sensors in pathological tissues. The use of the fluid bath was successful in maintaining isothermal conditions during the tests.

The hydrostatic synovial fluid pressure sensor response was in phase with the cyclic applied load, indicating correct sensor function. However, the low repeatability of the maximum observed pressure with the labrum intact of 260 ± 130 kPa and 440 ± 140 kPa, for Specimens 2 and 3 respectively, does not validate the repeatability objective of the study. The lack of a clear difference in response following labral resection on the final day does not support the findings of previous studies (Ferguson et al. 2003), however, by addressing some of the limitations in Section 4.10, more accurate statements may be possible.

Several challenges were encountered in measuring the cartilage solid matrix stress. The 50% failure rate of sensor fixation and small number of specimens, made it difficult to collect sufficient data for broad conclusions. Evidence exists suggesting the influence of

cross-sensitivity artifact from a combination of axial strain, bending, torsion, and swelling of the sensor sheath in the presence of water. The qualitative similarity of day to day profiles for the contact stress sensors was encouraging, however, these profiles were separated by a vertical shift between days that showed variability. Comparing the data without the labrum to the previous days with the labrum intact, a reduction in the difference between the maximum and minimum was observed in five sensors, with higher nominal maximum stress observed in four sensors without the labrum.

Of the two contact stress sensors with sustained measurements above zero, the observed values of 0.21 MPa and 0.69 MPa for solid matrix stress, are on the same order as measurements made by Dennison et al. (2010) of 0.16 ± 0.03 MPa and 1.5 ± 0.06 MPa. Both sets of cartilage solid matrix stress measurements are nominally lower than findings of previous *ex vivo* studies, where observations of the peak contact stress were on the order of 5 to 10 MPa with average contact stress ranging between 2.5 to 5.0 MPa. These previous *ex vivo* measurements, representing total contact stress, are expected to be higher than measurements of only the solid matrix stress subcomponent.

Although the primary objectives of this study were not validated, encouraging results were observed in several areas along with development of strategies to mitigate the limitations identified in this study, for future experiments.

# Bibliography

Adams, D. & Swanson, S.A., 1985. Direct measurement of local pressures in the cadaveric human hip joint during simulated level walking. *Annals of the Rheumatic Diseases*, 44(10), pp.658–666.

Adams, M.A. et al., 1999. Experimental determination of stress distributions in articular cartilage before and after sustained loading. *Clinical Biomechanics (Bristol, Avon)*, 14(2), pp.88–96.

Afoke, N.Y., Byers, P.D. & Hutton, W.C., 1987. Contact pressures in the human hip joint. *The Journal of Bone and Joint Surgery. British Volume*, 69(4), pp.536–541.

Afoke, N.Y., Byers, P.D. & Hutton, W.C., 1980. The incongruous hip joint. A casting study. *The Journal of Bone and Joint Surgery. British Volume*, 62-B(4), pp.511–514.

Afoke, N.Y., Byers, P.D. & Hutton, W.C., 1984. The incongruous hip joint: a loading study. *Annals of the Rheumatic Diseases*, 43(2), pp.295–301.

Amiri, S. et al., 2012. A model-free feature-based bi-planar RSA method for kinematic analysis of total knee arthroplasty. *Journal of biomechanical engineering*, 134(3), p.031009.

Amiri, S. et al., 2011. A novel multi-planar radiography method for three dimensional pose reconstruction of the patellofemoral and tibiofemoral joints after arthroplasty. *Journal of Biomechanics*, 44(9), pp.1757–1764.

Anderson, A.E. et al., 2010. Effects of idealized joint geometry on finite element predictions of cartilage contact stresses in the hip. *JOURNAL OF BIOMECHANICS*, 43(7), pp.1351–1357.

Anderson, A.E. et al., 2008. Validation of finite element predictions of cartilage contact pressure in the human hip joint. *Journal of Biomechanical Engineering*, 130, p.10pp.

Ateshian, G., 2009. The role of interstitial fluid pressurization in articular cartilage lubrication. *JOURNAL OF BIOMECHANICS*, 42(9), pp.1163–1176.

Backman, S., 1957. The proximal end of the femur: investigations with special reference to the etiology of femoral neck fractures; anatomical studies; roentgen projections; theoretical stress calculations; experimental production of fractures. *Acta Radiologica. Supplementum*, (146), pp.1–166.

Bay, B.K. et al., 1997. Statically equivalent load and support conditions produce different hip joint contact pressures and periacetabular strains. *Journal of Biomechanics*, 30(2), pp.193–196.

Beck, M. et al., 2005. Hip morphology influences the pattern of damage to the acetabular cartilage: femoroacetabular impingement as a cause of early osteoarthritis of the hip. *The Journal of Bone and Joint Surgery. British Volume*, 87(7), pp.1012–1018.

Bergmann, G. et al., 2001. Hip contact forces and gait patterns from routine activities. *Journal of Biomechanics*, 34(7), pp.859–871.

Bergmann, G., Graichen, F. & Rohlmann, A., 1993. Hip joint loading during walking and running, measured in two patients. *Journal of Biomechanics*, 26(8), pp.969–990.

Bombelli, R., 1976. *Osteoarthritis of the hip: pathogenesis and consequent therapy*, Springer-Verlag.

Brinker, M. & Miller, M., 1999. *Fundamentals of Orthopaedics, 1e*, Saunders.

Brown, T.D., Kikuike, A. & Ferguson, A.B.J., 1978. Towards a direct measurement of the dynamic contact force distribution in the hip. *The South African Mechanical Engineer*, 28, pp.210–214.

Brown, T.D. & Shaw, D.T., 1983. In vitro contact stress distributions in the natural human hip. *Journal of Biomechanics*, 16(6), pp.373–384.

Bullough, P., Goodfellow, J. & O'Conner, J., 1973. The relationship between degenerative changes and load-bearing in the human hip. *The Journal of Bone and Joint Surgery. British Volume*, 55(4), pp.746–758.

Chegini, S., Beck, M. & Ferguson, S., 2009. The effects of impingement and dysplasia on stress distributions in the hip joint during sitting and walking: a finite element analysis. *Journal of Orthopaedic Research: Official Publication of the Orthopaedic Research Society*, 27(2), pp.195–201.

Cowin, S.C., 1990. Deviatoric and hydrostatic mode interaction in hard and soft tissue. *Journal of biomechanics*, 23(1), pp.11–14.

David, N.A., Wild, P.M. & Djilali, N., 2012. Parametric study of a polymer-coated fibre-optic humidity sensor. *Measurement Science and Technology*, 23(3), p.035103.

Day, W.H., Swanson, S.A. & Freeman, M.A., 1975. Contact pressures in the loaded human cadaver hip. *The Journal of Bone and Joint Surgery. British Volume*, 57(3), pp.302–313.

Dennison, C. et al., 2008a. Ex vivo measurement of lumbar intervertebral disc pressure using fibre-Bragg gratings. *JOURNAL OF BIOMECHANICS*, 41(1), pp.221–225.

Dennison, C. et al., 2008b. Validation of a novel minimally invasive intervertebral disc pressure sensor utilizing in-fiber Bragg gratings in a porcine model - An ex vivo study. *SPINE*, 33(17), pp.E589–E594.

Dennison, C.R. et al., 2008c. A minimally invasive in-fibre Bragg grating sensor for intervertebral disc pressure measurements. *Measurement Science and Technology*, 085201, p.12.

Dennison, C.R. et al., 2010. An in-fiber Bragg grating sensor for contact force and stress measurements in articular joints. *Measurement Science and Technology*, 21, p.115803.

Dennison, C.R., 2011. Development of in-fibre Bragg grating contact force sensors for application to the human hip.

Dennison, C.R. & Wild, P.M., 2008a. Enhanced sensitivity of an in-fibre Bragg grating pressure sensor achieved through fibre diameter reduction. *Measurement Science and Technology*, 19(125301), p.11pp.

Dennison, C.R. & Wild, P.M., 2008b. Enhanced sensitivity of an in-fibre Bragg grating pressure sensor achieved through fibre diameter reduction. *Measurement Science and Technology*, 19(125301), p.11pp.

Dennison, C.R. & Wild, P.M., 2012. Superstructured fiber-optic contact force sensor with minimal cosensitivity to temperature and axial strain. *Applied Optics*, 51(9), pp.1188–1197.

Eckstein, F. et al., 1997. Quantitative analysis of incongruity, contact areas and cartilage thickness in the human hip joint. *Acta Anatomica*, 158(3), pp.192–204.

von Eisenhart, R. et al., 1999. Quantitative determination of joint incongruity and pressure distribution during simulated gait and cartilage thickness in the human hip joint. *JOURNAL OF ORTHOPAEDIC RESEARCH*, 17(4), pp.532–539.

von Eisenhart-Rothe, R. et al., 1997. Direct comparison of contact areas, contact stress and subchondral mineralization in human hip joint specimens. *ANATOMY AND EMBRYOLOGY*, 195(3), pp.279–288.

Erne, O.K. et al., 2005. Depth-dependent strain of patellofemoral articular cartilage in unconfined compression. *Journal of Biomechanics*, 38(4), pp.667–672.

Ferguson, S. et al., 2003. An in vitro investigation of the acetabular labral seal in hip joint mechanics. *Journal of Biomechanics*, 36, pp.171–178.

Ferguson, S. et al., 2000a. The acetabular labrum seal: a poroelastic finite element model. *Clinical Biomechanics*, 15(6), pp.463–468.

Ferguson, S. et al., 2000b. The influence of the acetabular labrum on hip joint cartilage consolidation: a poroelastic finite element model. *Journal of Biomechanics*, 33(8), pp.953–960.

Forster, H. & Fisher, J., 1999. The influence of continuous sliding and subsequent surface wear on the friction of articular cartilage. *Proceedings of the Institution of Mechanical Engineers, Part H: Journal of Engineering in Medicine*, 213(4), pp.329–345.

Ganz, R. et al., 2003. Femoroacetabular impingement: a cause for osteoarthritis of the hip. *Clinical Orthopaedics and Related Research*, (417), pp.112–120.

Ganz, R. et al., 2008. The etiology of osteoarthritis of the hip - An integrated mechanical concept. *CLINICAL ORTHOPAEDICS AND RELATED RESEARCH*, 466(2), pp.264–272.

Greaves, L.L. et al., 2009. Deformation and recovery of cartilage in the intact hip under physiological loads using 7T MRI. *Journal of Biomechanics*, 42(3), pp.349–354.

Greaves, L.L. et al., 2010. Effect of acetabular labral tears, repair and resection on hip cartilage strain: A 7 T MR study. *Journal of Biomechanics*, 43(5), pp.858–863.

Harris, W.H., 1986. Etiology of Osteoarthritis of the Hip. *Clinical Orthopedics and Related Research*, (213), pp.20–33.

HCUPnet, 2012. HCUPnet: A tool for identifying, tracking, and analyzing national hospital statistics. *National and Regional Estimates on Hospital Use for all Patients from the HCUP Nationwide Inpatient Sample (NIS)*. Available at: http://hcupnet.ahrq.gov/HCUPnet.jsp [Accessed July 14, 2012].

Hlavacek, M., 2002. The influence of the acetabular labrum seal, intact articular superficial zone and synovial fluid thixotropy on squeeze-film lubrication of a spherical synovial joint. *JOURNAL OF BIOMECHANICS*, 35(10), pp.1325–1335.

Ito, K. et al., 2001. Femoroacetabular impingement and the cam-effect. A MRI-based quantitative anatomical study of the femoral head-neck offset. *The Journal of Bone and Joint Surgery. British Volume*, 83(2), pp.171–176.

Kassarjian, A., Brisson, M. & Palmer, W.E., 2007. Femoroacetabular impingement. *European Journal of Radiology*, 63(1), pp.29–35.

Keogh, M.J. & Batt, M.E., 2008. A review of femoroacetabular impingement in athletes. *Sports Medicine (Auckland, N.Z.)*, 38(10), pp.863–878.

Konrath, G.A. et al., 1998. The role of the acetabular labrum and the transverse acetabular ligament in load transmission in the hip. *The Journal of Bone and Joint Surgery. American Volume*, 80(12), pp.1781–1788.

Kronenberg, P. et al., 2002. Relative humidity sensor with optical fiber Bragg gratings. *Optics Letters*, 27(16), pp.1385–1387.

Laude, F., Boyer, T. & Nogier, A., 2007. Anterior femoroacetabular impingement. *Joint, Bone, Spine: Revue Du Rhumatisme*, 74(2), pp.127–132.

Leunig, M., Beaulé, P.E. & Ganz, R., 2009. The Concept of Femoroacetabular Impingement: Current Status and Future Perspectives. *Clinical Orthopaedics and Related Research*, 467(3), pp.616–22.

Levine, R.G. et al., 2002. Biomechanical consequences of secondary congruence after both-column acetabular fracture. *Journal of Orthopaedic Trauma*, 16(2), pp.87–91.

Lizhang, J. et al., 2011. The effect of contact stress on cartilage friction, deformation and wear. *Proceedings of the Institution of Mechanical Engineers, Part H: Journal of Engineering in Medicine*, 225(5), pp.461–475.

Macfarlane, R.J. & Haddad, F.S., 2010. The diagnosis and management of femoro-acetabular impingement. *Annals of the Royal College of Surgeons of England*, 92(5), pp.363–367.

Macirowski, T., Tepic, S. & Mann, R., 1994. Cartilage Stresses In The Human Hip-Joint. *Journal Of Biomechanical Engineering-Transactions Of The Asme*, 116(1), pp.10–18.

Martini, F., 1998. *Fundamentals of anatomy and physiology* 4th ed., Upper Saddle River N.J.: Prentice Hall.

McLeish, R.D. & Charnley, J., 1970. Abduction forces in the one-legged stance. *Journal of Biomechanics*, 3(2), pp.191–209.

McNally, D.S., Adams, M.A. & Goodship, A.E., 1992. Development and validation of a new transducer for intradiscal pressure measurement. *Journal of Biomedical Engineering*, 14(6), pp.495–498.

Measures, R.M., 2001. *Structural Health Monitoring with Fiber Optic Technology*, Academic Press.

Michaeli, D.A., Murphy, S.B. & Hipp, J.A., 1997. Comparison of predicted and measured contact pressures in normal and dysplastic hips. *Medical Engineering & Physics*, 19(2), pp.180–186.

Mizrahi, J. et al., 1981. An experimental method for investigating load distribution in the cadaveric human hip. *The Journal of Bone and Joint Surgery. British Volume*, 63B(4), pp.610–613.

Mow, V.C. et al., 1980. Biphasic Creep and Stress Relaxation of Articular Cartilage in Compression: Theory and Experiments. *Journal of Biomechanical Engineering*, 102(1), p.73.

Murray, R.O., 1965. The aetiology of primary osteoarthritis of the hip. *The British Journal of Radiology*, 38(455), pp.810–824.

Ngoi, B.K.A. et al., 2004. Enhanced lateral pressure tuning of fiber Bragg gratings by polymer packaging. *Optics Communications*, 242(4–6), pp.425–430.

Park, S. et al., 2003. Cartilage interstitial fluid load support in unconfined compression. *Journal of Biomechanics*, 36(12), pp.1785–1796.

Paul, J.P., 1976. Force Actions Transmitted by Joints in the Human Body. *Proceedings of the Royal Society of London. Series B, Biological Sciences*, 192(1107), pp.163–172.

Pauwels, F., 1935. Der schenkelhalsbruch ein mechanisches problem. *Z Orthop Ihre Grenzgeb*, 63, p.138.

Pearle, A., Warren, R. & Rodeo, S., 2005. Basic science of articular cartilage and osteoarthritis. *CLINICS IN SPORTS MEDICINE*, 24(1), p.1–+.

Rushfeldt, P.D., Mann, R.W. & Harris, W.H., 1981. Improved techniques for measuring in vitro the geometry and pressure distribution in the human acetabulum. II Instrumented endoprosthesis measurement of articular surface pressure distribution. *Journal of Biomechanics*, 14(5), pp.315–323.

SourceForge, 2011. JointTrack. *SourceForge*. Available at: http://sourceforge.net/projects/jointtrack/ [Accessed July 26, 2012].

Steindler, A., 1955. *Kinesiology of the human body under normal and pathological conditions*, Thomas.

Tarasevicius, S. et al., 2007. Intracapsular pressure and elasticity of the hip joint capsule in osteoarthritis. *JOURNAL OF ARTHROPLASTY*, 22(4), pp.596–600.

Terayama, K., Takei, T. & Nakada, K., 1980. Joint space of the human knee and hip joint under a static load. *Engineering in Medicine*, 9(2), pp.67–74.

Widmer, K.H., Zurfluh, B. & Morscher, E.W., 1997. Contact surface and pressure load at implant-bone interface in press-fit cups compared to natural hip joints. *Der Orthopäde*, 26(2), pp.181–189.

Wingstrand, H., Wingstrand, A. & Krantz, P., 1990. Intracapsular and atmospheric pressure in the dynamics and stability of the hip. A biomechanical study. *Acta Orthopaedica Scandinavica*, 61(3), pp.231–235.

Witte, H., Eckstein, F. & Recknagel, S., 1997. A calculation of the forces acting on the human acetabulum during walking. Based On in vivo force measurements, kinematic analysis and morphometry. *Acta Anatomica*, 160(4), pp.269–280.

Wu, J.Z., Herzog, W. & Epstein, M., 1998. Effects of inserting a pressensor film into articular joints on the actual contact mechanics. *Journal of Biomechanical Engineering*, 120(5), pp.655–659.

# Appendix A: Detailed Specimen Potting Protocol

The detailed procedure used to pot the specimen in PMMA as explained in Section 3.4 is as follows:

1. Drill two 1/4" diameter transverse holes in distal end of the remaining femoral shaft for attachment to the femoral mounting fixture on the material testing machine. The holes must pass through centre of the linear aspera on the posterior femoral shaft to ensure neutral internal rotation.
2. Trim the distal tip of femoral shaft as necessary to integrate with mounting fixture.
3. Add wood screws to the iliac crest to improve fixation in potting material.
4. Attach the adjustable potting fixture (Figure 3-7-a) to the laboratory stand and then to the inverted specimen (Figure 3-7-b) using wood screws.
5. Use a laser level to project a vertical plane from the sagittal direction. This represents the anatomical coronal plane.
6. Align the ASIS and PT vertically in the projected plane.
7. Set the correct medial-lateral tilt of the hemipelvis in the coronal plane by visually comparing with a full pelvis Sawbones® model positioned with the left and right ASIS horizontal.
8. Insert a long wood screw into the ilium, adjusting depth until the screw head is in the same vertical projected plane as the ASIS and PT. The screw head provides the third point necessary to constrain the pelvis in this plane.
9. Project a second vertical plane from the anterior direction with a second laser level capable of angular adjustments. This new plane should be parallel to the sagittal plane and orthogonal to the plane projected in step 5.
10. Create two marks on the ilium falling on the vertical line projected onto the anterior face of the ilium projected by the laser in step 9.
11. Rotate the laser plane from step 9 by adjusting the level 13º from vertical in the direction allowing the PT to rotate medially about the joint centre.

12. Adjust the medial-lateral tilt of the pelvis until the marks from step 10 line up with the angled line projected in step 11.
13. Re-check that the ASIS, PT, and screw head from step 8 remain in the vertical plane projected in step 5.
14. Place the potting container underneath the iliac crest and lower the specimen on the laboratory stand to the correct depth for potting.
15. Add PMMA potting material using laboratory stand to support the specimen until cured.
16. Remove specimen potting fixture from step 4 and wood screw from step 8 from the ilium.

# Appendix B: Detailed Test Protocol

The following steps comprise the detailed test protocol explained in Section 3.10:

Initial preparation during Day 1:

1. Instrument specimen with FBG sensors as per Section 3.5 and 3.6.
2. Place specimen in empty fluid bath container
3. Transport to lab with material testing machine
4. Mix PBS+ and protease inhibitor solution
5. Add solution to container with specimen
6. Proceed with testing for Day 1 (Steps 7-13)

Daily testing protocol:

7. Attach specimen to material testing machine while submersed in fluid bath as per Section 3.7
8. Warm fluid bath to room temperature using heater and circulation pump
9. Remove heater and pump
10. Wait 1-2 hours until steady state response from all FBG sensors is reached indicating thermal equilibrium of the specimen and bath
11. Test specimen on material testing using load profile in Section 3.8
12. Remove specimen, still in bath, from material testing machine
13. Store specimen in fluid bath, surrounded by ice in large sink, overnight

Day 4, Labral Resection:

14. Remove specimen from fluid bath
15. Resect anterior half of labrum as per Section 3.11
16. Replace specimen in fluid bath
17. Proceed with testing for Day 4 (Steps 7-13)
18. Remove specimen from fluid bath and disarticulate to inspect sensor location and articular cartilage condition
19. Dispose of fluid and package specimens for longterm storage.

# Appendix C: Protease Solution

As done in other *in vitro* or *ex vivo* experiments[1,2], the following protease inhibitors were added to phosphate buffered saline solution (pH 7.4) to reduce the rate of cartilage decomposition.

| Description | Sigma-Aldrich® Part Number | Desired Molarity [M] | Molecular Weight [g/M] | Amount per L Solution [g/L] |
|---|---|---|---|---|
| Benzamidine hydrochloride hydrate (B-HCL) | B6506 | 0.005 | 156.6 | 0.78 |
| Ethylenediaminetetraacetic acid disodium salt dihydrate (ETDA) | E5134 | 0.002 | 372.2 | 0.74 |
| N-Ethylmaleimide (NEM) | E3876 | 0.01 | 125.1 | 1.25 |
| Phenylmethanesulfonyl fluoride (PMSF) | 78830 | 0.001 | 174.2 | 0.17 |

[1] Frank, E.H. et al., 1987. Streaming potentials: a sensitive index of enzymatic degradation in articular cartilage. *Journal of Orthopaedic Research: Official Publication of the Orthopaedic Research Society*, 5(4), pp.497–508.

[2] Greaves, L.L., 2008. *Effect of acetabular labral tears, repair and resection on hip cartilage strains : a 7T MR study*. University of British Columbia.